Fall 2014

Design and analysis of solar cells by coupled electrical - optical simulation

Xufeng Wang
Purdue University

Recommended Citation

Wang, Xufeng, "Design and analysis of solar cells by coupled electrical - optical simulation" (2014). *Open Access Dissertations*. 386.
https://docs.lib.purdue.edu/open_access_dissertations/386

Graduate School Form 30
(Updated 11/20/2014)

PURDUE UNIVERSITY
GRADUATE SCHOOL
Thesis/Dissertation Acceptance

This is to certify that the thesis/dissertation prepared

By Xufeng Wang

Entitled
Design and Analysis of Solar Cells by Coupled Electrical-Optical Simulation

For the degree of Doctor of Philosophy

Is approved by the final examining committee:

Mark Lundstrom	Peter Bermel
Muhammad Ashraful Alam	Jeffery Gray
Gerhard Klimeck	

To the best of my knowledge and as understood by the student in the Thesis/Dissertation Agreement, Publication Delay, and Certification/Disclaimer (Graduate School Form 32), this thesis/dissertation adheres to the provisions of Purdue University's "Policy on Integrity in Research" and the use of copyrighted material.

Approved by Major Professor(s): Mark Lundstrom
Peter Bermel

Approved by: Michael R. Melloch 12/08/2014
Head of the Department Graduate Program Date

DESIGN AND ANALYSIS OF SOLAR CELLS BY COUPLED ELECTRICAL – OPTICAL SIMULATION

A Dissertation

Submitted to the Faculty

of

Purdue University

by

Xufeng Wang

In Partial Fulfillment of the

Requirements for the Degree

of

Doctor of Philosophy

December 2014

Purdue University

West Lafayette, Indiana

To Hui…

TABLE OF CONTENTS

Page

LIST OF TABLES vii

LIST OF FIGURES viii

ABSTRACT xiii

1 INTRODUCTION 1
  1.1 The Solar Cell Device 1
  1.2 The Shockley-Queisser Limit 3
    1.2.1 Toward high J_{SC} 6
    1.2.2 Toward high V_{OC} 11
  1.3 Thesis Overview 12

2 DESIGN OF GAAS SOLAR CELLS TOWARD THE SHOCKLEY-QUESSIER LIMIT 14
  2.1 Preface 14
  2.2 Introduction 14
  2.3 Approach 16
    2.3.1 Efficiency Limit in GaAs Solar Cells 16
    2.3.2 Radiative Lifetime Enhancement by Photon Recycling 16
    2.3.3 Self-consistent Photon Recycling with the Semiconductor Equations 18
  2.4 Device Structure 20
  2.5 Results 23
    2.5.1 Fundamental Limits 23
    2.5.2 Effects of Backside Mirror 25
    2.5.3 Effects of SRH Recombination 28

Page
2.5.4 Effects of Series Resistance 29
2.5.5 Effects of Base Thickness 29
2.5.6 Summary of Loss Mechanisms 30
2.6 Discussion 31
2.7 Summary 32
3 DESIGN OF NANOWIRE SOLAR CELLS TOWARD THE SHOCKLEY-QUEISSER LIMIT 34
3.1 Preface 34
3.2 Introduction 34
3.3 Numerical methods 37
3.3.1 Optics module 37
3.3.2 Electrical module 39
3.3.3 Electro-optically coupled simulator 39
3.4 Results and discussion 40
3.4.1 Baseline parameters and performance 40
3.4.2 Nanowire solar cell with radial junction 45
3.4.3 Nanowire solar cell with vertical junction 47
3.4.4 Planar thin-film solar cell 50
3.4.5 Summary 52
3.5 Summary 54
4 DESIGN OF GAINP/GAAS TANDEM SOLAR CELLS TOWARD THE SHOCKLEY-QUEISSER LIMIT 55
4.1 Preface 55
4.2 Introduction 55
4.3 Approach 57
4.4 Calibration with Experiments 58
4.4.1 Single-junction GaAs Cell 58
4.4.2 GaAs/GaAs Tunnel Junction 60
4.5 Results and discussion 62

Page
4.5.1 Baseline GaInP/GaAs Tandem Solar Cell 62
4.5.2 Effects of Mirror Reflectivity 66
4.5.3 Effects of GaInP Top Cell Back-surface Field 67
4.6 Summary 71
5 CHARACTERIZATION OF SOLAR CELLS WITH THE RECIPROCITY THEOREM 73
5.1 Preface 73
5.2 Introduction 73
5.3 Approach 75
5.3.1 Self-consistent Optical Module with the Semiconductor Equations 75
5.3.2 Model Structures 75
5.4 Results 78
5.4.1 GaAs Solar Cell 78
5.4.2 CIGS Solar Cell with Trap-induced Nonsuperposition 80
5.4.3 CdTe Solar Cell with Schottky Barrier-induced Nonsuperposition 83
5.5 Discussion 85
5.6 Summary 86
6 CHARACTERIZATION OF INP THIN FILMS WITH TRPL/PLE/SIMULATION COUPLED APPROACH 87
6.1 Preface 87
6.2 Introduction 87
6.3 Method 88
6.3.1 Experimental Setup 88
6.3.2 Simulation Setup 92
6.4 TRPL & PLE Sensitivity 92
6.5 Results and Analysis 95
6.5.1 VLS-grown InP Thin Film 95
6.5.2 InP Substrate 97
6.6 Summary 98

Page

7 CONCLUSIONS AND FUTURE WORK 99
  7.1 Conclusions 99
  7.2 Future work 100
    7.2.1 Nanowire array 100
    7.2.2 Tandem solar cell 101

VITA 115

LIST OF TABLES

Table Page

3.1. Key baseline material parameters 42

3.2. Performance comparison for various III-V single-junction solar cell types under 1-Sun, where shaded rows are numerical predictions in this study. 53

4.1. Summary of cell performance for various structures investigated by this study. The shaded rows are benchmarked to have similar structure to the experiments. 71

5.1. Important device parameters for (a) the baseline solar cells, (b) the baseline CIGS solar cell, and (c) the baseline CdTe solar cell. Parameters: donor-like (acceptor-like) defect density N_{DG} (N_{AG}); donor-like (acceptor-like) defect peak energy E_D (E_A); trap Gaussian distribution width W_G; and capture cross-section σ. 78

LIST OF FIGURES

Figure Page

1.1. Band diagram and structure of a typical GaAs solar cell, modeled after [7]. The collection of a photon-generated electron-hole pair is also illustrated. Electrons travel “down” the conduction band to the left, while holes travel “up” the valence band to the right..2

1.2. Fundamental loss components for a single-junction solar cell versus semiconductor band gap, with zoomed-in region showing current record efficiencies for single-junction solar cells, compared to their Shockley-Queisser limits. 5

1.3. Record efficiency chart for some selected single-junction solar cells from NREL solar cell efficiency chart. 5

1.4. Absorbed fraction of photons above the crystalline silicon bandgap versus the silicon layer thickness. The layer is planar and has no backside mirror. 7

1.5. Some light trapping approaches previously explored in the literature: (a) random pyramidal texture used for c-Si solar cells [32], (b) advanced meta-surface trapping light with generalized Snell’s law [33], and (c) Bragg reflector for high reflectivity [31]. 9

2.1. Comparison among different intrinsic GaAs absorption coefficients as a function of wavelength close to the GaAs bandedge (left graph) and the corresponding effective recombination coefficients (table on right). 18

2.2. Overall scheme for ADEPT 2.0 upgraded with the addition of a photon recycling module. 19

2.3. Idealized single junction GaAs thin film solar cell with reflective back contact......20

2.4. Left: Baseline light IV characteristics with (blue solid line) vs. without (red dashed line) photon recycling. Right table: The key metrics (Voc, Jsc, and FF) obtained for the baseline cell with photon recycling effects (blue solid line on the left) matches those reported in ref. [7] closely..21

Figure Page

2.5. Radiative, SRH, and Auger recombination within baseline cell at V_{OC}. (a) Recombination rate vs. position. (b) Integrated recombination rate at V_{OC} for radiative recombination (Radiative), bulk SRH recombination (SRH), Auger recombination (Auger), and surface SRH recombination (Surface). "Position" on x-axis corresponds to the depth relative to sun-facing cell surface. Backside mirror is located at the right end of the x-axis. (See Fig. 2.3) 22

2.6. Left: Comparison of IV at Shockley-Queisser limit by analytical detailed balance method (solid line) and ADEPT 2.0 (black filled circles). Right: Characteristic parameters for Shockley-Queisser limit are compared to a planar cell in the table.. 24

2.7. Top: Ratio of the loss of photons through the back surface to the loss through the front surface as a function of back mirror reflectivity. Bottom: For 85% and 95% mirror reflectivity, shown here is the percentage of emitted photon escaping from front and losing at backside mirror at different location within the device under open circuit condition. "Position" on x-axis corresponds to the depth relative to sun-facing cell surface. Backside mirror is located at the right end of the x-axis. (See Fig. 2.3) 27

2.8. V_{OC}, J_{SC}, and efficiency as a function of backside mirror reflectivity. The marked 0.85 reflectivity is used in baseline case. 28

2.9. V_{OC}, J_{SC}, and efficiency as a function of SRH lifetimes. Notice the log scale used on x-axis. 28

2.10. Fill factor and efficiency as a function of different series resistance values. The cell has an area of 1 cm^2 29

2.11. V_{OC}, J_{SC}, and efficiency as a function of base thickness for three different SRH lifetimes. 30

2.12. List of loss mechanisms considered in this study and their impact on baseline cell efficiency. 31

3.1. Electro-optically coupled simulation framework flowchart, suitable for incorporating photon recycling effects into a PV device simulation in a self-consistent fashion... 40

3.2. (a) Baseline single nanowire solar cell geometry with a radial junction; (b) Absorptivity vs. incident wavelength for the baseline single nanowire solar cell. ... 41

3.3. Three important quantities are spatially resolved with wave optics simulation: (a) Carrier generation rate under AM1.5G. (b) Spontaneous emission enhancement with respect to a homogeneous environment. (c) Spatially resolved photon recycling probability. 42

3.4. With radial junction, (a) Electron current flow streamline at J_{SC}. (b) Hole current flow streamline at J_{SC}. (c) Benchmark single nanowire solar cell light and dark IV.44

3.5. With no minority carrier deflections at both contacts, performances for various surface recombination velocities are displayed. (a) J_{SC} and V_{OC}. (b) Percentage of each major loss mechanism at V_{OC}. 46

Figure Page

3.6. With complete minority carrier deflection at both contacts, performances for various surface recombination velocities are displayed. (a) J_{SC} and V_{OC}. (b) Percentage of each major loss mechanism at V_{OC}. 47

3.7. With vertical junction, (a) Device geometry. (b) Electron current flow streamline at J_{SC}. (c) Hole current flow streamline at J_{SC}. 48

3.8. With no minority carrier deflections at both contacts, performances for various surface recombination velocities are displayed. (a) J_{SC} and V_{OC}. (b) Percentage of each major loss mechanism at V_{OC}. 49

3.9. With complete minority carrier deflections at both contacts, performances for various surface recombination velocities are displayed. (a) J_{SC} and V_{OC}. (b) Percentage of each major loss mechanism at V_{OC}. 49

3.10. (a) Thin-film solar cell geometry. (b) Illustration of photon recycling and emission inside a thin-film solar cell. 51

3.11. With bulk SRH lifetime at 1 us, performances for various backside mirror reflectivities are displayed. (a) J_{SC} and V_{OC}. (b) Percentage of each major loss mechanism at V_{OC}. 52

4.1. Benchmark single-junction GaAs solar cell with variable back-contact thickness: (a) device structure, and (b) band diagram under equilibrium. 59

4.2. (a) V_{OC} and (b) J_{SC} from simulation for various contact thicknesses comparing to experimentally reported value. A combined optical loss at 6% due to shadowing and reflection is assumed. Both series show a match to within 2% for all data points. 60

Fig. 4.3. GaAs/GaAs tunnel junction used in this study: (a) band diagram under equilibrium, and (b) numerically simulated tunneling current benchmark with experiment. Resistance under AM1.5G spectrum is predicted to be small, as is also seen experimentally. 61

4.4. GaInP/GaAs tandem solar cell modeled after the NREL 31.1% cell: (a) device structure, and (b) band diagram under equilibrium. 62

4.5. (a) Simulated IV (green line) compared with measured NREL 31.1% cell (black asterisk), and (b) Simulated EQE from top GaInP cell (blue line) and bottom GaAs cell (red line). The two combined (green line) is compared with the measured EQE (black dots) from the NREL 31.1% cell and shows a close match. 64

4.6. (a) Recombination versus position at V_{OC}, and (b) the generation current (J_{gen}), the terminal current under light (J_{light}), the recombination current (J_{rec}) versus applied voltage. The leakage current through the BSF of top GaInP cell (J_{BSF}) is negligible in this case. 65

Figure Page

4.7. (a) The effect of mirror reflectivity on V_{OC} with GaInP IRE = 19% (green line), IRE = 85% (blue line), and without (red line) non-radiative recombination (R_{nr}). The V_{OC} values for the NREL 31.1% cell (black dash line) and the NREL 29.5% cell (blue dash line) are provided as reference. (b) Luminescence coupling inside the cell among the top GaInP cell, the bottom GaAs cell, and the mirror. 67

4.8. GaInP/GaAs tandem solar cell modeled after the NREL 29.5% cell [117]: (a) device structure, and (b) band diagram under equilibrium. 68

4.9. (a) Simulated IV (green line) compared with measured NREL 31.1% cell (black asterisk) and NREL 29.5% cell (black dots), and (b) Simulated EQE from top GaInP cell (blue line) and bottom GaAs cell (red line). The two combined (green line) is compared with the measured EQE (black dots) from the NREL 29.5% cell. 69

4.10. (a) The generation current (J_{gen}), the terminal current under light (J_{light}), the recombination current (J_{rec}), and the leakage current through the BSF of top GaInP cell (J_{BSF}) versus applied voltage. (b) The effect of mirror reflectivity on V_{OC} with GaInP IRE = 19% or IRE = 85% (green line, since both lines are very close), and without (red line) non-radiative recombination (R_{nr}). The V_{OC} values for the NREL 31.1% cell (black dash line) and the NREL 29.5% cell (blue dash line) are provided as reference. 70

4.11. Percentage of each loss mechanism at V_{OC}: (a) with a less efficient GaInP BSF, (b) with AlGaInP BSF and GaInP IRE = 19%, and (c) with AlGaInP BSF and GaInP IRE = 85%. 71

5.1. (a) Baseline single junction GaAs thin film solar cell with reflective back contact. (b) Baseline CIGS solar cell modeled after Gloeckler [131]. (c) Baseline CdTe solar cell modeled after Demtsu [95]. 76

5.2. (a) Equilibrium band diagram for the baseline GaAs solar cell. (b) Illuminated (AM1.5G) and dark IV displaying superposition behavior. The asterisk symbol marks the maximum power point (MPP). 79

5.3. (a) ERE values derived from the RRR and direct calculation for different mirror reflectivities (0% - 100%). (b) ERE values derived from the RRR and direct calculation for different base minority carrier lifetime (10 ps – 100 μs). 79

5.4. (a) Equilibrium band diagram for the baseline CIGS solar cell. (b) Illuminated (AM1.5G) and dark IV displaying nonsuperposition behavior. The asterisk symbol marks the maximum power point (MPP). 80

5.5. (a) ERE values derived from the RRR and direct calculation for different ΔE_C (0.1 eV – 0.5 eV, with 0.05 eV increments). (b) Ratio between ERE values from direct computation and the RRR vs. J-V cross-over voltages in Fig. 5.5(a). 81

Figure Page

5.6. (a) ERE values derived from the RRR and direct calculation for different mirror reflectivities (0% - 100%, with 20% increments). (b) ERE values derived from the RRR and direct calculation for different trap density (8.5×10^{17}, 9×10^{17}, 1×10^{18}, 1.5×10^{18}, 2×10^{18}, 2.5×10^{18}, and 3×10^{18} /cm^3) in CdS layer. Conduction band offset is set at 0.3 eV and is unaffected by the trap density. 82

5.7. (a) Equilibrium band diagram for the baseline CdTe solar cell. (b) Illuminated (AM1.5G) and dark IV displaying nonsuperposition behavior. The asterisk symbol marks the maximum power point (MPP). 83

5.8. (a) ERE values derived from the RRR and direct calculation for different Schottky barrier height (0 eV – 0.5 eV, with 0.05 eV increments). (b) ERE values derived from the RRR and direct calculation for different base minority carrier lifetime (10 ps – 100 μs) with a Schottky barrier height of 0.4 eV 84

6.1. Picture of the PLE setup used in this study. Several electrical components including the LED driver unit, lock-in amplifier, and controlling PC are not captured in this picture. 90

6.2. (a) Layout for the PLE experimental setup used in this study. The measurement event starts at the tunable LED matrix at the lower right corner. The sample under testing is at the upper left corner, and the PLE emission signal is detected at the lower left corner. (b) PLE for an unpassivated GaAs wafer. (c) The TCSPC TRPL experimental setup used in this study. 91

6.3. Numerical simulations demonstrate that: (a) TRPL and (b) PLE show greatly differing responses to variations in surface recombination velocity over the range $S_{\mathrm{front}} = 1, 10, 10^2, 10^3, 10^4, 10^5, 10^6$, and 10^7 cm/s at $\tau_{\mathrm{SRH}} = 28$ ns. PLE-based estimates of S_{front} generally have much smaller errors. 93

6.4. Internal loss components predicted for (a) TRPL vs. time and (b) PLE vs. wavelength at $S_{\mathrm{front}} = 5\mathrm{x}10^4$ cm/s and $\tau_{\mathrm{SRH}} = 12$ ns. These specific parameters are chosen since they provide the best overall fit to the InP sample tested, as shown in Fig. 6.7. 94

6.5. (a) TRPL and (b) PLE for $\tau_{\mathrm{SRH}} = 5, 9, 13, 17, 21$, and 25 ns at $S_{\mathrm{front}} = 10^4$ cm/s. 95

6.6. VLS-grown InP thin film: least-square error map as a function of SRH lifetime and front surface recombination velocity when fitting to simulations of (a) TRPL and (b) PLE. The least-square error units are arbitrary, with cold blue regions indicating smaller error and best fit, with hot red regions being the opposite. 96

6.7. Best overall fit for (a) TRPL and (b) PLE. Simulations are solid blue curves, and measurements are green dots 97

6.8. InP wafer: Least-square error map as a function of SRH lifetime and front surface recombination velocity when fitting to simulations of (a) TRPL and (b) PLE. The least-square error units are arbitrary, with cold blue regions indicating smaller error and best fit, with hot red regions being the opposite. 98

ABSTRACT

Wang, Xufeng. Ph.D., Purdue University, December 2014. Design and Analysis of Solar Cells by Coupled Electrical-optical Simulation. Major Professors: Mark Lundstrom and Peter Bermel.

Careful electrical design and optical design are both crucial for achieving high-efficiency solar cells. It is common to link these two aspects serially; the optical design is first done to minimize reflection and maximize light trapping, and then the resulting optical generation rate is input to the electrical simulation. For very high efficiency solar cells that approach the Shockley-Queisser limit, however, electrical and optical transports are tightly coupled in both directions. Photons generated by radiative recombination can be reabsorbed to create additional electron-hole pairs (so-called photon recycling), which decreases losses. A variety of novel photon management schemes are currently being explored. To achieve the promise of these new approaches, a self-consistent simulation framework that rigorously treats both photons and electrons is needed[1]. In this work, the thin-film GaAs solar cell, the single nanowire solar cell, and the GaInP/GaAs tandem solar cell are investigated. For solar cell characterization, this work examines the validity of the reciprocity theorem and quantitative lifetime parameter extraction using Time-Resolved Photoluminescence (TRPL) and Photoluminescence Excitation Spectroscopy (PLE). Overall, this thesis work has created a new simulation tool for advanced photovoltaic devices based on the self-consistent coupling of wave optics with electronic transport, which lead to accurate predictions of the characteristics and performance. Optimization of photon recycling facilitates improved design strategies to approach the Shockley-Queisser limit, which will eventually pave the way for extension to advanced

---

[1] The development and application of such a model is described in this thesis.

designs, capable of approaching or even exceeding the Shockley-Queisser limit in the future.

1 INTRODUCTION

The sun is a powerful source of energy, delivering to Earth approximately 3,850,00 exajoules (EJ) per year, which is more than 10,000 times the daily energy used by us today [1, 2]. It sustains the ecosystem, which is vital to all life on the planet. Solar radiation is absorbed in different proportions by the land surface, oceans, and atmosphere. Temperature gradients thus appear, giving rise to natural phenomena such as wind and water cycle. Plants convert the solar energy into chemical energy through photosynthesis, while humans rely on the sun to see and to keep warm.

Since historic times, humans have found creative and effective ways of tapping into the vast amount of solar energy. Solar cells are able to directly convert sunlight into electricity. The worldwide solar power generated from photovoltaic (PV) devices is rapidly increasing. As of 2013, approximately 0.54% of total U.S. electricity was produced from PV, comparing to only 0.06% in 2008 [3-5]. Solar cells can be made from solid-state materials without moving parts, resulting in a long operational lifetime. In fact, most of the commercial solar panels today offer a warranty of over 25 years. Thus, solar will play an increasingly important role in the U.S. energy landscape.

1.1 The Solar Cell

The operating principles of the solar cell are the mechanisms of carrier generation and collection. This is very often implemented via a semiconductor-based p-n junction—one of the most fundamental structures in integrated circuits (IC) [6]. A simple GaAs thin-film solar cell structure and band diagram is shown in Fig. 1.1. The structure consists of an n-type emitter and a p-type base forming the junction for charge separation. At the emitter, a window layer having a high valence band offset is used to prevent minority carriers, which are electrons, from entering the n-contact. Similarly, a back-surface field (BSF) with a high conduction band offset is used at the p-contact. This structure nicely summarizes important design features of a solar cells: charge generation, separation, and collection, and minority carrier deflection at the contacts.

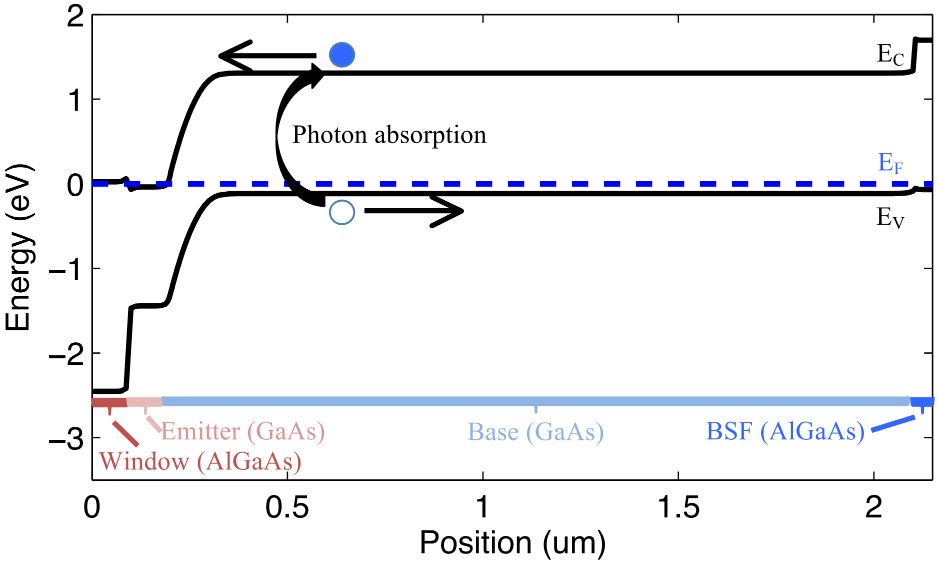

Fig. 1.1. Band diagram and structure of a typical GaAs solar cell, modeled after [7]. The collection of a photon-generated electron-hole pair is also illustrated. Electrons travel “down” the conduction band to the left, while holes travel “up” the valence band to the right.

Under illumination, the junction separates the photon-excited carriers, so the electron (hole) may flow into the n-contact (p-contact), resulting in a steady-state DC current. In order to harvest energy from this device, a positive voltage bias must be applied to the p-n junction. As more bias is applied, the current eventually will become zero, where, again, no energy can be harvested. Thus, the maximum power point (MPP) lies at an intermediate voltage. One of the main causes for this current to decrease is the injected dark current (J_{dark}) by the p-n junction cancelling the light-generated current (J_{gen}), and the resulting terminal current (J) is:

$$J(V) = J_{gen}(V) - J_{dark}(V)\,. \tag{1.1}$$

Notice the voltage-dependence of J_{gen}, as it can also cause the terminal current to decrease, because, as the applied bias increases over the p-n junction, the built-in electric field decreases. When it eventually disappears, the light-generated carriers have an equal chance to reach the p and n contacts, resulting in a net current of zero.

To evaluate the overall performance of the solar cell, several figures of merit are used, including 1) the current at zero bias, or the so-called short-circuit current (J_{SC}), 2) the voltage at zero current, or the so-called open-circuit voltage (V_{OC}), and 3) the MPP where the most power can be extracted. From these three quantities, two other important figures of merits can be calculated. The first is the fill-factor (FF), defined as [6]

$$FF = \frac{V_{mpp} J_{mpp}}{V_{OC} J_{SC}} \tag{1.2}$$

where V_{mpp} and J_{mpp} are the voltage and current at MPP respectively. Finally, the most important figure of merit is the power conversion efficiency (η) of the solar cell, which is defined as [6]

$$\eta = \frac{V_{mpp} J_{mpp}}{P_{in}} = \frac{J_{SC} V_{OC} FF}{P_{in}} \tag{1.3}$$

1.2 The Shockley-Queisser Limit

Since the first demonstration of a practical silicon-based photovoltaic device at Bell Labs in 1954 [8], solar cell efficiency has steadily improved over the years. This efficiency cannot of course increase without bound but is subject to a certain limit, depending primarily on the material. Shockley and Queisser pointed this out in their famous 1961 paper [9]. Their argument was based on a fundamental reciprocity between absorption and emission: the more absorptive a material is, the more emissive the material will be in thermal equilibrium due to Kirchoff's law of thermal radiation, derived from the Second Law of Thermodynamics. In their treatment, the solar cell is modeled as a blackbody. The solar cell's bandgap (E_G) acts as a filter and prevents any photon with energy below E_G from the sun being absorbed. On the other hand, the blackbody emission from the cell cannot emit any photon with energy below E_G either. Increased absorption increases the J_{SC} of the cell, while increased emission decreases the V_{OC}. This tradeoff places a fundamental limit on the ultimate efficiency of solar cells—the so-called Shockley-Queisser limit. It also reveals the important design principle of cells approaching the Shockley-Queisser limit, which is the core idea of this thesis:

promoting in-coupling of sunlight to increase the J_{SC}, while suppressing out-coupling of radiative recombination emission to increase the V_{OC}.

By strongly coupling sunlight with the solar cell, sunlight absorption, and thus the J_{SC}, can be increased. Unlike the assumption in the Shockley-Queisser limit however, not all photons from the sunlight with energy higher than the bandgap can be absorbed by the solar cell in reality. Photons can be lost, for example, due to front reflection or incomplete absorption. The later is especially true for silicon, which has poor absorption properties due to its indirect bandgap. It is also true for many of the thin film solar cells due to their small thicknesses below 50 μm [6]. Advanced optical designs have been proposed to help decreasing the reflection and increasing the optical path of photons traveling inside the cell [10, 11].

Radiative recombination, which is the dominant loss mechanism for cells near the Shockley-Queisser limit, can be effectively suppressed, leading to an increased V_{OC}. The mechanism is as follows. For each radiative recombination event, the photo-generated excess carriers radiatively recombine by giving up energy to create one photon per electron-hole pair. After the emission, these photons travel within the solar cell structure, and some of them will be re-absorbed, while the rest are lost by escaping the structure or being parasitically absorbed by backside mirror or other non-photovoltaic regions. If the emitted photons are re-absorbed in the so-called photon-recycling process, electron-hole pairs are created again, so these are losses recovered and can effectively reduce the radiative recombination. With clever cell designs, one can promote the photon recycling to obtain high, sometimes world-record, efficiencies.

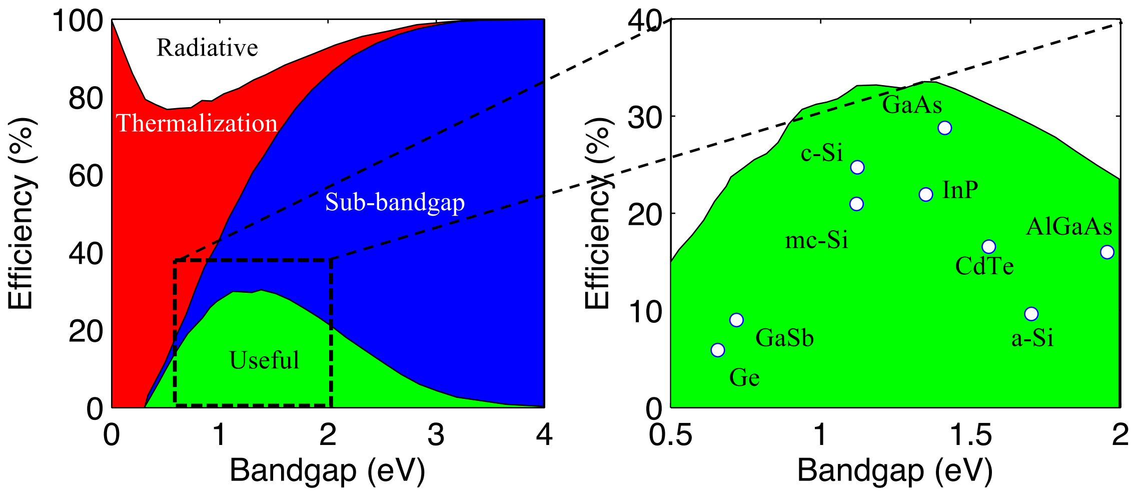

Fig. 1.2. Fundamental loss components for a single-junction solar cell versus semiconductor band gap, with zoomed-in region showing current record efficiencies for single-junction solar cells, compared to their Shockley-Queisser limits.

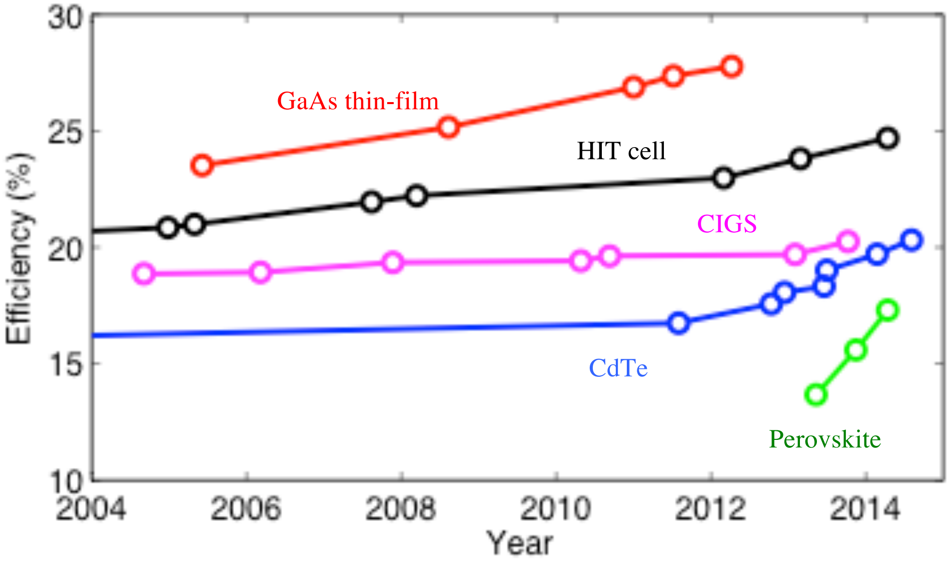

Fig. 1.3. Record efficiency chart for some selected single-junction solar cells from NREL solar cell efficiency chart.

Fig. 1.2 shows the various fundamental loss components for single-junction solar cell vs. bandgap. For solar cells with lower bandgaps, thermalization losses dominate. Thermalization loss occurs when a photon with energy significantly higher than the material bandgap is absorbed. When the energized electron-hole pair interacts with its surroundings, the excess energy is lost as heat. For solar cells with higher bandgaps, the sub-bandgap photon loss dominates. This is because the material is unable to absorb the photons with lower energy than its bandgap. Therefore, there is an optimal bandgap for solar cells close to 1.4 eV. Fig. 1.2 also includes a zoom-in reproduction from the original Shockley-Queisser paper showing the efficiency limits for a range of E_G. On the same figure for comparison are record single-junction efficiencies for several common semiconductor materials. GaAs solar cell at 28.8% is the closest to its Shockley-Queisser limit today [12], while c-Si at 25.0%, which is the most commonly used semiconductor material for commercial solar cells, is still significantly below its ultimate efficiency limit. A number of alternatives and extensions to the original Shockley-Queisser paper have been reported, including the multi-junction limit [13], limits considering re-emission [14], and limits under finite absorption [15]. In all cases, the fundamental reciprocity between absorption and emission is maintained. Unconventional physics-based approaches have been proposed to exceed the single-junction Shockley-Queisser limit, including the use of multi-exciton generation [16], hot carrier collection [17], and intermediate band gap states [18], although none of the above have experimentally demonstrated efficiencies higher than conventional designs. Fig. 1.3 shows the impressive efficiency improvement of some popular solar cell types in the past 10 years.

1.2.1 Toward high J_{SC}

The importance of a strong in-coupling of sunlight for solar cells cannot be overstated. A bare piece of silicon in contact with air has a reflectivity ~30% [19]. It is common to apply layers of anti-reflection coating (ARC) on top of solar cells to minimize reflective losses. For example, an application of SiN/TiO_2 ARC layers on silicon can decrease the spectrally averaged reflectivity to as little as ~5% [20]. Moreover, the absorption of sunlight requires sufficient material thickness. For silicon, which has an indirect bandgap, approximately 400 μm in thickness is needed to absorb 99% of the sunlight up to the band edge in a single pass [21]. This is a substantial amount of silicon and would not fare well in the current cost-driven solar industry. The common strategy is to chemically etch the silicon surface to create random roughness, so the normally incident sunlight will acquire an angle upon refraction into the cell and subsequently being trapped within due to total internal reflection. This increases the effective optical path, thus allowing a much thinner wafer to be used. Using this technique, today's industrial standard for crystalline silicon solar cell uses a wafer ~180 μm or less in thickness with texturing and backside reflector [22].

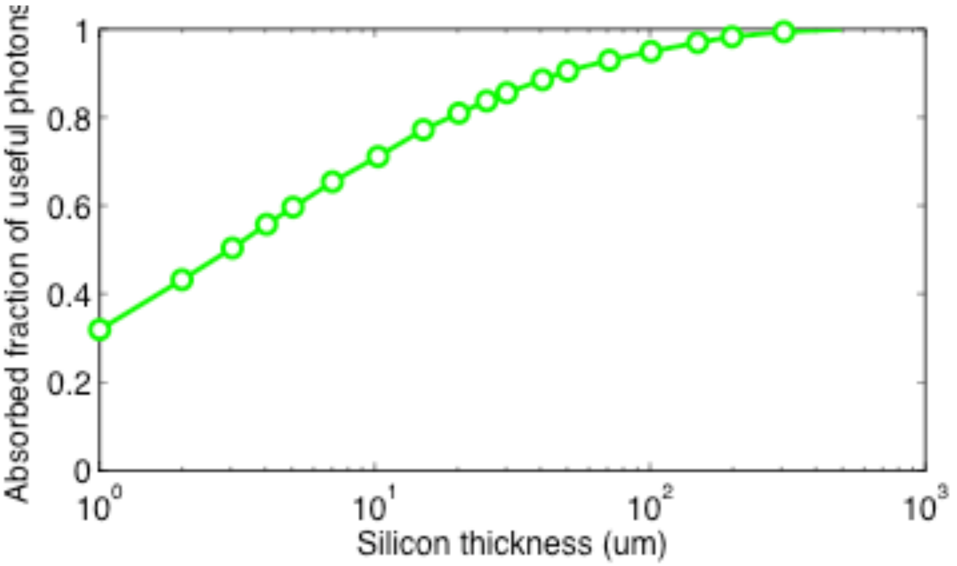

Fig. 1.4. Absorbed fraction of photons above the crystalline silicon bandgap versus the silicon layer thickness. The layer is planar and has no backside mirror.

For thin-film solar cells however, equally effective texturing cannot be realized. Typical thin film solar cells are less than 3 μm thick. This is comparable to the texture roughness on silicon described above, so clearly the method used in silicon cannot be directly applied. A certain degree of surface roughness can be obtained during material deposition, although its effectiveness is fairly limited [23]. Roughness in glass substrates is also used, so the deposited thin film can have better light trapping [24]. Due to these constraints, thin film solar cells commonly use highly absorptive, direct-bandgap semiconductor materials including GaAs, CIGS, CdTe, and CZTS [25].

The techniques discussed so far have been known to the PV community for a long time. For example, the simplest form of anti-reflective coating dates back to 1886 by Lord Rayleigh [26], while the method of using an alkaline solution to etch random pyramid texturing on silicon solar cell was patented in 1979 [27]. Regardless, most solar cells made today, including some with record efficiencies, still rely solely on these techniques to in-couple sunlight with the solar cell. One cannot, however, reach the Shockley-Queisser J_{SC} limit with these techniques alone. For example, corresponding to the random texturing, Yablonovitch and Cody [28] pointed out that random texture could not enhance the optical thickness of a dielectric layer beyond $4n^2$ times, where n is the index of refraction of the dielectric layer. The recent introduction of advanced optical designs in solar cells using, photonic metamaterials and plasmonics can significantly enhance the absorption of solar cells by increasing the local density of photonic states—in some cases even beyond the $4n^2$ ray-optics light-trapping limit [12]. Fig. 1.5 shows some examples of light trapping schemes used in solar cells.

The first obvious application of the advanced optical design is to improve the performance of existing features in the solar cells. Unlike the metals relying on plasmon resonances to screen and reflect the electromagnetic waves, dielectric mirrors are built from layers of dielectric materials with precisely controlled refractive indices and thickness. They cause destructive interference for forward propagating waves, thus reflecting them with great efficiency [29]. In [30], Fink *et al.* presented the general design criterion for a dielectric omni-directional reflector. The dielectric reflector can be tailored to have different bandwidths with high reflection and low loss. In addition, the flexibility of design using 2D/3D photonics extends beyond what the simple layered structures can offer. For example, Bermel *et al.* proposed novel design for thin film c-Si solar cells using 3D photonics [31]. In this work, the power generation of the cell has been improved by deploying various kinds of photonic structures to enhance light absorption. For a solar cell made of a 2 μm thin film of c-Si and a 6 bilayer distributed Bragg reflector (DBR) in the back, 24.0% relative power generation improvement was achieved with a 1D grating, 26.3% improvement by replacing the DBR with a six-period triangular photonic crystal made of air holes in silicon, 31.3% by a DBR plus 2D grating, 26.5% improvement by replacing it with an eight-period inverse opal photonic crystal, and 35% enhancement with a woodpile 3D photonic crystal.

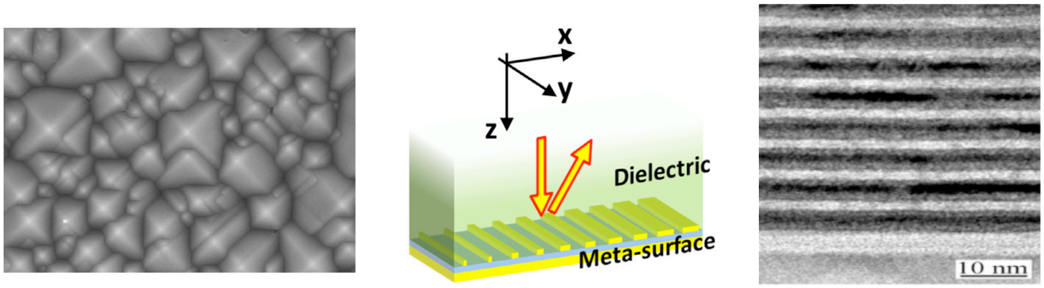

Fig. 1.5. Some light trapping approaches previously explored in the literature: (a) random pyramidal texture used for c-Si solar cells [32], (b) advanced meta-surface trapping light with generalized Snell's law [33], and (c) Bragg reflector for high reflectivity [31].

Advanced optics not only improves single junction effectiveness, but it also opens up new design approaches such as spectral splitting. One of the major losses in the cells approaching the Shockley-Queisser limit is thermalization loss—the high energy photons excite electrons into the conduction band with energy much higher than the bandgap, and the difference is subsequently lost to lattice as heat. One approach minimizing thermalization loss is to split the solar spectrum into various energy bins and send each bin to a solar cell with similar bandgap [34]. This strategy also avoids the current and lattice matching constraints present in stacked multi-junction solar cells. This so-called spectrum splitting technique has seen renewed interest recently as a path to exceed 50% efficiency. Atwater *et al.* takes this approach one step further, and recently proposed various specific designs for spectrum splitting [35-38]. For example, in the so-called polyhedral specular reflector design [37], spectral splitting is achieved indirectly by allowing the sunlight to bounce between two planes of subcells facing each other in parallel. The sunlight will enter the subcell with the highest bandgap first, and then subsequently bounce to the next one with a lower bandgap following a specular optical path. This design thus avoids the use of dispersive material to split the sunlight.

The power of advanced optics is not limited to only improving existing features. It also enables many designs that were previously not possible. One such example is the recent work by Ni *et al.* [39] and Capasso *et al.* [40]. With their own separate efforts, they proposed a photonic layer with an index gradient that creates a tilted escape cone. With each section of the dielectric having a slightly different index of refraction, the incident planewave upon entering the dielectric layer travels at different speed at each section. This effectively tilts the direction of movement of the planewave along with the escape cone toward the section with high index of refraction. As shown by Khan *et al.* [33], this tilted planewave will be confined within the thin film due to total internal reflection and unable to escape. This effectively stretches the optical path for absorption to infinity—something highly desired in solar cells to boost J_{SC}.

Novel non-planar optical structures such as nanowire solar cells, can themselves be tailored to couple to the light favorably. Perhaps one of the most famous examples is the so-called "black silicon". In [41], Her *et al.* developed a process using femtosecond lasers to etch needles on the surface of crystalline silicon. The needles gradually change the refractive index from air to silicon to significantly lower the reflection, causing the silicon to appear black. Zhu *et al.* used the same idea, but with a different approach by etching the silicon base behind a mask array of SiO_2 nanospheres [42]. At the end of the etching, upright standing nanocones are obtained offering a gradient of refractive index similar to the randomly distributed needles in black silicon. The nanocone array achieved a broadband transmission enhancement of ~30% over planar thin film and ~20% over a nanowire array. In a somewhat different approach, Krogstrup *et al.* [43] demonstrated a single standing GaAs nanowire solar cell (instead of an array) could have a self-concentrating effect that captures incoming sunlight at an optical cross-section much larger than its physical wire cross-section. A significantly high J_{SC} of 180 mA/cm^2 is observed under 1-Sun, although it is expected to have lower J_{SC} when made into a nanowire solar cell array. This result is in stark contrast with a similar but horizontally oriented GaAs nanowire solar cell, where a much lower performance is obtained [44]. Nanowire solar cells however suffer from enhanced non-radiative surface recombination losses due to large surface-to-volume ratio. Because of this, nanowire solar cells have so far been significantly inferior to planar, bulk devices. As discussed previously, nanowire can exhibit good absorption, thus the fundamental challenge toward higher efficiency has been to obtain high V_{OC}. This underscores the viability of nanostructures based on InP, whose unpassivated surface has a known surface recombination velocity at ~1000 cm/s, a value orders of magnitude lower compared to other III-V compound such as GaAs under unpassivated conditions [45]. In [46], Wallentin *et al.* reported an InP nanowire array solar cell on InP substrate reaching 13.8% efficiency with a V_{OC} of 0.906 V, which is the current efficiency record for nanowire solar cell.

1.2.2 Toward high V_{OC}

Equally important to enhancing the in-coupling of optical absorption is the suppression of out-coupling of radiative recombination losses, which is the dominant loss mechanism in solar cells approaching the Shockley-Queisser limit. As discussed before, radiative recombination can be effectively suppressed by reabsorbing the photons emitted. The effects of the so-called photon recycling were examined in early work by Stern and Woodall [47]; Lush and Lundstrom proposed to exploit photon recycling in thin-film GaAs solar cells to increase cell performance and decrease material consumption [48]. Thin film GaAs solar cells perhaps benefit the most from photon recycling. GaAs has a high intrinsic material quality with superior absorptivity due to its direct bandgap. It has the ability to absorb 90% of the sunlight within the first micron, and as shown in Fig. 1.2, it has a near-ideal bandgap at 1.44 eV for solar cell application. Furthermore, high quality GaAs thin films can be epitaxially grown with AlGaAs layers to passivate the surfaces to gain low surface recombination. As a result, the internal photoluminescence efficiency, defined as the ratio between radiative recombination and overall recombination, can be as high as 99.7% [49]. One of the most successful examples is the replacement of the backside metallic mirror with highly reflective dielectric mirrors in single junction GaAs solar cells by Alta Devices. The higher reflectivity promotes photon recycling and is the key to reach the record efficiency of 28.8% [50]. Despite such a high efficiency, these GaAs solar cells still fall short of the theoretically predicted Shockley-Queisser efficiency limit of 33.5%. As pointed out in [51], recent efficiency gains are correlated with increasing open circuit voltage (V_{OC}), arising from reducing radiative recombination (R_{rad}) by careful design. Specifically, suppression of R_{rad} is achieved by designing the cell to enhance the photon recycling.

Photon recycling adds additional complexity into the numerical modeling. First, the absorption and emission within the solar cell, in the absence of other losses, must be in detailed balance. This relates the absorption coefficient (α) of the material to the intrinsic radiative recombination coefficient (*B*) that is described by the Roosbroeck-Shockley equation [52]:

$$R_{emit}(V=0)=\int_0^\infty R_{emit}(v)\,dv=\int_0^\infty \frac{8\pi v^2 n^2}{c^2}\frac{\alpha(v)}{e^{hv/kT}-1}dv \tag{1.4}$$

where $\alpha(v)$ is the optical absorption coefficient at wavelength v, and n is the index of refraction.

Second, the reabsorption from radiative recombination must be correctly calculated. Martí showed that Shockley's ideal diode model is equivalent to the detailed balance model, if photon recycling is taken into account [53]. Miller *et al.* [21] analytically calculated the thermodynamic limiting performance of single-junction GaAs solar cells assuming an Urbach tail-like absorption coefficient [54] and the $4n^2$ ray-optics light-trapping limit [55]—both assumptions applied equally to the absorption and emission. In this work, Miller *et al.* pointed out the critical role of having a high internal fluorescence efficiency and high mirror reflectivity for cells reaching high efficiency toward Shockley-Queisser limit. In the absence of a backside mirror, significant amount of radiated photons are lost (0.8 mA/cm^2) at the MPP [21]. This constitutes approximately 98% of the radiative recombination loss! Durbin *et al.* [56] conducted more elaborate efforts and incorporated the photon recycling into a 1D device simulator, ADEPT [57]. In his approach, the radiative recombination at each location within the device emits photons isotropically, and the optical re-absorption at other locations is then calculated via Beer's law. Such approach is well suited for layered solar cell structures that are well within the ray optics limit.

1.3 Thesis Overview

This thesis explores high efficiency solar cell designs approaching the Shockley-Queisser limit. The thesis is organized as follows:

- In Chapter 2, we study the record efficiency, single-junction GaAs thin-film solar cell. At 28.8% efficiency, this cell is close to its Shockley-Queisser limit of approximately 33%. We see how the 1D electro-optically coupled approach is able to model this structure in a thermodynamically sound fashion. The remaining design challenges and critical parameters for this cell are also discussed.

- In Chapter 3, we develop a wave optics-based, 3D electro-optically coupled approach to study a nanowire solar cell. Due to its unique, nanoscale geometry, the nanowire solar cell displays distinctly different behaviors than regular, planar thin film solar cells. As a result, its design follows a different principle.
- In Chapter 4, we investigate the reciprocity theorem between absorption and emission inside a solar cell. These two quantities are closely related through the Rau's Reciprocity Theorem, but its validity depends on certain conditions. In this work, we use the electro-optically coupled simulation to test the reciprocity theorem and show that the superposition principle is a prerequisite for it to hold.
- In Chapter 5, we apply the electro-optically coupled simulation to solar cell characterization. Luminescence-based characterization techniques are powerful, contactless methods in assessing the quality of the PV material before it is incorporated into solar cells. In this work, we show a combined approach coupling the time-resolved photoluminescence (TRPL), photoluminescence excitation spectroscopy (PLE), and the electro-optically coupled simulation together to extract quantitative information regarding the lifetimes inside an InP thin film.
- In Chapter 6, the design of a GaInP/GaAs tandem junction solar cell is studied using the electro-optically coupled approach. The study reveals the importance of the minority carrier reflectors, internal radiative efficiency of the materials, and the backside mirror in achieving high conversion efficiency.
- In Chapter 7, we summarize the thesis and provide suggestions for future work.

2 DESIGN OF GAAS SOLAR CELLS TOWARD THE SHOCKLEY-QUESSIER LIMIT

2.1 Preface

The contents of this chapter have been extracted from the following publications with permission: X. Wang, M. R. Khan, M. A. Alam, and M. Lundstrom, "Approaching the Shockley-Queisser limit in GaAs solar cells," in *IEEE Photovoltaic Specialists Conference*, 2012, pp. 002117-002121; X. Wang, M. R. Khan, J. L. Gray, M. A. Alam, and M. S. Lundstrom, "Design of GaAs Solar Cells Operating Close to the Shockley–Queisser Limit," *IEEE Journal of Photovoltaics,* vol. 3, pp. 737-744, 2013.

2.2 Introduction

The efficiency of thin film single junction GaAs solar cells has improved substantially in the past several years, reaching impressive efficiencies above 28% [7, 58, 59]. Despite such a high efficiency, these GaAs solar cells still fall short of the theoretically predicted Shockley-Queisser efficiency limit of 33.5% [21], leaving room for additional improvement. This chapter is a numerical design study that seeks to clarify the device physics that limits performance of thin film GaAs solar cells.

As pointed out in [51], recent efficiency gains are correlated with increasing open circuit voltage (V_{OC}) arising from reducing radiative recombination (R_{rad}) by careful design. Specifically, suppression of R_{rad} is achieved by designing the cell to enhance so-called photon recycling, which can be explained as follows. High-quality GaAs double heterostructures are dominated by radiative recombination, with internal quantum yields of more than 99% [49]. In these thin film structures, photons emitted by radiative recombination can be re-absorbed (recycled) many times before escaping the cell, thereby effectively increasing the radiative lifetime [60]. The effects of photon recycling were examined by Stern and Woodall [61]; Lush and Lundstrom subsequently proposed to exploit photon recycling in thin-film GaAs solar cells to increase cell performance and decrease material consumption [48]. Martí *et al.* [53] showed that the Shockley diode model is equivalent to the detailed balance model if photon recycling is taken into account. Recent advances in cell design and fabrication exploit photon recycling effects and have brought the efficiency of single junction thin-film GaAs solar cell close to fundamental limits. Miller *et al.* have discussed the fundamental processes that limit GaAs solar cell performance from a thermodynamic perspective [21]. Our goal is to do so from a device physics and design perspective and, in the process, to determine the practical limits of cell efficiency.

Numerical simulation is a powerful tool for optimizing the design of high-efficiency solar cells [62]. When cells operate near their ultimate efficiency limit, however, care has to be taken to ensure the simulation is thermodynamically sound. Most numerical simulation codes are not. At V_{OC}, photogeneration within the cell is in detail balance with recombination within the cell. For GaAs, most of the recombination occurs radiatively, but radiative recombination is not a loss, provided the photon is subsequently reabsorbed within the cell. At V_{OC}, in the absence of nonradiative recombination, one photon must leave the cell for every photon that is absorbed. This thermodynamic balance sets the upper limit to solar cell efficiency.

This chapter explores practical issues of GaAs solar cells operating near the thermodynamic limit using detailed numerical simulations that include both electrical transport and optics. Electrical transport is well understood. The first step, therefore, is to properly construct a numerical device simulation including photon recycling in a way that is consistent with electrical transport. Our self-consistent electrical-optical model is discussed in Sec. 2.3. In Sec. 2.4, we simulate a baseline cell structure as a starting point. Sec. 2.5 is a design study, which examines how solar cell device parameters affect performance near the fundamental limit. Insights from the design study suggest a strategy for further efficiency improvement, as discussed in Sec. 2.6. Our conclusions are summarized in Sec. 2.7.

2.3 Approach

2.3.1 Efficiency Limit in GaAs Solar Cells

The well-known Shockley-Queisser limit [9] is a material-dependent upper limit to solar cell performance. In practice, nonradiative recombination and other losses reduce the efficiency below this limit. In addition, there is also an upper limit for the effectiveness of light trapping [15, 55]. This light-trapping limit is structure dependent, which means that the upper limit performance of a solar cell is both material and device dependent. In the discussion below, we focus on planar cells with an anti-reflection coating (ARC).

2.3.2 Radiative Lifetime Enhancement by Photon Recycling

Photon recycling is a two-step process; photons are first emitted by radiative recombination and then a fraction is subsequently re-absorbed (recycled) elsewhere in the device. The net effect is a reduction of the rate of radiative recombination.

Intrinsic radiative recombination (denoted by R_{emit} here) is typically described by the B-coefficient:

$$\begin{aligned} R_{emit}(\vec{r}) &= B\left(np - n^2_i\right) = Bn^2_i\left(e^{q\left(F_n(\vec{r})-F_p(\vec{r})\right)/kT} - 1\right) \\ &\approx Bn^2_i e^{q\left(F_n(\vec{r})-F_p(\vec{r})\right)/kT} \end{aligned} \tag{2.1}$$

where $F_n(\vec{r})$ and $F_p(\vec{r})$ are positional dependent quasi-Fermi level for electron and hole respectively. Thus, one straightforward way to incorporate photon-recycling effects in device simulation is to reduce the intrinsic radiative coefficient (or equivalently, enhance the intrinsic radiative lifetime) by reducing B-coefficient according to

$$R_{rad}(\vec{r}) \equiv R_{emit} - G_{recycle} \approx \frac{B}{\phi_r} n^2_i e^{q\left(F_n(\vec{r})-F_p(\vec{r})\right)/kT} \tag{2.2}$$

where ϕ_r is the so called photon recycling factor (Asbeck factor [63]), B is the intrinsic radiative recombination coefficient, $G_{recycle}$ is the absorption rate of recycled photons, and R_{rad} is the effective radiative recombination rate as a result of photon recycling.

The limitation of this simple approach is the lack of physically meaningful, well-defined connection between the chosen recycling factor ϕ_r and other parameters such as device geometry and material properties. In addition, the recycling factor has no apparent upper bound to prevent a violation of thermodynamic limit. Thermodynamically, the two steps —intrinsic radiative recombination and recycling of emitted photons are self-consistently related.

Radiative recombination is an intrinsic property of any material at a finite temperature, and it is related to the absorption coefficient by the Roosbroeck-Shockley equation [52],

$$R_{emit}(V=0)=\int_0^\infty R_{emit}(v)dv=\int_0^\infty \frac{8\pi v^2 n^2}{c^2}\frac{\alpha(v)}{e^{hv/kT}-1}dv \qquad (2.3)$$

where *α(v)* is the optical absorption coefficient at wavelength *v*, and *n* is the index of refraction. The condition *V*=0 indicates this equation applies at equilibrium. Away from equilibrium the quasi-Fermi levels split, so that

$$R_{emit}(\vec{r})=R_{emit}(V=0)e^{\left(F_n(\vec{r})-F_p(\vec{r})\right)/kT} \qquad (2.4)$$

For thermodynamic consistency of the *B* coefficient, equation (1) and (4) must agree, and therefore,

$$B=\frac{8\pi n^2}{n_i^2 c^2}\int_0^\infty \frac{v^2\alpha(v)}{e^{kv/kT}-1}dv \qquad (2.5)$$

The Roosbroeck-Shockley equation connects the electrical radiative recombination and optical absorption coefficient of the material. The *B* coefficient is not an independent input, but rather it is determined from absorption coefficients.

Equation (2.5) is an integral across all wavelengths, but most of the emission occurs in a very narrow wavelength range near the GaAs bandgap. The *B* coefficient is closely related to the area under this narrow region as suggested in (2.5), so that an accurate knowledge of near band-edge absorption coefficient is essential for quantitative calculation of intrinsic radiative recombination.

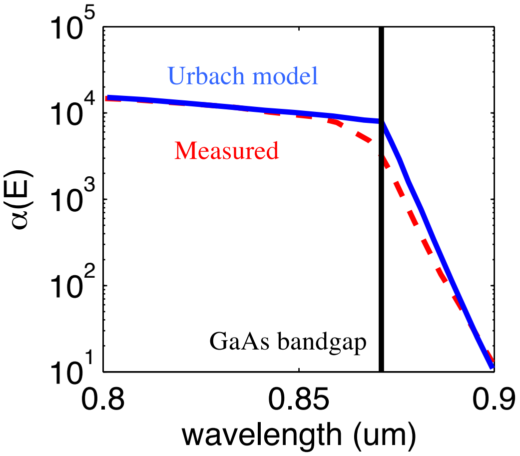

	B coefficient
Urbach model	6.7×10^{-10} /cm^{3}s
Lush	5.0×10^{-10} /cm^{3}s
Varshni	7.2×10^{-10} /cm^{3}s

Fig. 2.1. Comparison among different intrinsic GaAs absorption coefficients as a function of wavelength close to the GaAs bandedge (left graph) and the corresponding effective recombination coefficients (table on right).

Fig. 2.1 shows a comparison between three sets of intrinsic absorption coefficients: an analytical “Urbach tail” model described in [54], experimental data from Lush [64], and the commonly cited *B*-coefficient value from Varshni [65]. The differences near the bandgap energy translate to an approximate 25% difference in B coefficient. The absorption coefficient of GaAs is well known to depend on doping [64, 66]. In this study, we will use the data from Lush *et al.* [9] which was measured on a 1.3×10^{17} /cm^3 doped n-type GaAs sample.

After describing radiative emission correctly, the second step in photon recycling involves treating reabsorption of these emitted photons. Photons are emitted isotropically, and ray-tracing methods can be used to trace each emitted ray at each angle and each wavelength in the emission spectrum for each solution node within the device [67].

2.3.3 Self-consistent Photon Recycling with the Semiconductor Equations

In this study, we augment ADEPT 2.0, which solves the semiconductor device equations, by photon recycling based on an approach similar to that of Durbin [56]. ADEPT 2.0 is a 1D self-consistent solar cell simulator capable of simulating layered structures. The simulator is well calibrated, numerically sound, and is available on web [57]. In brief, the solution scheme is as follows.

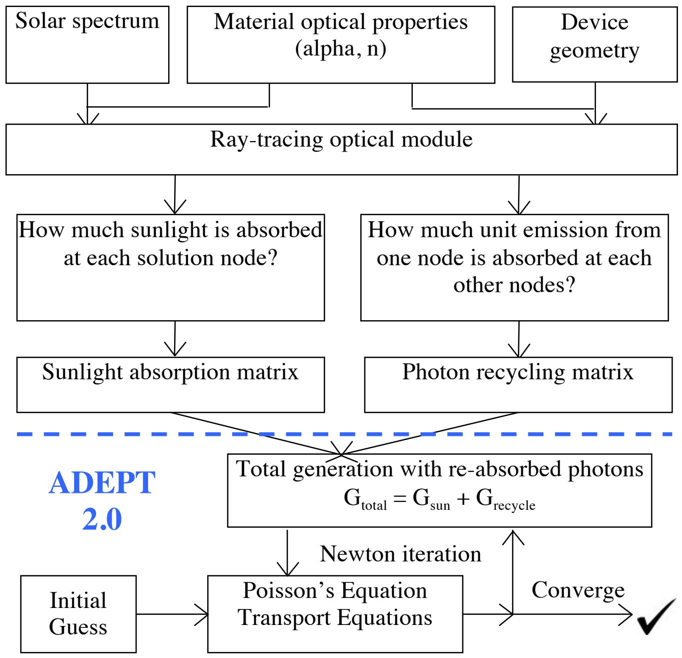

Fig. 2.2. Overall scheme for ADEPT 2.0 upgraded with the addition of a photon recycling module.

We begin by calculating the response matrix (see Fig. 2.2), which quantifies how much absorption occurs at every other node in response to a unit radiative recombination event occurring at a specific node. The optical module traces the isotropically emitted photons from the unit radiative recombination event at every possible angle throughout the structure and determines the absorption at each node. This unit response matrix termed “photon recycling matrix” is then passed on to ADEPT 2.0 for the electrical calculation. To ensure consistency, the same ray-tracing module handles the incoming sunlight absorption calculation as well, and the resulting “sunlight absorption matrix” is also passed onto ADEPT 2.0. For a general discussion regarding ray-tracing simulation in solar cells, see [68]. ADEPT 2.0 couples the generation from the two matrices, the electron and hole transport equations, and Poisson’s equation into one single Jacobian matrix and uses Newton’s method to iterate to the final solution. After each Newton step,

R_{emit} is updated with the new local quasi-Fermi level splitting. After obtaining the new R_{emit}, a generation rate due to photon recycling, $G_{recycle}$, is re-calculated. The process continues until convergence is achieved. The model is tested by switching off all non-radiative processes and ensuring that the results give the correct thermodynamic upper limit of efficiency.

2.4 Device Structure

With this thermodynamically consistent model, we can study realistic GaAs solar cells that operate close to the upper limit of efficiency. In this study, we begin with a model structure shown in Fig. 2.3. In Sec. 2.5, we then identify the key loss mechanisms and determine the most important device parameters that limit the efficiency in practice.

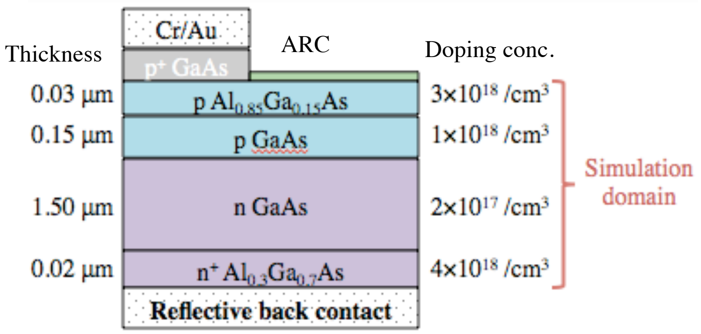

Fig. 2.3. Idealized single junction GaAs thin film solar cell with reflective back contact.

The model device is a single junction GaAs solar cell structure that resembles a recently reported cell [7]. Specifics of the structure in [7] have not been reported, so we make no effort to match experimental data precisely. Our goal here is to use a reasonable device structure and investigate the effects of various key design parameters that affect the performance of these kinds of solar cells.

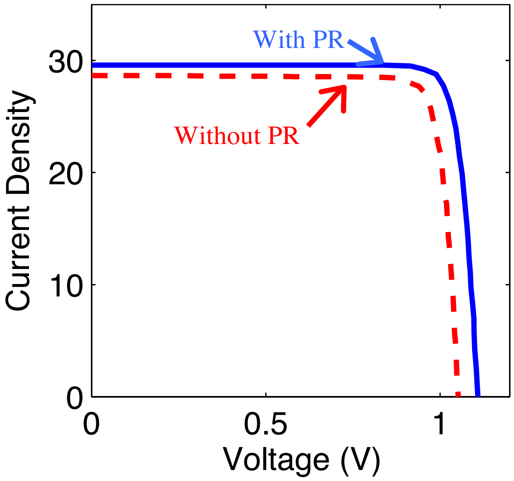

	Baseline (with PR)	**Ref. [7]**
V_{OC}	1.107 V	1.107 V
J_{SC}	29.49 mA/cm^2	29.47 mA/cm^2
FF	0.867	0.867
Eff.	28.35%	28.3%

Fig. 2.4. Left: Baseline light IV characteristics with (blue solid line) vs. without (red dashed line) photon recycling. Right table: The key metrics (Voc, Jsc, and FF) obtained for the baseline cell with photon recycling effects (blue solid line on the left) matches those reported in ref. [7] closely.

Fig. 2.3 summarizes the model cell structure and several key parameters. The structure is typical for single junction GaAs solar cells by epitaxial liftoff. The cell features a heavily doped p-type GaAs thin emitter (0.15 μm) and lightly doped n-type GaAs base (1.5 μm). Two thin high-bandgap doped AlGaAs layers at front and back form heterojunctions with GaAs, effectively deflecting minority carriers away from contacts to decrease surface recombination. A metallic mirror is placed on the back, which also serves as backside contact. An ARC is typically used on the front to reduce sunlight reflection. For this study, an ARC is not explicitly simulated, so the front reflection loss is summed into shadowing loss, producing a total loss of 6.6%. This percentage was determined by matching the short circuit current reported in [58]. The backside mirror reflectivity was taken from [59].

The escape of photons through the front surface is am important loss mechanism in these cells. The escape cone depends on the ambient index, *n*, but diffraction effects in the ARC are expected to increase the escape cone somewhat. Photon transport through the ARC is not treated. Instead, we use an ambient index of n =1.35 in an attempt to mimic transmission through the stack of GaAs/ARC (160 nm)/Air by making the front escape cone slightly larger than that of air/GaAs interface. We compared calculations with an ambient index of refraction $n = 1$ to those with $n = 1.35$ and found only a slight increase of 7 mV in V_{OC}, which shows that the specific choice of the ambient index used in modeling has a relatively minor impact compared to the parameters (SRH lifetime, mirror reflectivity, device width, etc.) we focus on in this chapter.

The SRH lifetime (0.5 μs) and the Auger coefficients (7.0x10^{-30} cm^6/s) are reported in [59]. Finally, a series resistance of 0.7 Ω is used to match fill factor reported in [7]. In our simulation, we have assumed that the perimeter recombination is negligible. Therefore, comparison between theory and experiment is rigorously justified only for GaAs solar cells with passivated edges [69]. (To first order, edge recombination could be viewed as an effective decrease in bulk SRH recombination lifetime.) With these assumptions, the simulated baseline cell shows performance similar to that of the cell reported in [7] (see Fig. 2.4).

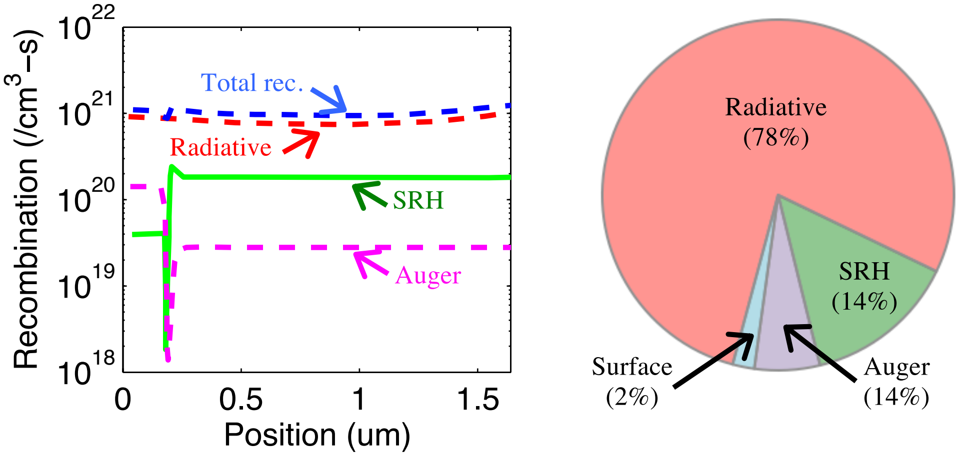

Fig. 2.5. Radiative, SRH, and Auger recombination within baseline cell at V_{OC}. (a) Recombination rate vs. position. (b) Integrated recombination rate at V_{OC} for radiative recombination (Radiative), bulk SRH recombination (SRH), Auger recombination (Auger), and surface SRH recombination (Surface). "Position" on x-axis corresponds to the depth relative to sun-facing cell surface. Backside mirror is located at the right end of the x-axis. (See Fig. 2.3)

As discussed in [7], most of the efficiency gain in this thin film cell, as compared to its substrate counterpart, is achieved through a substantially higher V_{OC}. Fig. 2.5 shows a comparison of various recombination losses in the device. Radiative recombination (intrinsically emitted minus recycled) dominates throughout (at V_{OC}) the cell structure and is responsible for ~80% of total recombination. The rest is mainly due to SRH recombination. The heterojunction interfaces formed by AlGaAs/GaAs serve as excellent minority carrier mirrors at both the front and back, thus surface recombination is very low (~ 2%), and therefore not shown in the Fig. 2.5.

2.5 Results

With a baseline structure defined, we now proceed to investigate some design parameters and determine the most important loss mechanisms. In this section, we first establish an upper limit for this baseline cell as reference. We then examine the effects of the backside mirror (Fig. 2.8), SRH recombination (Fig. 2.9), series resistance (Fig. 2.10), and cell thickness (Fig. 2.11) with respect to the baseline structure to understand how each of these loss factors reduces the cell efficiency from the upper limit.

2.5.1 Fundamental Limits

The Shockley-Queisser limit is derived by using detailed balance between absorption of incoming photons from sunlight and radiative emission at cell's temperature described by Planck's law. Since the updated ADEPT 2.0 simulator is thermodynamically consistent, the Shockley-Queisser limit can also be obtained by requiring that all parameters satisfy four Shockley-Queisser conditions: 1) complete absorption, 2) maximum angle entropy [15], 3) no transport bottleneck, and 4) absence of nonradiative recombination.

To ensure that all incident photons with energy higher than GaAs bandgap are completely absorbed at the cell surface we customize the GaAs absorption coefficient to be artificially high (e.g., 10^7/cm) for energies above GaAs bandgap and zero for those below (step-like). We ensure that the performance of the cell (V_{OC}, J_{SC}, FF) at the thermodynamic limit is insensitive to the exact value of the absorption coefficient.

To ensure the maximum angle-entropy implied in the SQ paper, the emission out of the cell must occur at the surface with 2π sr. Therefore, we set the index of refraction for all solar cell layers to be 1 (same as air), effectively making the front escape cone to be 2π sr. to avoid any angle restriction.

To make sure the carriers are collected as soon as they are generated, carrier mobilities are set to very high value (10^8 cm^2/V-s. Finally, *all* non-radiative recombination processes (including the fundamental Auger process) are set to zero to be consistent with the SQ assumptions.

Fig. 2.6 shows the simulated IV from ADEPT 2.0 with the Shockley-Queisser assumptions compared to that obtained from analytical calculation based on detailed balance; the results are identical, as expected. This verifies that the detailed balance model was correctly implemented in the numerical simulation.

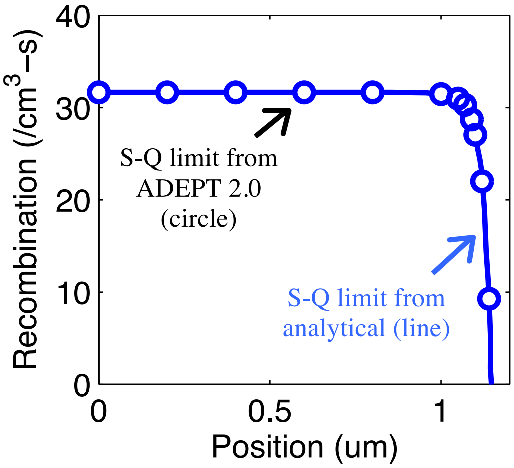

	Shockley-Queisser	**Optical Planar**
V_{OC}	1.12 V	1.14 V
J_{SC}	33.5 mA/cm^2	31.9 mA/cm^2
FF	0.89	0.89
Eff.	33.5%	32.7%

Fig. 2.6. Left: Comparison of IV at Shockley-Queisser limit by analytical detailed balance method (solid line) and ADEPT 2.0 (black filled circles). Right: Characteristic parameters for Shockley-Queisser limit are compared to a planar cell in the table.

We now define the “Optical Planar Limit” by removing the first of the four constrains that define SQ limit, namely, that of complete absorption. Recall that, in practice, the absorption coefficient in GaAs is finite [9] and therefore photon absorption in 1.5 μm baseline cell, even with photon recycling, is necessarily imperfect. Therefore, even if the mobilities are presumed infinite and non-radiative recombination is absent (just as in Schockley-Queisser analysis), the cell efficiency calculated from ADEPT 2.0

with finite absorption and photon recycling is still lower that of the Shockley-Queisser limit.

The table in Fig. 2.6 compares the Shockley-Queisser limit to the planar optical limit. Although the planar optical limit is lower in efficiency, its V_{OC} is *higher* than that of Shockley-Queisser limit. One can also appreciate this difference in V_{OC} from a detailed balance point of view. The imperfect absorption of the planar cell causing it to have lower absorbance near band edge comparing to the perfectly absorbing cell in case of Shockley-Queisser limit, as if the planar cell has a larger bandgap, and thus a higher V_{OC} results [21]. In this study, we focus exclusively on cells defined by parallel planar surfaces.

2.5.2 Effects of Backside Mirror

The backside mirror plays a special role in thin film GaAs solar cells. Traditionally, a metallic backside contact reflects incident sunlight (that is not absorbed in the first pass through the material) back toward the front of the cell to enhance overall absorption and increase J_{SC}. In thin film GaAs solar cells where radiative recombination dominates, it serves another critical role of reflecting *radiatively* emitted photons and contributing to photon recycling.

As discussed in Sec. 2.3, the emission spectrum peaks around a narrow region near the material's bandgap energy, where the absorption coefficient transitions from high to low. Emitted photons travel several passes within the device before they are re-absorbed, because unless the photons are emitted within the escape cone or absorbed by a non-perfect backside mirror, they are forever trapped within the planar parallel surfaces. Therefore, a radiatively emitted photon within planar device with an incident angle to the planar surface outside of the escape cone will bounce around the structure and eventually be recycled—unless it is absorbed, lost at the backside mirror, or escapes through the edges of the cell. This means a typical photon has to strike the backside mirror several times before it is recycled. As a result, efficiency reductions from a lossy backside mirror are mostly due to a reduction in V_{OC} rather than J_{SC}—an important point that is also emphasized in [21].

In the case of a non-perfect backside mirror reflectivity (< 100%), the photons trapped by guiding modes are mostly lost to the mirror after repeatedly striking the backside. The absorption length is about 100 μm for photons having GaAs bandgap energy. For a 1 cm x 1 cm cell, this translates to an edge-emission affected area of 0.0199 cm^2, which is roughly 2% of total cell area.

The front escape cone is determined by the difference in the indices of refraction. This escape cone is ~4% of 2π sr, so that R_{front}~96%. Given the high front reflectivity, the design of back mirror becomes critically important. The back mirror reflectivity used in this study ($R_{back} = 0.85$) is appropriate for a metallic mirror in contact with AlGaAs (see Fig. 2.3). This reflectivity is higher than that of a mirror exposed in air (n=1) due to the difference in medium indices. The internal spatial profiles of emission and generation due to photon recycling are complex (Fig. 2.7), so we spatially integrate the total. Fig. 2.7 (top) plots the ratio of the loss of photons through the back surface to the loss through the front surface as a function of the back mirror reflectivity. The photon loss associated with the backside mirror can be interpreted as an effective escape probability, i.e. the probability of “escape” is proportional to the number of times a photon bounces off the mirror. The losses are seen to be approximately equal when the front and back surfaces have about the same reflectivity.

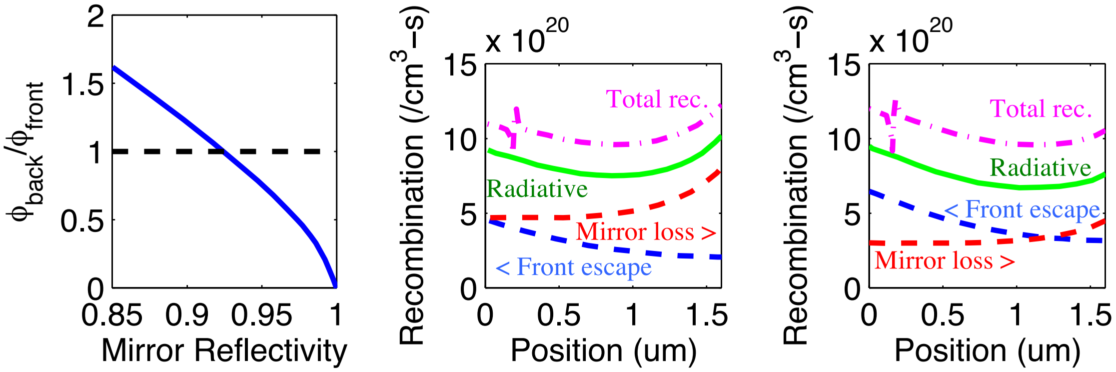

Fig. 2.7. Top: Ratio of the loss of photons through the back surface to the loss through the front surface as a function of back mirror reflectivity. Bottom: For 85% and 95% mirror reflectivity, shown here is the percentage of emitted photon escaping from front and losing at backside mirror at different location within the device under open circuit condition. "Position" on x-axis corresponds to the depth relative to sun-facing cell surface. Backside mirror is located at the right end of the x-axis. (See Fig. 2.3)

Fig. 2.8 shows the influence of backside mirror reflectivity on V_{OC}, J_{SC}, and efficiency. As expected, enhancement in backside mirror reflectivity above ~85% mostly affects the V_{OC}. Since GaAs is already a good absorbing material, most of the light is absorbed during the first pass through 1.5 μm base, and backside mirror reflectivity brings minor improvement to J_{SC}. Worth noticing is a superlinear improvement on V_{OC} with increasing mirror reflectivity. This is especially true for high quality mirrors (> 85%), indicating a substantial opportunity toward higher efficiency. This detailed calculation supports the simpler analysis of [21]. Design of sophisticated mirrors with high reflectivity, however, may not only be nontrivial, but also expensive.

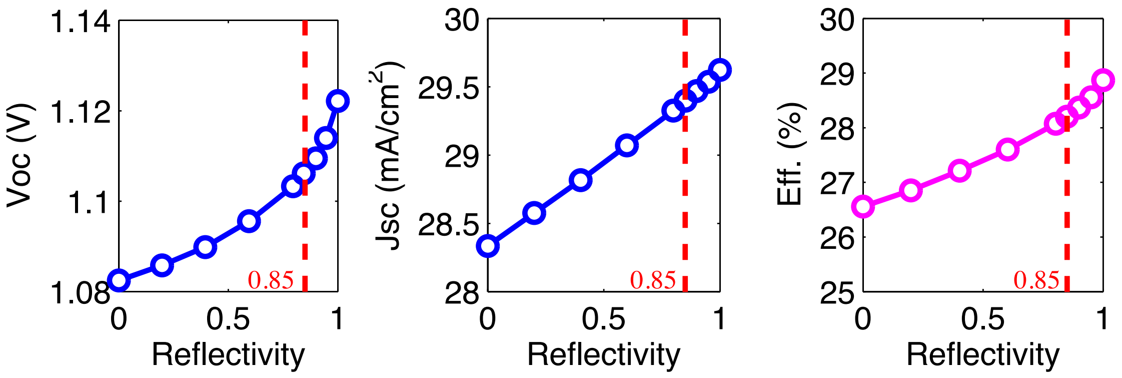

Fig. 2.8. V_{OC}, J_{SC}, and efficiency as a function of backside mirror reflectivity. The marked 0.85 reflectivity is used in baseline case.

2.5.3 Effects of SRH Recombination

Radiative recombination losses can be minimized by photon recycling, but non-radiative recombination including SRH, Auger, surface recombination, and other losses will inevitably be present. Auger recombination is a fundamental loss and cannot be avoided, but its effect on cell performance is minimal. SRH recombination on the other hand is responsible for ~20% of all recombination losses with the assumed 0.5 μs lifetime.

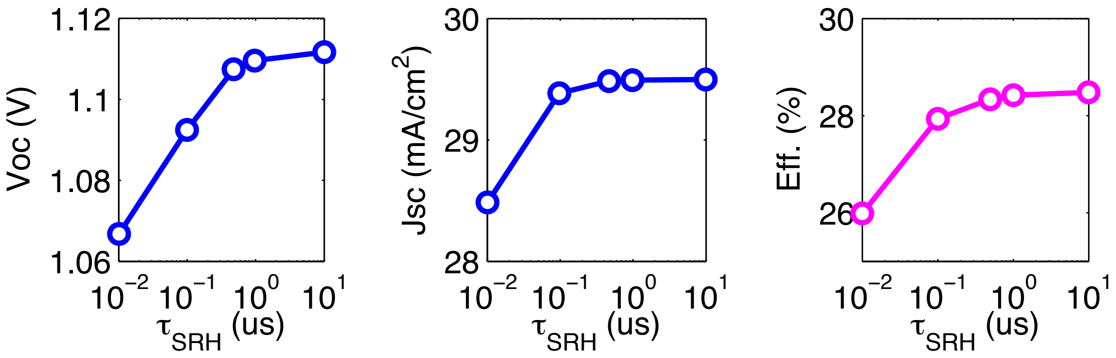

Fig. 2.9. V_{OC}, J_{SC}, and efficiency as a function of SRH lifetimes. Notice the log scale used on x-axis.

Fig. 2.9 shows how V_{OC}, J_{SC}, and efficiency vary with SRH lifetime from 0.01 μs to 10 μs. SRH lifetimes of 1 μs are achievable, so it appears that SRH lifetime is not a significant limiting factor for further improvement in efficiency. Note that V_{OC}, J_{SC}, and efficiency all saturate for very high SRH lifetime. This is because at high SRH lifetime, radiative recombination becomes the dominant loss mechanism, and cell performance is thus insensitive to further increases of the SRH lifetime.

2.5.4 Effects of Series Resistance

Series resistance introduces significant loss in efficiency by lowering the fill factor (FF). The two most recent reports on record efficiency cells confirmed by NREL benefitted mostly from an improvement in FF, while J_{SC} and V_{OC} saw no major change. This is most likely due to a lowering of series resistance. Fig. 2.10 shows the impact on FF and efficiency due to different series resistance values. Efficiencies appear to degrade almost linearly (~1%/Ω) with increasing series resistance.

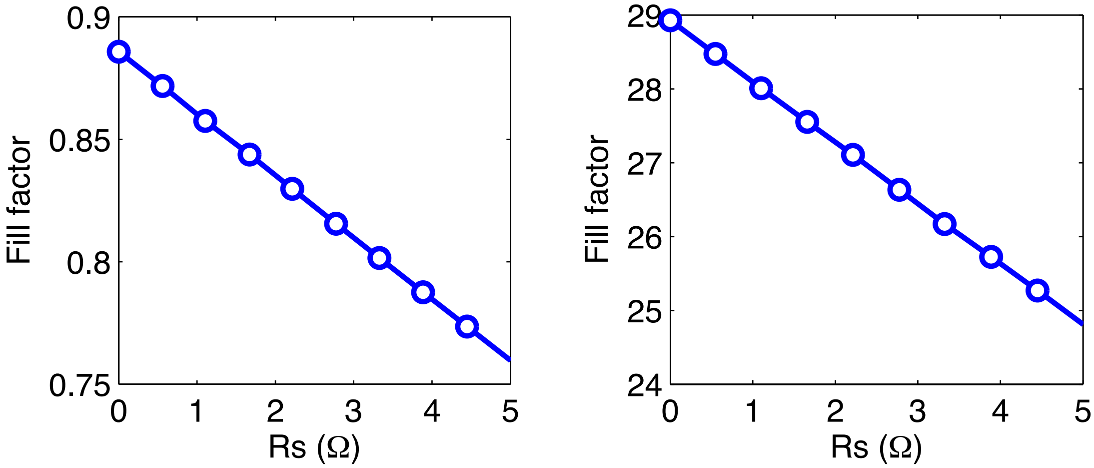

Fig. 2.10. Fill factor and efficiency as a function of different series resistance values. The cell has an area of 1 cm^2.

2.5.5 Effects of Base Thickness

One major improvement in single junction GaAs solar cell comes from the benefits of having a thin base. Compared to a substrate design, a thin film has the advantage of a lower overall recombination region due to a reduction of base thickness and a decrease in radiative recombination since the backside mirror aids in photon recycling.

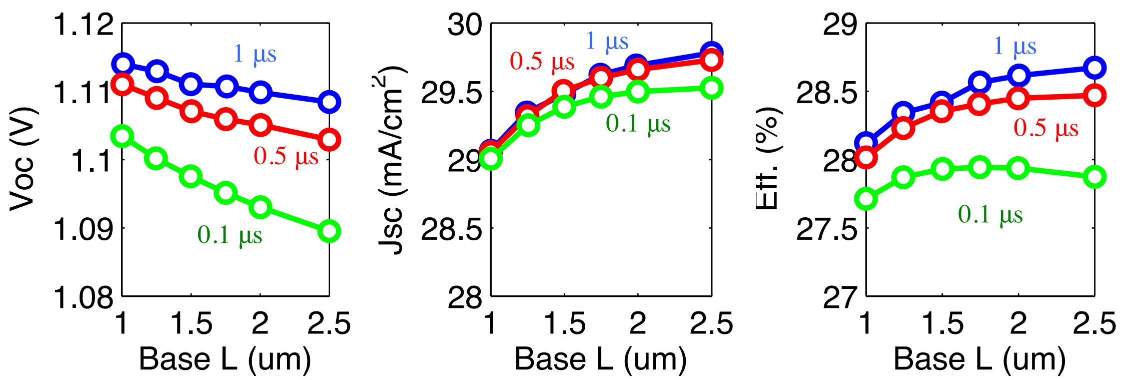

Fig. 2.11. V_{OC}, J_{SC}, and efficiency as a function of base thickness for three different SRH lifetimes.

Any increase in base thickness (see Fig. 2.11) produces a small increase J_{SC} due to more complete absorption of sunlight. The V_{OC} however decreases due to a larger volume available for recombination. As a result, the change in overall efficiency is rather small. The detailed impact of base thickness on radiative recombination is related to the backside mirror discussion in subsection B. As the base thickness shrinks, emitted photons need to strike the backside mirror more frequently. This significantly increases losses due to the backside mirror. Therefore, it is a trade-off between more pronounced backside mirror loss and less region for radiative recombination to occur—a quantitative connection that only a detailed numerical calculation can precisely capture.

2.5.6 Summary of Loss Mechanisms

As a summary of results, Fig. 2.12 shows a detailed breakdown of efficiency decreases introduced by various loss mechanisms. This chart is an illustrative way of showing how much the cell efficiency is degraded with each loss mechanism, starting from the Shockley-Queisser limit on the left. Although this plot is specific to the particular device, and adding the losses in a different order would yield a different efficiency at each step, Fig. 2.12 serves the purpose of identifying the most important loss factors. The overall efficiency is degraded by a lower J_{SC} due to finite absorption ("S-Q Limit" -> "Planar Optical"), despite a slightly higher V_{OC} from restriction of emission angles. Efficiency suffers significantly (to 30.5%) by 6% shadowing, front-side sunlight reflection, and any other parasitic losses in the ARC/TCO layers ("Planar Optical" -> "Shadowing/Refl."). An imperfect rear mirror with 85% reflectivity further lowers the efficiency by reducing V_{OC} ("Shadowing/Refl." -> "Rear Mirror Loss"). Auger recombination is much less significant comparing to SRH recombination ("Rear Mirror Loss -> "Auger Loss" -> "SRH Loss"). In the end, a 0.6 Ω R_S causes further degradation of the efficiency to 28.35% ("SRH Loss" -> "Series R. Loss").

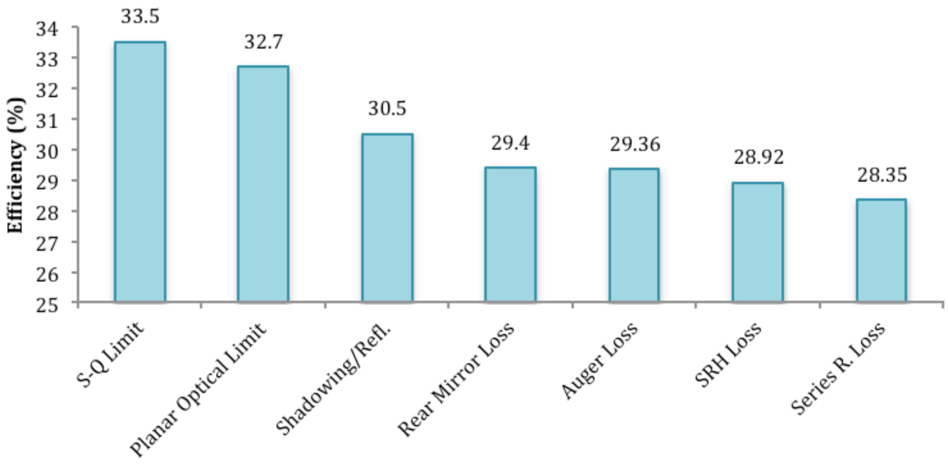

Fig. 2.12. List of loss mechanisms considered in this study and their impact on baseline cell efficiency.

2.6 Discussion

In this chapter, we have studied the effects of various design parameters including SRH recombination, backside mirror reflectivity, series resistance, and cell base thickness, on the practical efficiency limit of single junction thin film solar cells. As single junction GaAs solar cells approach the ultimate limit, critical and controllable parameters have been pushed to be close to best experimentally achievable values, so that the gap between the theoretical and experimental limits is reduced.

Not all design parameters can contribute equally in closing the remaining gap. For example, our calculation shows that further improvements in SRH lifetime or optimization of base thickness would not increase the efficiency significantly. On the other hand, improvements on backside mirror reflectivity beyond 95% will increase the efficiency superlinearly (see Fig. 2.8), therefore, back mirror reflectivity and series resistances are two most important parameters to focus on to create highest efficiency thin film solar cells.

These conclusions can also be understood by an intuitive argument proposed by Ross [70]. With nonradiative losses such as the backside mirror loss, the V_{OC} is degraded from its thermodynamic maximum:

$$V_{oc} = V_{oc-max} - kT\ln(k) \tag{2.6}$$

where k (≥ 1) is the ratio between total recombination and radiative recombination at V_{OC}—the inverse of what is known as the external fluorescence efficiency η_{ext}. If backside mirror loss is the dominant non-radiative loss mechanism, its improvement makes the loss term approaches zero logarithmically.

Besides the backside mirror, another opportunity to improve efficiency involves lowering series resistance, as seen in Fig. 2.10. This can be achieved by optimizing the grid design [71]. In the module level, methods such as novel interconnection schemes reducing resistance have also been suggested [72].

Finally, in discussing *practical* efficiency limits, it is important to understand the role of the various uncertainties and assumptions introduced in the simulation. For example, in (5), the choice of the intrinsic carrier concentration, n_i influences radiative recombination rate. Since n_i is related to the material bandgap, which is connected to the absorption coefficient, a connection between n_i and optical properties has to be made. This connection is absent at present in our model. Moreover, our choice of ambient index with an effective value of 1.35 is an attempt to model the correct front escape cone. Rigorous optical simulation of the ARC layers with wave effect is needed to accurately model the frequency dependent transmission and will be a topic of future study.

2.7 Summary

Designing GaAs solar cells to operate close to the ultimate efficiency limit requires careful device optimization guided by models that accurately incorporate thermodynamic limits. In this chapter, we have discussed how to properly simulate solar cells that operate near the thermodynamic limit and have developed a self-consistent device simulator, which includes the thermodynamic limits. In addition, we have conducted a design study that identifies the key loss factors limiting the cell efficiency. We conclude that a good backside mirror and very low series resistance are the most important factors for future improvement in cell efficiency. Non-radiative recombination plays a smaller role as long as SRH lifetime greater than 0.5 μs can be maintained. Losses due to shadowing and reflection can also be significant, but may be difficult to decrease substantially. Therefore, the most promising strategy toward ultimate efficiency for single junction GaAs solar cell is to focus on building advanced backside mirrors and developing techniques to achieve very low series resistance.

3 DESIGN OF NANOWIRE SOLAR CELLS TOWARD THE SHOCKLEY-QUEISSER LIMIT

3.1 Preface

The contents of this chapter have been extracted from the following publications with permission: X. Wang, M. R. Khan, M. Lundstrom, and P. Bermel, "Performance-limiting factors for GaAs-based single nanowire photovoltaics," *Optics Express,* vol. 22, p. A344, 2014.

3.2 Introduction

It is commonly understood that with the advent of low-cost, moderate efficiency photovoltaics, the long-term future of photovoltaics, sometimes called the ‘third generation,’ would combine low costs with substantially higher efficiencies [73]. Nanowire solar cells can potentially satisfy both requirements and, as a result, are emerging as one of the most promising possibilities. To date, nanowire array solar cells have reached an efficiency of 13.8% [46]. The experimentally obtained efficiencies so far are still well below the Shockley-Queisser (SQ) limit—the ultimate theoretical efficiency limit for solar cells [9]. For GaAs-based single-junction photovoltaics, the SQ limit is at 33.5% [21], and the highest efficiency obtained today is at 28.8% under 1-Sun with a thin-film design [7, 58]. Thus, there is still a lot of room for improvement, and nanowire array solar cells offer one possible approach. Since a single GaAs-based nanowire solar cell was recently reported to have an apparent solar conversion efficiency of 40% [43], there is an open question as to whether performance at this level could also extend to large-area arrays.

Nanowire-based solar cells certainly have some distinct advantages over the more traditional, planar solar cell designs. For example, nanowires display excellent light absorption with minimal reflection [11, 41]. In an array configuration, the wire diameter, spacing, and even shape can be optimized, and an effective broadband sunlight absorption as high as ~98% can be achieved [42]. In single standing nanowires with diameters comparable or less than the wavelength of incoming light, the effective light capture cross section can well exceed the wire's physical cross section. In other words, such nanowires can function as optical antennas and exhibit a "self-concentrating" effect [74]. This effect is primarily responsible for the high short-circuit current (J_{SC}) observed in [43]. One additional benefit is the amount of material saved. With 10 times self-concentration, nanowires ideally would require 10 times less material than thin film designs at the same absorption efficiency [75]. This potentially can drive down the material costs for manufacturing solar cells, while keeping the cell efficiency high. Another advantage is the added junction area in a radial-junction nanowire, where the p-n junction runs along the axis of the nanowire. Carriers generated inside the nanowire can be quickly collected by the junction without much diffusion [76-78], thereby improving the carrier collection efficiency.

On the other hand, nanowire solar cells also have some inherent disadvantages. One of the most obvious is their high surface-to-volume ratio. If left untreated, the nanowire surfaces can be defective with dangling bonds and as a result, induce large surface recombination. This is commonly cited as the leading cause for the low open-circuit voltages (V_{OC}) observed in fabricated nanowire solar cells [78-80]. However, this can be an advantage for certain applications such as electrochemical cells which require a high surface area-to-volume ratio. A second challenge associated with nanowires is building proper barriers for deflecting minority carriers away from contacts, such as the back-surface-field (BSF) used in silicon and GaAs thin-film solar cells [6]. Without proper minority carrier deflectors, the recombination loss at contacts can be significant. A third, lesser-known disadvantage is the decrease of reabsorption of radiated photons —a phenomenon known as photon recycling [61]. This has been shown to be a particularly important effect in high efficiency solar cells such as the GaAs double-heterostructure thin-film solar cells [7, 50, 81]. Near the SQ limit, radiative recombination becomes the dominant loss mechanism by emitting photons out of the device structure from recombined electron-hole pairs. If emitted photons can be trapped within the device and reabsorbed before escaping, they are not lost, so the radiative recombination is effectively decreased. Of course, one cannot completely eliminate the re-emission required by detailed balance. In planar solar cells, photon recycling benefits from having a backside mirror and total internal reflection, meaning only a small fraction of the isotropically emitted photons can escape the structure through the semiconductor (for GaAs, refractive index $n=3.3$ near the band edge)-air ($n=1$) interface. In comparison, nanowire solar cells are commonly designed to enhance in-coupling of light for maximum sunlight absorption, and as a result of reciprocity [82, 83], the radiatively emitted photons can also be extracted out of the device efficiently, thus decreasing the probability of reabsorption.

The design and operation of the nanowire solar cells are distinctly different, and arguably more complex than traditional solar cells. In traditional solar cells, the electrically active part of the cell, namely the p-n junction responsible for separating the carriers, is well separated from the optically active part, namely the anti-reflective coating for enhancing sunlight absorption. One can easily optimize one separately without too much concern for the other. In the nanowires however, the electrically and optically active regions are the same and one. Aspects such as photon recycling further complicate the design by linking the electrical transport with optical reabsorption. Thus, in order to properly predict the performance of nanowire solar cells, one must consider the optical and electrical aspects in a self-consistent fashion. Moreover, photon recycling is an important aspect in devices other than nanowires also, for example, in optoelectronic devices such as LED [84]. We expect that, as the solar cell efficiency increases toward its ultimate limit, the complication of photon recycling linking electrical and optical components will become an important issue that is common to all the devices.

This chapter explores practical issues of GaAs-based standing nanowire solar cell efficiency using detailed numerical simulations that include both electrical transport and optics. The first step, therefore, is to build a numerical device simulator including photon recycling in a way that is consistent with electrical transport. The details of our self-consistent electrical-optical model are discussed in Sec. 3.3. In Sec. 3.4, we first establish a baseline radial-junction nanowire structure as a starting point. We investigate both the radial and vertical junction designs in detail and compare their performance to a more traditional planar GaAs thin-film solar cell modeled after the current efficiency record at 28.8%. Our conclusions are summarized in Sec. 3.5.

3.3 Numerical methods

As discussed in Sec. 3.2, to properly model a nanowire solar cell, the electrical and optical aspects need to be considered in a self-consistent manner. The key physical phenomena included in our model are as follows:

- *Sunlight absorption (optics module)*: The absorption from sunlight must be properly modeled in 3D using wave optics solving Maxwell's equations.
- *Electrical transport (electrical module)*: The electron and hole transport equations coupled with Poisson's equation must be solved self-consistently in a 3D nanowire geometry. Due to the symmetry of the nanowire however, the equations can be solved in cylindrical coordinates.
- *Spontaneous emission (optics module)*: The spontaneous emission rate inside a nanowire can be very different from one under a homogenous environment [85]. Maxwell's equations need to be solved in 3D to resolve this spontaneous emission modification due to the nanowire geometry.
- *Photon recycling (optics module)*: The emission from the intrinsic radiative recombination has a finite probability to be reabsorbed, and this spatially-resolved absorption rate can be obtained, along with the spontaneous emission modification factor, by monitoring the divergence of the Poynting vector in the dispersive semiconductor material.

Below, we consider the implementation of both the optics and electrical modules, before moving on to our approach to integrating them together.

3.3.1 Optics module

For optical simulation in 3D nanowires, we employ a finite-difference time-domain (FDTD) simulation [86] implemented via a freely available software package developed at MIT, known as MEEP [87]. We have developed an optics module based on MEEP that delivers three quantities in matrix form: the sunlight absorption matrix, the spontaneous emission matrix, and the photon recycling matrix.

For the sunlight absorption matrix, the standard AM1.5G solar spectrum is used. The spectrum is first divided into 100 wavelength ranges, with each segment having 1/100 of the total sunlight flux. The average wavelength for each segment is used to characterize that particular segment. For each segment, one FDTD simulation is then done by injecting continuous-wave (CW), half TE and half TM, perpendicularly incident radiation onto the standing nanowire structure. To capture material dispersion, the GaAs is modeled with a complex dielectric constant that depends on wavelength [88]. The absorption rate at each position can be obtained with the following formula [86]

$$P_{abs} = -0.5\omega|E|^2\, imag(\epsilon)\,, \tag{3.1}$$

where ω is the angular frequency, E is the complex electric field, and $imag(\epsilon)$ is the imaginary part of the dielectric constant associated with loss. The absorption rate is then weighted by the AM1.5G solar spectrum and summed over all the wavelengths.

For the spontaneous emission matrix and the photon recycling matrix, a dipole source is placed inside nanowire for the calculation. Virtual flux planes surrounding the nanowire, plus the integrated absorption within the nanowire, yield the total emission of the dipole. The same simulation is then done in a homogenous environment with the semiconductor material occupying the entire simulation space. The ratio between the amounts of the two emissions is the spontaneous emission modification factor inside a nanowire. The spatially resolved absorption inside the nanowire also gives us the photon recycling profile for radiative emission at that particular location. This photon-recycling rate is normalized to quantify, for one unit of emission at one position, what percentage (in units of /cm^{3}s) is reabsorbed at every other position. Of course, these simulations must be done at all the locations within the nanowire and for all dipole orientations (since no preferred direction is assumed). For each dipole orientation, the photon-recycling and emission enhancement profile throughout the nanowire does not have continuous rotational symmetry. For this reason, the optical module, unlike the electrical module to be discussed next, must be done in 3D instead of in cylindrical coordinate.

3.3.2 Electrical module

For electrical simulations of nanowires, we use Sentaurus™ from Synopsys [89] which solves the semiconductor transport equations coupled with Poisson's equation self-consistently in 1D, 2D, and 3D [90]. For this study, we exploit the fact that electrical transport in nanowires has continuous rotational symmetry about the wire center, and use cylindrical coordinates to reduce computational time. Various recombination mechanisms are considered in this study, including the bulk SRH, surface, Auger, and radiative recombinations. Important material parameters are listed below, where a baseline nanowire structure is established.

Radiative recombination is an intrinsic property of any piece of material at a finite temperature, and in a homogeneous environment, it is related to the absorption coefficient by the Roosbroeck-Shockley equation [52],

$$R_{emit}(V=0)=\int R_{emit}(v)dv=\int \frac{8\pi v^2 n^2}{c^2}\frac{\alpha(v)}{e^{(hv/kT)}-1}dv \tag{3.2}$$

where $\alpha(v)$ is the optical absorption coefficient at wavelength v, n is the index of refraction, T is the material temperature, and h, c, and k are standard physical constants. The condition where the applied voltage V=0 indicates this equation applies at equilibrium. Away from equilibrium, the quasi-Fermi levels for electrons and holes split, so that:

$$R_{emit}(V)=R_{emit}(V=0)e^{qV/kT}\,. \tag{3.3}$$

The spatially resolved spontaneous emission modification factor, calculated from the optics module, is then used to scale this intrinsic radiative recombination rate. Subsequently, the photon recycling matrix is used to calculate the reabsorption, and this introduces a new generation term into the continuity equation for electrical transport calculations in Sentaurus™.

3.3.3 Electro-optically coupled simulator

The overall flow of the electro-optically coupled simulator is shown in Fig. 3.1. Sentaurus conveniently offers Physical Model Interfaces (PMI) to allow seamlessly integration with the optical module. The optical module is parallelized. An entire simulation for one standing nanowire with ~ 400 nm in diameter and ~ 2 mm in length takes approximately 5 hours with 100 cores (64-bit, dual 12-core AMD Opteron 6172). A similar electro-optically coupled approach based on ray-tracing optics and 1D transport has been successfully used in the past to investigate GaAs solar cells approaching the SQ limit [56, 67].

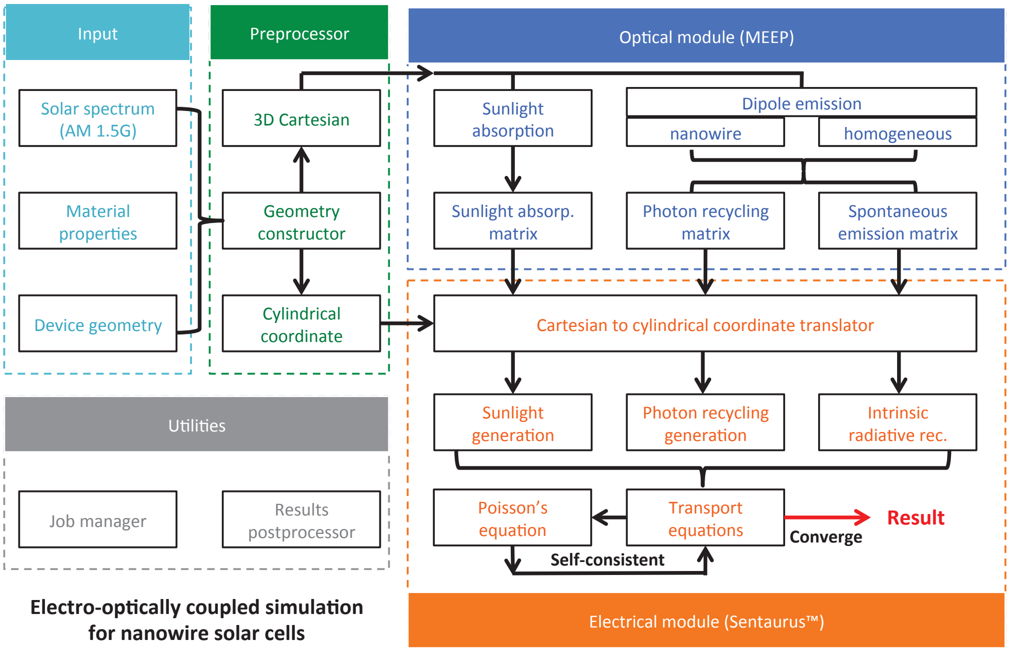

Fig. 3.1. Electro-optically coupled simulation framework flowchart, suitable for incorporating photon recycling effects into a PV device simulation in a self-consistent fashion.

3.4 Results and discussion

3.4.1 Baseline parameters and performance

To compare various designs and parameters, a baseline nanowire solar cell is modeled after [43]. The device structure is shown in Fig. 3.2(a). The single standing nanowire is GaAs-based with a radial junction. It is 212.5 nm in radius and 2.5 mm in height. It stands on a p-type doped silicon substrate. At its center is a $7x10^{18}$ /cm^3 p-type doped GaAs core with 147.5 nm radius. An intrinsic GaAs layer of 15 nm radial thickness is sandwiched between the p-type core and a $7x10^{18}$ /cm^3 n-type doped GaAs shell. The heavily doped p-type substrate is assumed to make an ideal Ohmic contact with the p-type GaAs core, and the n-type contact is only in contact with the top of the nanowire and is transparent. These are of course very ideal assumptions, but doing so allows us to independently control the surface recombination velocities on the side. We concern only the intrinsic losses of the solar cell design (surface and bulk SRH, Auger, radiative recombinations, etc.). We do not take extrinsic factors into account (shadowing, series resistance, front reflection, reliability, grid design, etc.). The temperature is set to 300 K. In this work, we focus on this specific nanowire geometry and compare its radial and vertical junction configurations with thin-film design. The optimization of such solar cells and the performance in array settings will be investigated in a later study. In addition, although, as pointed out in [43], the structure is not optimized for maximum efficiency, it provides us a realistic platform to start our numerical study. Although the performance may differ with different device dimension or material parameters, the detailed physics of the device operation and observations made thereof remain the same.

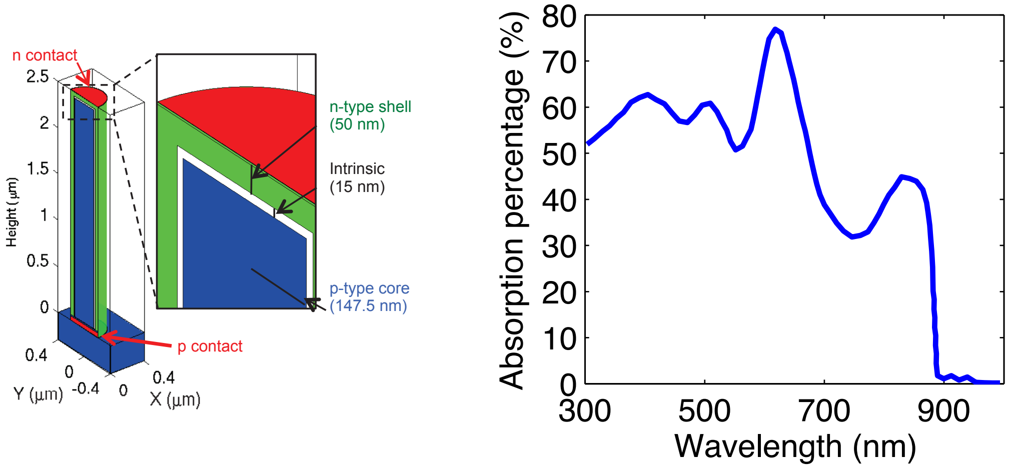

Fig. 3.2. (a) Baseline single nanowire solar cell geometry with a radial junction; (b) Absorptivity vs. incident wavelength for the baseline single nanowire solar cell.

Table 3.1. Key baseline material parameters

	Electron	**Hole**
Mobility	2500 $cm^2/V\cdot s$	60 $cm^2/V\cdot s$
SRH lifetime	1 ms	1 ms
Auger coefficient	$7x10^{-30}$ cm^6/s	$7x10^{-30}$ cm^6/s
Effective density of states	$4.7x10^{17}$ $/cm^3$	$9x10^{18}$ $/cm^3$
Recombination velocity at contacts	10^7 cm/s	10^7 cm/s
Surface recombination velocity	10^7 cm/s	10^7 cm/s

[a] unless mentioned specifically, all simulations in this study use the parameters in this table by default.

The absorption percentage of perpendicularly incident CW light is plotted in Fig. 3.2(b). The absorptivity exhibits several peaks as the incident wavelength becomes comparable or exceeds the nanowire's physical diameter. The complete result for different diameters can be found in [43]. Overall, the broadband absorptivity for a single standing nanowire is much less than what one can achieve in an array of nanowires and in thin-films with multiple layers of anti-reflection coatings [91, 92].

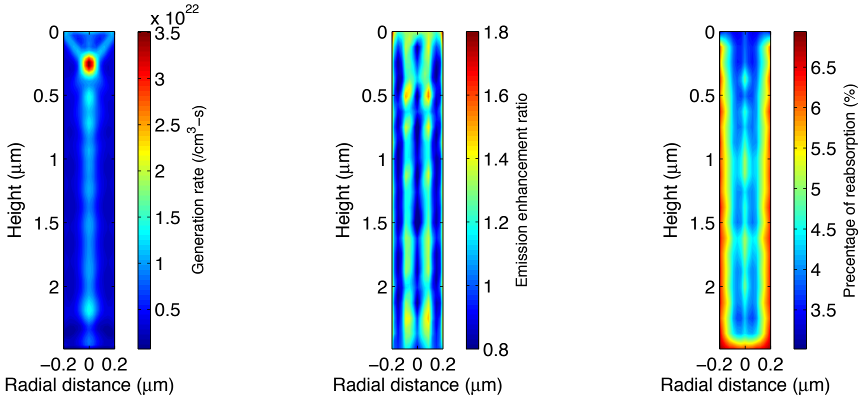

Fig. 3.3. Three important quantities are spatially resolved with wave optics simulation: (a) Carrier generation rate under AM1.5G. (b) Spontaneous emission enhancement with respect to a homogeneous environment. (c) Spatially resolved photon recycling probability.

Fig. 3.3 shows the three important optical matrices generated by the wave optics module. Fig. 3.3(a) shows the spatially resolved generation rate from AM1.5G sunlight spectrum. The generation focuses strongly at the center of the nanowire and away from the surfaces. This is beneficial, since a defective surface may rapidly recombine electron-hole pairs generated near its vicinity. Fig. 3.3(b) shows the spatially resolved spontaneous emission modification factor. The overall modification to the spontaneous emission is not very significant for this particular nanowire. The result also shows invariance along the nanowire length. This is due to the fact that the aspect ratio of the wire is large, so it can be approximated as a wire with infinite length. The solution is not expected to vary along the length in an infinite wire. Fig. 3.3(c) shows the spatially resolved percentage of reabsorption. It is interpreted as the percentage of photon emission reabsorbed by the nanowire, after averaging over x, y, and z dipole orientations. The average photon recycling probability is only around ~5% for this particular nanowire structure. This is in stark contrast with a well-designed thin-film solar cell, where more than 80% of the emission can be recycled [7, 58, 93] – more than an order of magnitude higher. This small photon recycling in nanowires is the consequence of having improved light coupling, which enhances the emission by reciprocity. For this reason, photon recycling in single GaAs nanowire photovoltaic is low and may even be disregarded without introducing much error. On the other hand, photo recycling in planar GaAs solar cells can be significant and shall not be disregarded. In general, to know the significance of photon recycling and emission enhancement for a novel nanostructure, it is important to conduct a full electro-optically coupled simulation as we have demonstrated in this work.

This suppression of photon recycling due to enhanced out-coupling is an inherent disadvantage for nanowire solar cells. As suggested in [50], at open-circuit, the external luminescence efficiency should be as close to 100% as possible. For every photon absorbed from the incident spectrum, one should be "extracted" from the device. But to maximize open-circuit voltage, the quasi-Fermi level spitting must be maximized. This means that Δn should be as large as possible. The internal recombination rate, $\Delta n/\tau$, must equal the rate at which photons are absorbed from the incident illumination, G_{OP}. To maximize Δn, the carrier lifetime should be as long as possible. Non-radiative processes must be minimized so that the lifetime is dictated by photons emitted by radiative recombination that leave the cell. To make the lifetime as long as possible, we should make it **difficult** to extract the emitted photons using, for example, a planar thin-film solar cell with good backside mirror as illustrated in Fig. 3(b) of [21]. So there are two ways to achieve 100% luminescence efficiency: 1) extract the emitted photons quickly, but this results in low lifetime, low Δn, and low open-circuit voltage, or 2) make it hard for emitted photons to escape, which results in high lifetime, high Δn, and higher open-circuit voltage. Both approaches give 100% external luminescence efficiency, but the second is preferable for solar cells. To make the lifetime as long as possible, one should trap the photons emitted by radiative recombination inside the cell for as long as possible.

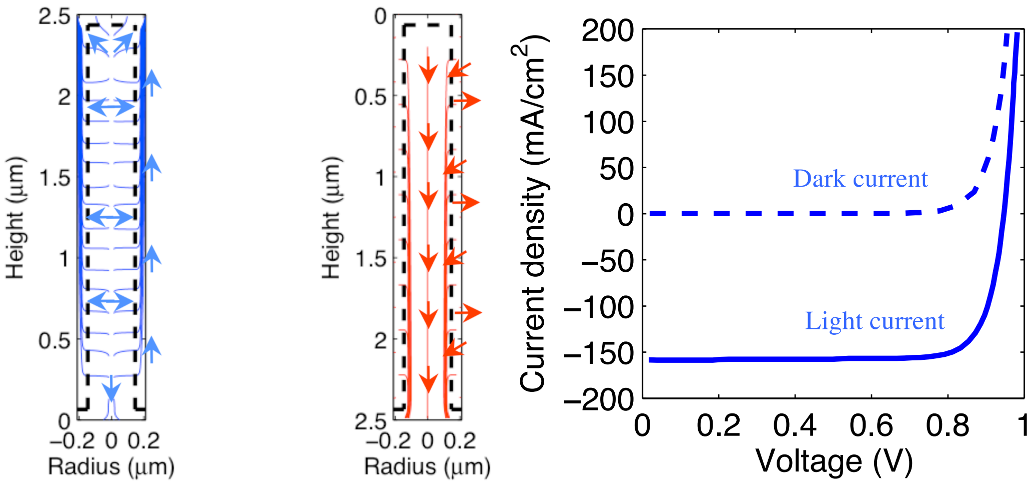

Fig. 3.4. With radial junction, (a) Electron current flow streamline at J_{SC}. (b) Hole current flow streamline at J_{SC}. (c) Benchmark single nanowire solar cell light and dark IV.

Once the electron-hole pairs are generated, each carrier will be set to motion in accordance with the transport equations and Poisson's equation. Fig. 3.4(a) shows the flow of electrons inside the nanowire at J_{SC}. The core region is p-type, so the electrons generated in the core need to travel to the n contact at the top of the nanowire to be collected. As seen in Fig. 3.4(a), the radial junction is very effective in collecting the electrons. Electrons quickly travel radially to the nearest p-n junction and flows along the n-type shell toward the n contact at the top. Some of the electrons generated at the bottom of the nanowire recombined at the p contact. Fig. 3.4(b) shows the flow of holes inside the nanowire at J_{SC}. Some of the holes generated inside the n-type shell are collected by the p-n junction, but the rest recombine at the surface (arrows pointing outward).

However, since the generation of the carriers focuses away from the surface (Fig. 3.3(a)), the loss due to surface recombination is significantly reduced.

The light and dark IVs are shown in Fig. 3.4(c). The IVs shows typical solar cell behavior obeying the superposition principle [94]. Despite the poor absorptivity shown in Fig. 3.2(b), the optical antenna effect concentrates the light outside the physical cross-section of the nanowire and boosts its overall absorption. The total generation within the nanowire divided by its physical area is at 260 mA/cm^2. Due to recombination losses, primarily surface recombination and emission, the J_{SC} is reduced to 160 mA/cm^2. This J_{SC} is comparable to the experimentally reported value at 180 mA/cm^2 in [43]. On the other hand, the predicted V_{OC} is at 0.94 V, comparing to the experimentally reported value at 0.43 V. This large discrepancy is possibly due to defects such as shunts or series resistance. The simulation thus suggests the low V_{OC} observed is <u>not</u> fundamental to nanowire solar cells, and there is a lot of room for improvement through material and design optimization.

3.4.2 Nanowire solar cell with radial junction

We take a closer look at the role of surface recombination and electrical contacts in the nanowire solar cell with radial junction. Fig. 3.5(a) shows the J_{SC} and V_{OC} under various surface recombination velocities. Any surface recombination velocity lower than 10^4 cm/s has minimal effect on the cell performance, while anything higher will lower both the J_{SC} and V_{OC}. The result suggests that, by treating the surfaces and removing dangling bonds, the single nanowire reported in [43] may obtain an extra J_{SC} of ~ 25 mA/cm^2. The major loss mechanisms at V_{OC} are shown in Fig. 3.5(b). Surprisingly, recombination at contacts can be significant when the surface recombination is not dominating. The contact recombination primarily comes from the diffusion of electrons generated inside the p-type core toward the back p-type contact. Such contact recombination can significantly degrade the performance of solar cells. A heavily doped back-surface-field (BSF) in silicon or a heterojunction in GaAs thin-film solar cells is commonly used to deflect minority carriers away in order to minimize the contact recombination loss [95]. These types of structures however could be a significant challenge to implement experimentally in nanowire solar cells.

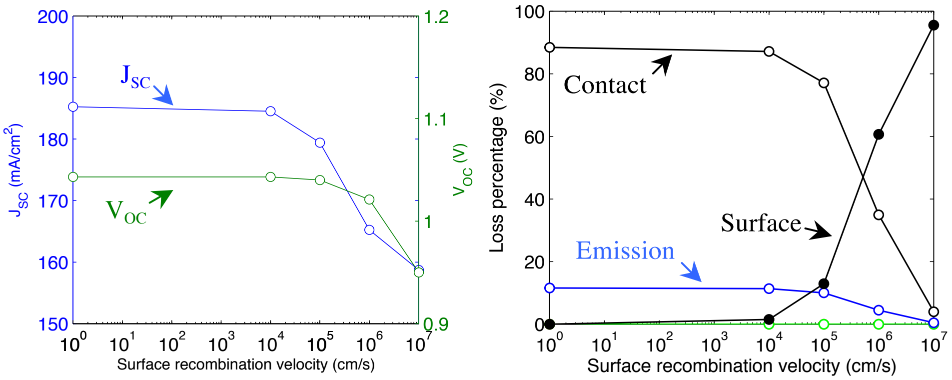

Fig. 3.5. With no minority carrier deflections at both contacts, performances for various surface recombination velocities are displayed. (a) J_{SC} and V_{OC}. (b) Percentage of each major loss mechanism at V_{OC}.

Fig. 3.6(a) shows the solar cell performance under various surface recombination velocities assuming no contact recombination. An extra ~5 mA/cm^2 in J_{SC} and ~100 mV in V_{OC} could be obtained through improved minority carrier deflection at both contacts. When both the surface and contact recombination are low, the radiative recombination, labeled as "emission" in Fig. 3.6(b), becomes the dominant loss mechanism. The radiative recombination thus caps J_{SC} and V_{OC} at approximately 190 mA/cm^2 and 1.1 V respectively.

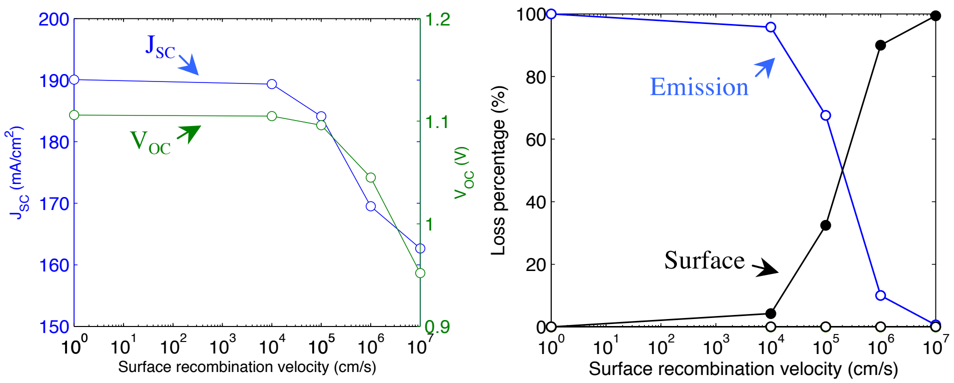

Fig. 3.6. With complete minority carrier deflection at both contacts, performances for various surface recombination velocities are displayed. (a) J_{SC} and V_{OC}. (b) Percentage of each major loss mechanism at V_{OC}.

3.4.3 Nanowire solar cell with vertical junction

In this section, we investigate an alternative design for the nanowire solar cell. In the vertical junction configuration, the p-i-n regions are stacked vertically along the nanowire height. The resulting geometry, as shown in Fig. 3.7(a), is effectively the radial junction structure with the side junction removed and everything else kept the same. The top vertical junction in fact exists in the radial junction structure, but it is not primarily responsible for the separation of charges—the side junction does this job and collects majority of the current. Now in the vertical junction configuration, with the side junction removed, the only place carriers can be separated is at the very top of the wire.

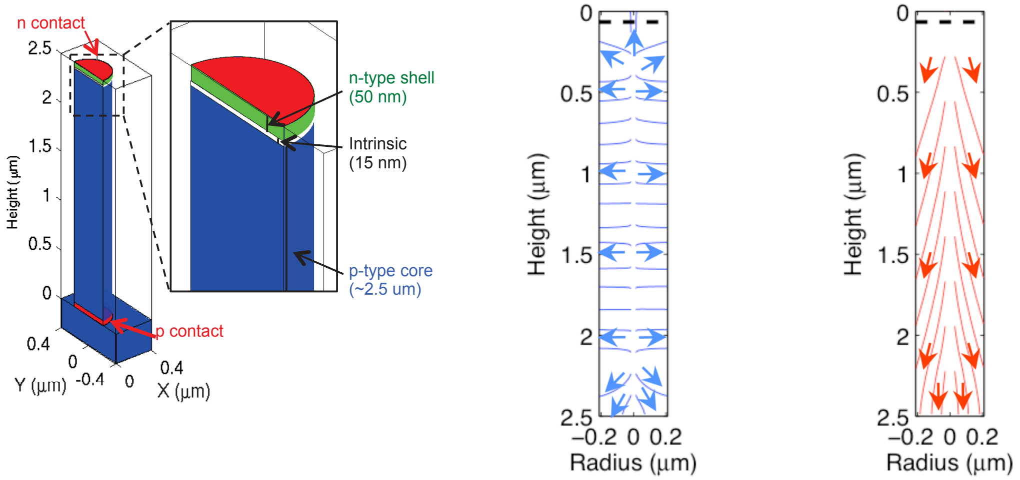

Fig. 3.7. With vertical junction, (a) Device geometry. (b) Electron current flow streamline at J_{SC}. (c) Hole current flow streamline at J_{SC}.

Fig. 3.7(b) shows the electron current flow within the nanowire. Without the radial junction isolating the surfaces, the electrons generated in the p-type region quickly flow to the surface and recombine. Only a small fraction of the electrons that are generated near the vicinity of the depletion region at the top of the nanowire are collected. The surface recombination is so high that, as seen in Fig. 3.7(c), the hole current is significantly distorted as a result. Therefore, intuitively, one would expect the vertical junction is much more vulnerable to defective surfaces and, therefore, performs worse than the radial junction.

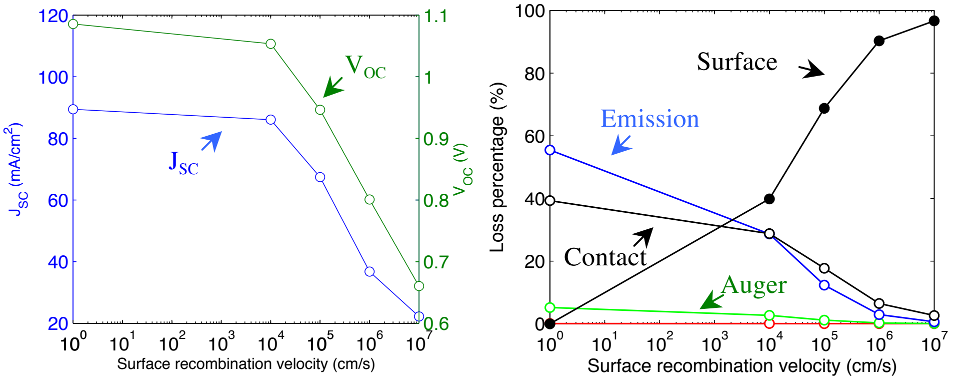

Fig. 3.8. With no minority carrier deflections at both contacts, performances for various surface recombination velocities are displayed. (a) J_{SC} and V_{OC}. (b) Percentage of each major loss mechanism at V_{OC}.

Fig. 3.8(a) confirms the vertical junction's vulnerability to surface recombination. Overall, the J_{SC} and V_{OC} values are significantly lower than those for radial junctions. If the surfaces are left untreated, the J_{SC} can plummet to as low as 20 mA/cm^2, which is 1/13 of the total absorption. The V_{OC} can be significantly reduced as well. In this situation, materials having low surface recombination when left untreated, such as InP, become preferable to GaAs.

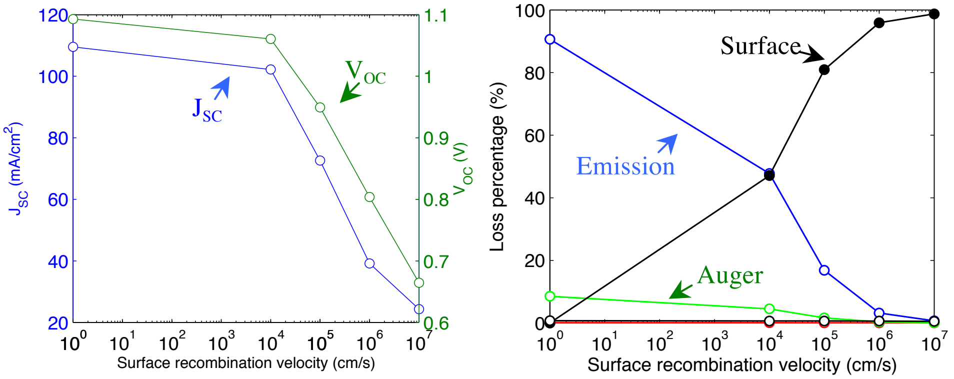

Fig. 3.9. With complete minority carrier deflections at both contacts, performances for various surface recombination velocities are displayed. (a) J_{SC} and V_{OC}. (b) Percentage of each major loss mechanism at V_{OC}.

Since contact recombination in the vertical junction is not the most dominant recombination at V_{OC}, one expects little effect on V_{OC} when the contacts are improved to deflect minority carriers. On the other hand, the J_{SC} can be improved to gain ~20 mA/cm^2, suggesting significant electron diffusion toward the back contact. The J_{SC} in the best case is significantly lower than the one in the radial junction, due to the inefficient collection of carriers causing carriers to be lost through radiative emission. Over all, the vertical junction displays an inferior performance compared with the radial junction due to its vulnerability to surface defects and inefficient carrier collection.

3.4.4 Planar thin-film solar cell

High efficiency single-junction solar cells using GaAs have been created using a thin-film approach, with efficiencies as high as 28.8% under the standard solar spectrum being reported [93]. This efficiency is fairly close to the theoretically predicted SQ efficiency limit at 33%. The planar thin-film solar cell is less complex than a nanowire cell, and many theoretical studies have been done to investigate its physics. A more detailed design study of GaAs thin-film solar cells toward the SQ limit can be found in [93]. In this work, we only briefly look at the role of the backside mirror reflectivity to illustrate the major differences between nanowire and thin-film solar cells.

Fig. 3.10(a) shows the thin-film solar cell geometry. It is equivalent to the vertical junction nanowire extended to have an infinite radius. The structure has two distinct features that nanowire cells do not have. One is the front and back AlGaAs/GaAs heterojunction interface blocking the minority carriers away from the contacts. This is a commonly deployed feature in thin-film cells, and therefore, we assume there is no minority carrier loss at the contacts. The other distinct feature is the backside mirror, which reflects the radiatively emitted photons back to the thin-film and enhances photon recycling. This effect has been known and proposed as a means to increase GaAs solar cell efficiency, going back to early work from over two decades ago [48].

In order to make a fair comparison with the nanowire geometry, the total generation rate in the planar cell is kept the same as that in nanowires. This translates to a 7.7-Sun concentration that produces a generation current of 260 mA/cm^2.

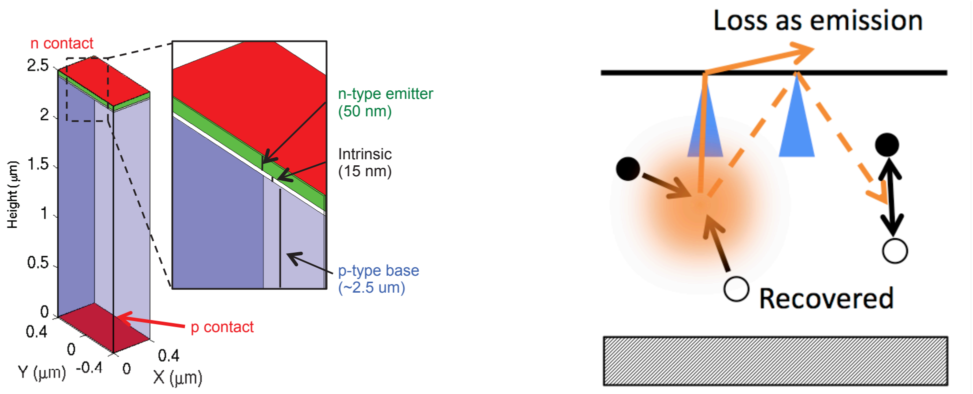

Fig. 3.10. (a) Thin-film solar cell geometry. (b) Illustration of photon recycling and emission inside a thin-film solar cell.

With the absence of surface and contact recombination, which are the two major sources of non-radiative recombinations in nanowires, the radiative recombination loss dominates in thin-film GaAs solar cells. This is an expected signature of any solar cell approaching its SQ limit, as non-radiative recombination losses are being minimized. The radiatively emitted photons, if not recycled, may be emitted out of the structure or be parasitically absorbed by the backside mirror. This is illustrated in Fig. 3.10(b). The planar semiconductor/air interface creates a small escape cone, allowing only ~2% of the emission escapes the structure. The rest of the emitted photons are trapped within the thin-film through total internal reflection, until they are reabsorbed by the semiconductor or parasitically absorbed by the mirror and turned into waste heat. The emitted photons concentrate closely to the bandgap energy, where the absorption probability is low for such photons. The photons thus need to bounce around the thin-film and travel an extended distance for recycling. A fraction of the photons striking the backside mirror are lost due to the imperfect reflectivity. Thus, as shown in Fig. 3.11, the mirror reflectivity noticeably influences both the J_{SC} and V_{OC}. Unless it is designed to have a high reflectivity (> 90%), the mirror is responsible for majority of the radiative recombination loss and thus is the bottleneck toward higher efficiency.

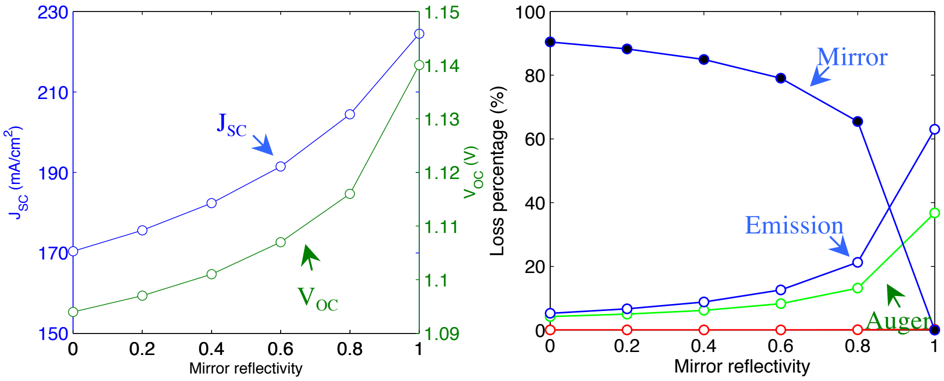

Fig. 3.11. With bulk SRH lifetime at 1 us, performances for various backside mirror reflectivities are displayed. (a) J_{SC} and V_{OC}. (b) Percentage of each major loss mechanism at V_{OC}.

3.4.5 Summary

Table 2 summarizes the best performing radial and vertical junction nanowire solar cells and planar solar cell seen in this study. Also listed are experimentally reported record efficiency III-V solar cells. Due to the self-concentration effect, nanowires display an abnormally high apparent (uncorrected) efficiency exceeding 100%. We term this efficiency the “apparent efficiency” (Apparent η). Since this measure does not account for a mismatch between the optical collection area and geometric cross-sectional area, the simulated J_{SC} should be divided the self-concentration factor in order to calculate the effective efficiency (η). This effective efficiency is what would be observed after masking the optical input cross-sectional area to equal the geometric cross-sectional area; it is most suitable for comparison with other photovoltaic technologies. Note that the V_{OC} and Fill Factor (FF) are both assumed to stay invariant with concentration, since the concentration affects them only logarithmically, much less than J_{SC}.

Table 3.2. Performance comparison for various III-V single-junction solar cell types under 1-Sun, where shaded rows are numerical predictions in this study.

	Source	J_{SC} (mA/cm^2)	V_{OC} (V)	FF	Apparent η*	**η**
Radial junction single nanowire	[7]	180	0.43	0.52	40 %	**5.2 %**
	This work	190	1.1	0.84	175.6 %	**25.1 %**
Vertical junction single nanowire	This work	110	1.08	0.85	101 %	**14.4 %**
Nanowire array -vertical junction	[2]	24.6	0.779	0.724	-	**13.8 %**
Planar bulk	[5]	29.8	1.030	0.86	-	**26.4 %**
Planar thin-film	[5]	29.68	1.122	0.865	-	**28.8 %**
	This work (7.7-Sun)	225	1.14	0.87	223.2 %	**31.9 %**
SQ limit	[3]	33.5	1.12	0.89	-	**33.5%**

* Apparent efficiency does not account for a mismatch in the collection area and geometric cross-sectional for nanowires exhibiting self-focusing effects, and thus is not a ‘true’ efficiency measure.

The reported single, radial junction, nanowire solar cell in [43] shows an efficiency at 5.2%, while the theoretically predicted performance may reach as high as 25.1%. This suggests that there is still a lot of room for improvement. In comparison, the vertical junction performs much worse with a theoretically predicted best efficiency at 14.4%. Interestingly, one of the highest efficiency nanowire array solar cells is made from vertical junction with InP at 13.8% efficiency [46]. As discussed in Sec. 3.3, one of the key disadvantages of vertical junctions is the lack of depletion region area to efficiently collect the carriers. Compared to the vertical junction structure we used in this study, the InP nanowire array has a much more optimal design. The intrinsic region extends throughout the majority of the wire length, creating a built-in electric field that separates the charges efficiently.

The fabricated planar bulk and thin-film solar cells, at 26.4% and 28.8% respectively, significantly outperforms the nanowire solar cells. As discussed in Sec. 3.4, having no side surfaces and using double-heterojunction structures are two of the key advantages that planar cells have over nanowire solar cells. The thin-film solar cell has an additional advantage in having a backside mirror to enhance photon recycling. The predicted best thin-film solar cell efficiency is at 31.9%. In comparison, the SQ limit is at 33.5%. The intriguing fact that the planar solar cell can exceed the V_{OC} of the SQ limit has been explained in detail in [21] and [93].

3.5 Summary

In this study, we used an electro-optically coupled simulator to investigate the performance of GaAs-based single NW solar cell with radial and vertical junctions, based on the experimental structure explored in [43]. The thin-film GaAs solar cell is used as a comparison to illustrate some of the important differences between NW and thin-film designs. Through an extensive set of numerical simulations, we showed that the low V_{OC} observed experimentally for the NW cell at 0.43 V is not a fundamental limit; there is a lot of room for improvement to obtain higher efficiency in such cells. At V_{OC}, contact recombination becomes a major loss factor in radial junction design, while the vertical junction is much more vulnerable to surface defects. If both engineering challenges are addressed, NW solar cells can obtain high efficiencies comparable, but still lower, to that of thin-film solar cells. The distinct advantage of total internal reflection and backside mirror allows thin-films to exhibit better photon recycling. Single nanowires, on the other hand, have strong in-coupling and out-coupling of light, which creates the possibility of optical self-focusing, but also decreases photon recycling. Although the apparent efficiency can exceed 33%, this effect is caused by optical self-focusing. Thus, we found it is necessary to correct raw short-circuit currents observed by effectively masking the light entering to match the geometric cross-section of the nanowire. With this correction, near the SQ limit where radiative recombination dominates, nanowires demonstrate lower V_{OC} and J_{SC} values and efficiencies than a thin-film solar cell. Although the design principles differ, both the nanowire and thin-film solar cells are constrained by the same physical principles and neither should be expected to exceed the SQ limit.

4 DESIGN OF GAINP/GAAS TANDEM SOLAR CELLS TOWARD THE SHOCKLEY-QUEISSER LIMIT

4.1 Preface

The contents of this chapter have been extracted from the following publications with permission: X. Wang, M. Lundstrom, and P. Bermel, "Design of GaInP/GaAs tandem solar cells toward the Shockley-Queisser limit," *Progress in Photovoltaics,* submitted, 2014.

4.2 Introduction

The development of tandem solar cells has progressed rapidly in recent years. With a structure consisting of a GaInP top cell stacked on top of a GaAs bottom cell, NREL researchers have demonstrated a two-terminal, current-matching tandem solar cell with conversion efficiency of (31.1 ± 0.9)% under the AM1.5 global spectrum at 1000 W/m^2 [96]. While this conversion efficiency is impressively high, it still falls significantly short from the cell's ultimate, theoretical efficiency at approximately 39% [97-99].

One obvious cause for the efficiency gap is the additional complexity of the system by having two stacked, serially connected cells [100, 101]. Not only does the quality of each cell need to be controlled to minimize the recombination losses, but also the thicknesses of each layer must be optimized to achieve optimal current-matching. In addition, there are design issues including the peak tunneling current that the tunnel junction can carry, the series resistance, and the layer lattice matching [102, 103]. The current throughout the subcells for two terminal devices also has to match, since they are connected in series. This is a critical design factor for tandem solar cells, since the mismatched current will be consumed by recombination inside the non-current limiting subcell [104].

For a high efficiency cell operating close to its SQ limit [9], one additional design factor becomes critical—the internal optics for emitted photons by radiative recombination [21, 48, 50]. The emitted photons travel inside the cell structure, bouncing at the interfaces, and are eventually either reabsorbed or escape the structure. In a tandem cell, radiative recombination can be a complicated process. For example, a photon emitted from the top cell can follow several possible scenarios: 1) it can be reabsorbed in the top cell itself, fully recovering the energy by transferring it to a free electron-hole pair; 2) it can be reabsorbed at the bottom cell losing part of that energy (equal to the bandgap difference between the top and bottom cell) to the lattice through thermalization; 3) it can be lost either through parasitic absorption by the backside mirror or escape from the structure. The optical internal couplings, or the so-called luminescence couplings, between the layers are thus highly non-trivial [105, 106].

Radiative recombination, and the resulting luminescence coupling, is believed to be quite significant in the record 31.1% GaInP/GaAs solar cell [105]. GaInP and GaAs have each demonstrated high conversion efficiency in single-junction solar cell devices—20.8% [107] and 28.8% [12] respectively. Experimentally, the internal radiative efficiency (IRE) is reported to be as high as 86% in GaInP [107] and well over 99% in GaAs [108]. The IRE is a gauge for the intrinsic quality of the material and defined as

$$IRE = \frac{R'_{rad}}{R'_{rad} + R_{nr}} \tag{4.1}$$

where R'_{rad} is the intrinsic radiative recombination rate, and R_{nr} is the total non-radiative recombination rate. In other words, higher IRE, which closely related to a higher External Radiative Efficiency (ERE), is desired for operation close to the SQ limit [109].

In the literature, studies regarding the luminescence coupling focus mostly on two issues—its influence on the current matching and the loss of energy when photon emission couples to a lower bandgap cell. Therefore, the amount of absorption inside each subcell must be carefully optimized. With luminescence coupling among the subcells, the overall current matching process becomes a complex issue. Moreover, the amount of luminescence coupling can be bias dependent and nonlinear [110]. Another concern regarding the luminescence coupling is the thermalization loss when a higher energy photon is coupled to a lower bandgap subcell. This “luminescence down-coupling” decreases the maximum efficiency a cell system can achieve. Designs including using intermediate photonic layers to deflect photons away from lower bandgap subcells have recently been proposed [111]. Using spectral splitting to direct photons into independent subcells can also avoid this problem [35, 38, 112].

The design and optimization of tandem cells will thus depend on proper treatment on the electrical aspect, the optical aspect, and the coupled nature of both. Therefore, a unified, comprehensive simulation framework that can accommodate all these aspects is needed. In this chapter, we use an electro-optically coupled simulation to capture the essential physics in a self-consistent manner as discussed in detail in Sec. 4.3. We first show benchmark results for a single-junction GaAs cell and a GaAs/GaAs tunneling junction in Sec. 4.4, which establishes a good calibration of the simulator with experiments. In Sec. 4.5, we move on to analyze the roles of several critical design parameters in the GaInP/GaAs tandem solar cells based on published structures. Our conclusions are summarized in Sec. 4.6.

4.3 Approach

Since radiative recombination is the dominant loss mechanism in a high efficiency GaInP/GaAs tandem cell, it is important to model it correctly. Traditionally, the radiative recombination has been introduced using an effective radiative recombination coefficient denoted as B. Using this B coefficient, the overall radiative recombination rate can be described as

$$R_{rad} = B(np - n^2_i) \tag{4.2}$$

where n and p are the electron and hole concentrations respectively, and n_i is the intrinsic carrier concentration. As discussed in Sec. 4.2, the radiatively emitted photons propagate within the structure, and some of them are eventually reabsorbed, resulting in the so-called photon-recycling effect [64]. Therefore, the use of a B coefficient is an effective way of treating photon-recycling and perimeter recombination, into account. The B coefficient is often measured on a test structure instead of the actual device, and doing so introduces additional uncertainties. Moreover, the photon-recycling probability of a radiative recombination event is spatially dependent, i.e., an emitted photon near the cell surface will have a lower probability of being reabsorbed than one deep inside. Thus, an effective *B* coefficient is only an approximation to the actual physics.

To avoid the inaccuracy and arbitrariness of using an effective *B* coefficient, we instead model the radiative recombination event directly. Radiative recombination is an intrinsic property of any material at a finite temperature, and it is related to the absorption coefficient by the Roosbroeck-Shockley equation [48, 52],

$$R_{emit}(V=0)=\int_0^\infty R_{emit}(v)dv=\int_0^\infty \frac{8\pi v^2 n^2}{c^2}\frac{\alpha(v)}{e^{hv/kT}-1}dv \tag{4.3}$$

where *α(v)* is the optical absorption coefficient at wavelength *v*, and *n* is the index of refraction. The condition *V*=0 indicates this equation is valid at equilibrium. Away from equilibrium the quasi-Fermi levels split, so that:

$$R_{emit}(V)=R_{emit}(V=0)e^{qV/kT} \tag{4.4}$$

In this approach, we first calculate a structure-independent intrinsic radiative recombination rate using the Roosbroeck-Shockley equation, and then use ray-tracing to calculate the spatial profile of radiative emission that is either recycled or lost through parasitic absorption, or escapes. The approach is similar to the one used by Durbin *et al.* [56, 67], which we have implemented on Sentaurus™, a comprehensive numerical simulator for semiconductor devices [93]. This framework has already been successfully used to investigate single-junction GaAs solar cells and nanowire solar cells [93, 113].

4.4 Calibration with Experiments

4.4.1 Single-junction GaAs Cell

A series of single-junction GaAs solar cells, resembling the one used in the 31.1% GaInP/GaAs tandem were fabricated as part of a detailed characterization analysis conducted by NREL [105]. The goal of fabricating these devices was to obtain quantitative information regarding the radiative recombination and to observe the effects of the backside mirror to the cell's performance.

In this section, we will show that our electro-optically coupled simulator is able to reproduce the results in this experiment. The overall cell structure is shown in Fig. 4.1(a). The cell consists of a GaAs p-n junction with n-type AlInP as the window layer and p-type GaInP as a back-surface field (BSF). Both the heterojunctions are known to have very low surface recombination velocities and are very effective in reflecting minority carriers. The p-type GaAs base is 2 μm thick and is sufficient to absorb more than 90% of the incoming photons above the GaAs bandgap [21]. The device sits on top of a heavily p-type doped GaAs contact layer with variable thickness from 10 nm to 3 μm.

The thickness of this GaAs contact layer affects the number of photon that can be effectively recycled. This can be understood better from the band diagram shown in Fig. 4.1(b). Emitted photons from the radiative recombination events inside the GaAs layers need to travel through the GaAs contact layer, twice, in order to reach the reflective gold mirror and return to the GaAs layers to be recycled. As a result, the thicker the GaAs contact layer is, the less likely the photon will be reabsorbed to generate useful free carriers; any reabsorption inside the GaAs contact layer is expected to be lost, since the GaInP BSF prevents the minority carrier electrons from moving into the base and getting collected.

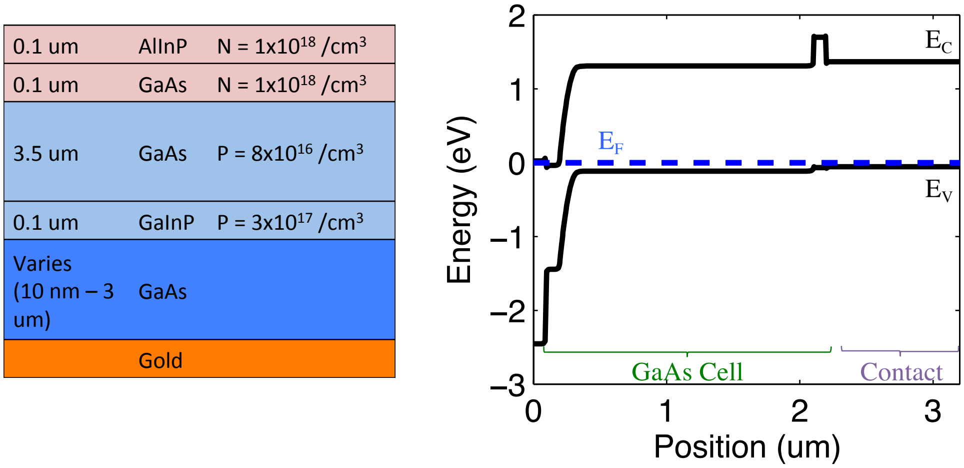

Fig. 4.1. Benchmark single-junction GaAs solar cell with variable back-contact thickness: (a) device structure, and (b) band diagram under equilibrium.

It is therefore expected that the total effective radiative recombination is proportional to the thickness of the GaAs contact layer. The results from our electro-optically coupled simulation agree with this conclusion as shown in Fig. 4.2(a). Since the radiative recombination is the dominant loss mechanism in this cell, the V_{OC} is inversely related to the amount of effective radiative recombination loss, which increases with increasing GaAs contact layer thickness. On the other hand, the J_{SC} also decreases with increasing contact thickness as shown in Fig. 4.2(b), and this is primarily due to the sunlight absorption at the GaAs contact layer.

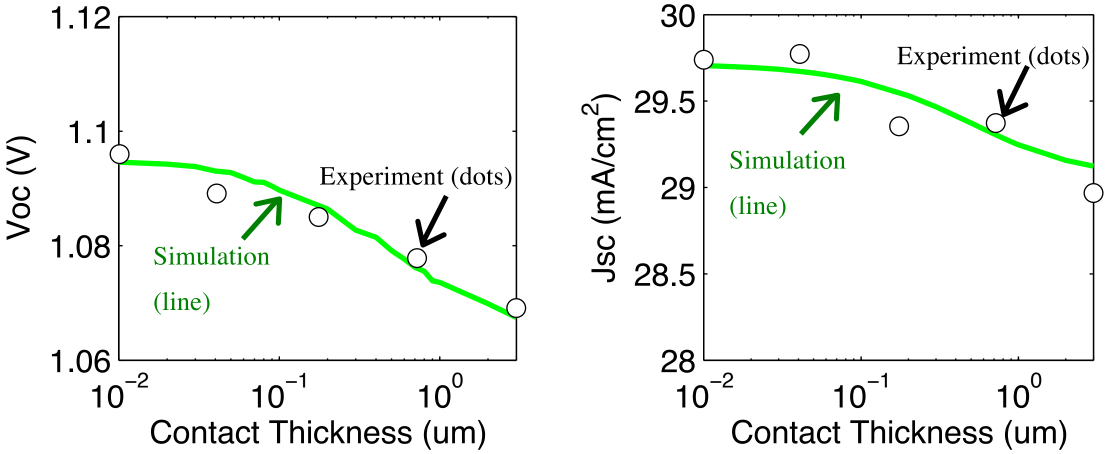

Fig. 4.2. (a) V_{OC} and (b) J_{SC} from simulation for various contact thicknesses comparing to experimentally reported value. A combined optical loss at 6% due to shadowing and reflection is assumed. Both series show a match to within 2% for all data points.

4.4.2 GaAs/GaAs Tunnel Junction

Another important aspect to calibrate is the GaAs/GaAs tunnel junction used to connect the top GaInP cell with the bottom GaAs cell in series. Both sides of the p-n junction are heavily doped, creating a non-local tunneling path between the conduction and valence bands near the Fermi level. The band diagram of the tunnel junction is shown in Fig. 4.3(a).

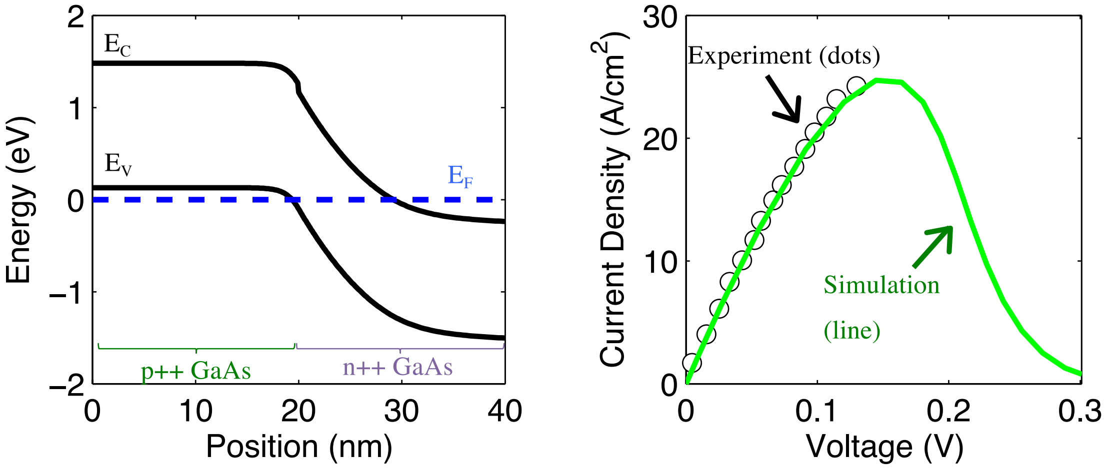

Fig. 4.3. GaAs/GaAs tunnel junction used in this study: (a) band diagram under equilibrium, and (b) numerically simulated tunneling current benchmark with experiment. Resistance under AM1.5G spectrum is predicted to be small, as is also seen experimentally.

We follow the work by Hermle [114] and Kanevce [115] on simulating the tunneling current. The model is a Sentaurus™ built-in, non-local tunneling model using the WKB approximation [116]. The model allows the holes inside the valence band of the p^{++} side to recombine, non-locally, with the electrons inside the conduction band of the n^{++} side. This semi-classical treatment of tunneling yields good agreement with experiments as seen in Fig. 4.3(b). The experimental data and structure are taken from [114]. The tunneling current rises with voltage and then drops due to the decreasing of available tunneling energy paths with increasing bias, yielding a negative differential resistance region. Eventually, the IV will rise again at higher bias due at the onset of the thermionic current. This results in the well-known “N-shape” IV characteristic of the tunnel diode.

For the purpose of this work, however, the precise benchmarking of the tunneling diode is not critical. The diode is able to carry significant amount of current under very small bias. For a AM1.5G spectrum under 1-sun concentration, the expected maximum J_{SC} of a GaInP/GaAs tandem junction is around 15 mA/cm^2, which corresponds to less than 1 mV of bias on the tunnel junction. Therefore, the main purpose of the tunnel junction in this work is to accurately capture the physics of the entire tandem cell under one simulation.

4.5 Results and discussion

4.5.1 Baseline GaInP/GaAs Tandem Solar Cell

The baseline GaInP/GaAs tandem solar cell structure used in this study is modeled on the 31.1% cell reported by NREL [105] shown in Fig. 4.4(a). Overall, the tandem cell consists of a top GaInP cell connected to a bottom GaAs cell through a GaAs/GaAs tunnel junction described in Sec. III. The top GaInP cell has GaInP p-n junction layer between an AlInP front-surface field (FSF) and an AlGaInP BSF. The GaInP layer is designed to be 0.7-um thick, which leads to optimal current matching [105]. The bottom cell consists of a 2-um thick GaAs p-n junction between a FSF with n-type doped $Al_{0.3}Ga_{0.7}As$ and a BSF with p-type doped $Al_{0.3}Ga_{0.7}As$. The GaAs bottom cell is very similar to the one by Alta Devices [7]. For parameters that are not reported with the 31.1% cell, such as the FSF and BSF thicknesses, we choose the values reported from a 29.5% GaInP/GaAs tandem cell reported by NREL [117]. The overall band diagram is shown in Fig. 4.4(b).

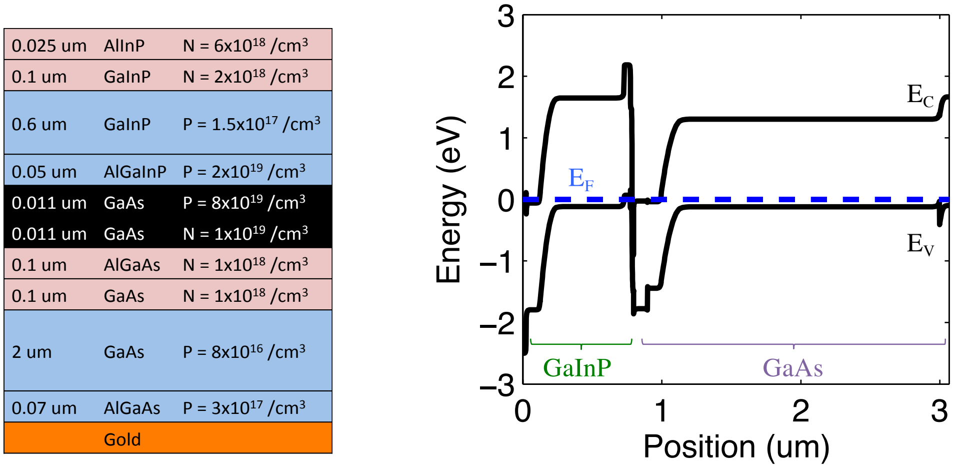

0.025 um	AlInP	N = 6×10^{18} /cm^3
0.1 um	GaInP	N = 2×10^{18} /cm^3
0.6 um	GaInP	P = 1.5×10^{17} /cm^3
0.05 um	AlGaInP	P = 2×10^{19} /cm^3
0.011 um	GaAs	P = 8×10^{19} /cm^3
0.011 um	GaAs	N = 1×10^{19} /cm^3
0.1 um	AlGaAs	N = 1×10^{18} /cm^3
0.1 um	GaAs	N = 1×10^{18} /cm^3
2 um	GaAs	P = 8×10^{16} /cm^3
0.07 um	AlGaAs	P = 3×10^{17} /cm^3
	Gold	

Fig. 4.4. GaInP/GaAs tandem solar cell modeled after the NREL 31.1% cell: (a) device structure, and (b) band diagram under equilibrium.

For the GaAs cell, material parameters are calibrated as discussed in Sec. II. The SRH lifetime is set to 2.7 μs as reported [105], with the GaAs absorption coefficient, which is used to calculate radiative recombination, is taken from Ref. [48]. For the GaInP cell, the absorption coefficient is taken from [118] and a SRH lifetime of 500 ns is used. The interface formed between the emitter (base) and FSF (BSF) is reported to have very low surface recombination velocities, so we do not include interface recombination in this study. The optical reflectance and shadowing losses are taken from [117]. The backside mirror reflectivity is set to 60% to obtain the best match with the measurements. It has small impact on the J_{SC} but, as we will discuss next, can significantly impact the V_{OC}.

With these calibrated parameters, we find a good match with the measured IV and EQE as shown in Fig. 4.5(a) and Fig. 4.5(b) respectively. The simulation shows a V_{OC} and J_{SC} of 2.52 V and 14.09 mA/cm^2 versus measured value of 2.51 V and 14.13 mA/cm^2, respectively. A series resistance of 0.8 Ω-cm^2 is added to match the measured fill factor of 87.7%. The simulated efficiency of 31.3 % is very close to the measured 31.1%. The EQE is obtained by simulating the double-source method as used in experiments [119]. In this method, the junction-under-test is illuminated using monochromatic light sources with various wavelengths. At the same time, the second junction is over-illuminated with a bias light. The bias light is chosen to have a certain wavelength range of photons that are highly absorbed only by the second junction. This double-source setup makes the junction under test into the current-limiting junction, so the output current of the tandem cell becomes proportional to the EQE of the junction under test.

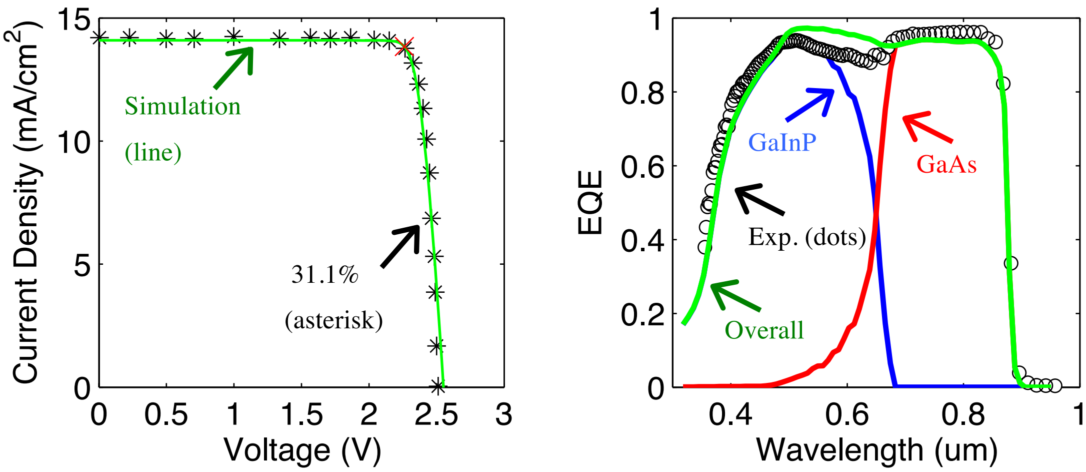

Fig. 4.5. (a) Simulated IV (green line) compared with measured NREL 31.1% cell (black asterisk), and (b) Simulated EQE from top GaInP cell (blue line) and bottom GaAs cell (red line). The two combined (green line) is compared with the measured EQE (black dots) from the NREL 31.1% cell and shows a close match.

The EQE for the GaAs cell shows an interesting phenomenon between 500 nm and 650 nm. Within this range, the incoming photons should be absorbed by the GaInP, so the EQE of GaAs bottom cell is expected to be very small. A closer look reveals the finite EQE seen within this range is due to not only the incomplete absorption by the GaInP but also the luminescence coupling from the higher energy photons emitted from the GaInP top cell. This effect can be more easily observed in the spatially resolved recombination plot shown in Fig. 4.6(a). The intrinsic *radiative* recombination is the photon emission, and the recycling of these photons creates a generation profile denoted by *recycling*. The recycling curve shows a strong peak near the bottom cell top surface, and this excess generation is due to the recycling of incoming luminescence coupling from the top GaInP cell.

While photon recycling effectively reduces the loss due to radiative recombination, this luminescence coupling has its downside. By recycling a photon where the bandgap is lower than the photon's energy, the energy from the mismatch in bandgap is lost through thermalization. Tandem cell design in the presence of luminescence coupling therefore becomes a non-trivial compromise between reducing the radiative recombination loss and reducing the thermalization loss.

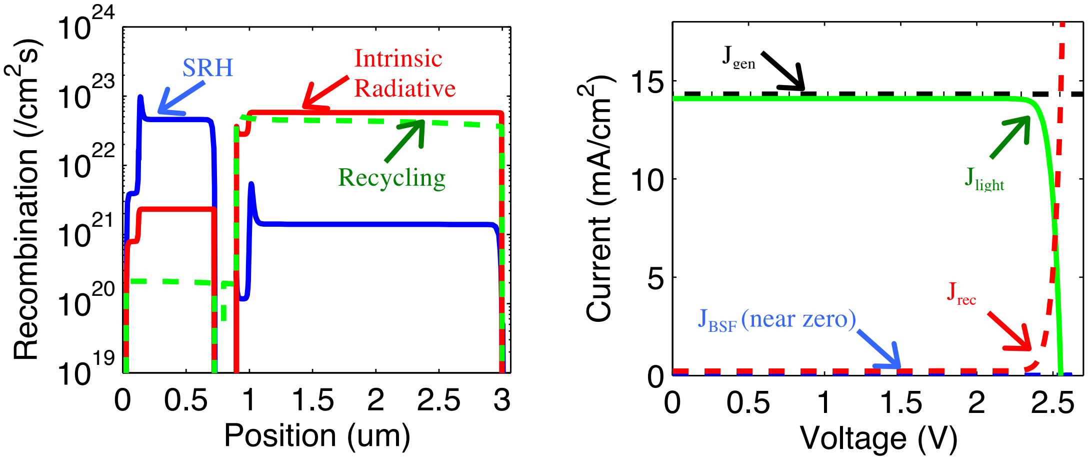

Fig. 4.6. (a) Recombination versus position at V_{OC}, and (b) the generation current (J_{gen}), the terminal current under light (J_{light}), the recombination current (J_{rec}) versus applied voltage. The leakage current through the BSF of top GaInP cell (J_{BSF}) is negligible in this case.

From the spatially resolved recombination profile, we also see that while the GaAs solar cell is dominated by radiative recombination, the GaInP cell has comparable levels of radiative and SRH recombination. From this plot, we can estimate the IRE of GaAs is at ~99%, while the IRE of GaInP is at ~18.5%. These are in agreement with reports in literature [107].

Besides the spatially resolved recombination profile, another way of looking at the loss mechanisms is by their recombination route. Here we consider two possibilities. The first route is recombination inside the bulk layers, which is illustrated by the spatially resolved recombination profile in Fig. 4.6(a). The second route is recombination by escaping through the FSF and BSF, and it has at four different scenarios: 1) holes in GaInP emitter overcome the AlInP FSF, 2) electrons in GaAs base overcome the AlGaAs BSF, 3) electrons in GaInP base overcome the AlGaInP BSF, and 4) holes in GaAs emitter overcome the AlGaAs FSF. The first two scenarios result in losses at the contacts, while the last two scenarios allow minority carriers leak into the tunnel junction and recombine through tunneling. Shown in Fig. 4.6(b), the light IV (J_{light}) can therefore be partitioned into three components

$$J_{light}(V) = J_{gen} - J_{rec}(V) - J_{SF}(V) \tag{4.5}$$

where J_{light} is the light generated current, J_{rec} is the bulk recombination current, and J_{SF} is the total leakage loss through the FSF and BSF in scenarios (1)-(4) listed above, which in this case, is negligible.

4.5.2 Effects of Mirror Reflectivity

A previous GaInP/GaAs tandem cell fabricated by NREL showed an efficiency of 29.5% [117]. By using epitaxial lift-off, the GaAs substrate was removed and replaced with a reflective mirror on the back. The resulting 31.1% efficiency was credited to the enhanced photon recycling in the thin-film structure [105].

One of the most important design aspects that directly impacts the effectiveness of the thin-film approach is the backside mirror reflectivity. Since the emitted photons have energy close to the semiconductor bandgap, they are not strongly reabsorbed and need to bounce around the device many times. Photons strike the backside mirror repeatedly, so even a slightly imperfect mirror can produce significant amount of parasitic absorption.

The change in V_{OC} of the baseline tandem cell with different backside mirror reflectivity is shown in Fig. 4.7(a). To accommodate the uncertainty of GaInP material quality, two curves with GaInP IREs of 19% and 85% are plotted to show the effects of non-radiative recombination in the top GaInP cell. With increasing mirror reflectivity, the V_{OC} increases super-linearly, i.e., the same amount of improvement in mirror reflectivity produces a higher increase in V_{OC} if the mirror reflectivity is already high. Pushing the mirror reflectivity beyond what a simple metallic layer can offer is a challenging task; advanced photonic mirrors may be required to closely approach 100% reflectivity [30]. With higher GaInP IRE, the minimal V_{OC} increases since the non-radiative recombination is reduced. In the best-case scenario with no non-radiative recombination, the tandem cell is estimated to reach a V_{OC} of 2.72 V with a perfect backside mirror.

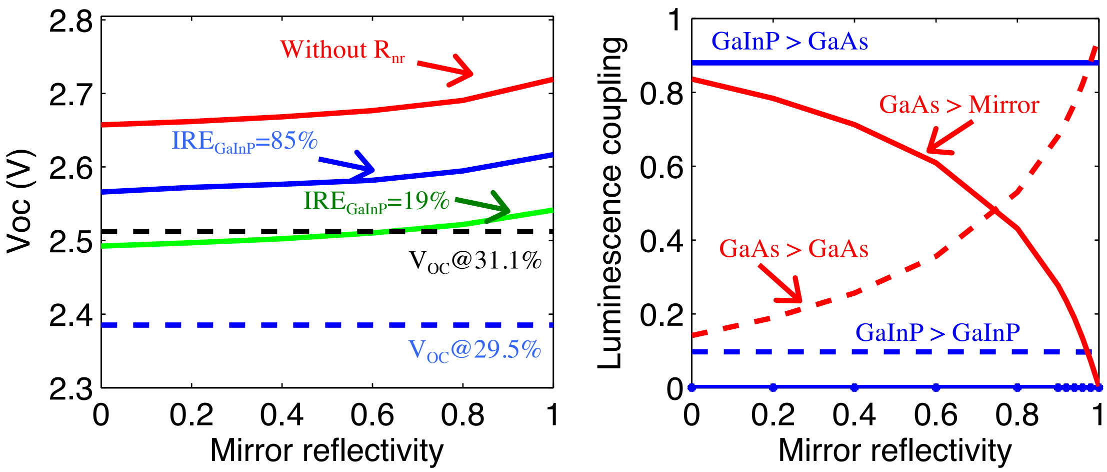

Fig. 4.7. (a) The effect of mirror reflectivity on V_{OC} with GaInP IRE = 19% (green line), IRE = 85% (blue line), and without (red line) non-radiative recombination (R_{nr}). The V_{OC} values for the NREL 31.1% cell (black dash line) and the NREL 29.5% cell (blue dash line) are provided as reference. (b) Luminescence coupling inside the cell among the top GaInP cell, the bottom GaAs cell, and the mirror.

The effects of the backside mirror on the top and bottom cells are however not equal. This is illustrated in Fig. 4.7(b), which shows the relative amount of luminescence coupling from one cell to the other or the backside mirror. The emission from GaInP top cell is mostly unaffected by the change in mirror reflectivity, because most of it is absorbed by the GaAs bottom cell. The recycling of the GaInP luminescence by the GaAs bottom cell is so strong that almost no photons reach the backside mirror. On the other hand, the effect of mirror reflectivity on the GaAs bottom cell is significant, and the GaAs luminescence does not couple to the top GaInP cell, since the emitted photons have energy less than the GaInP bandgap. Therefore, the thin-film approach only benefits the bottom GaAs cell in terms of photon recycling.

4.5.3 Effects of GaInP Top Cell Back-surface Field

One intriguing fact about the results shown in Fig. 4.7(a) is that, even in the worst scenarios with 0% mirror reflectivity, the V_{OC} does not drop to a value comparable to the 2.385 V for the 29.5% tandem cell [117], despite the similarities between the two structures. The structure of the 29.5% tandem cell is shown in Fig. 4.8(a) [117]. The only remaining major difference with the 31.1% baseline cell is the choice of BSF for the top GaInP/GaAs junction: in the 29.5% cell, a heavily doped GaInP layer is used instead of a higher bandgap AlGaInP layer. The overall band diagram is shown in Fig. 4.8(b).

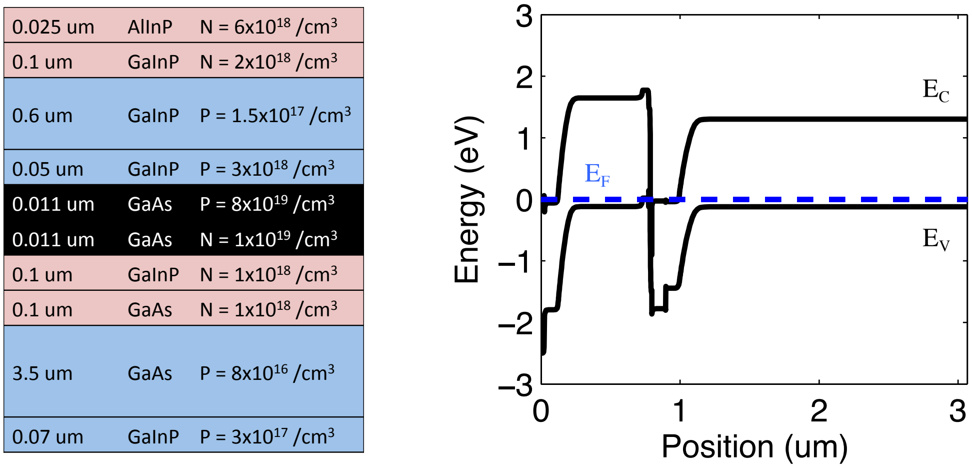

0.025 um	AlInP	N = 6×10^{18} /cm^3
0.1 um	GaInP	N = 2×10^{18} /cm^3
0.6 um	GaInP	P = 1.5×10^{17} /cm^3
0.05 um	GaInP	P = 3×10^{18} /cm^3
0.011 um	GaAs	P = 8×10^{19} /cm^3
0.011 um	GaAs	N = 1×10^{19} /cm^3
0.1 um	GaInP	N = 1×10^{18} /cm^3
0.1 um	GaAs	N = 1×10^{18} /cm^3
3.5 um	GaAs	P = 8×10^{16} /cm^3
0.07 um	GaInP	P = 3×10^{17} /cm^3

Fig. 4.8. GaInP/GaAs tandem solar cell modeled after the NREL 29.5% cell [117]: (a) device structure, and (b) band diagram under equilibrium.

As seen in Fig. 4.9(a), the effect of using a p+ GaInP BSF is a significant drop in V_{OC}. The J_{SC} and EQE, shown in Fig. 4.9(b), remain mostly unaffected. It seems surprising that, without changing any material parameter, the simulated results are able to match the measured results so well. This is what we will look into next.

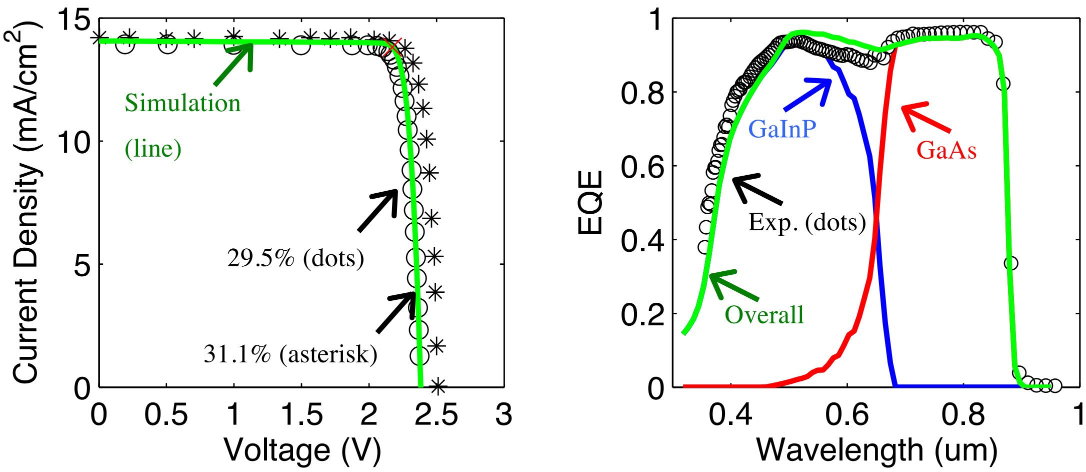

Fig. 4.9. (a) Simulated IV (green line) compared with measured NREL 31.1% cell (black asterisk) and NREL 29.5% cell (black dots), and (b) Simulated EQE from top GaInP cell (blue line) and bottom GaAs cell (red line). The two combined (green line) is compared with the measured EQE (black dots) from the NREL 29.5% cell.

The origin of the lowering in V_{OC} becomes apparent when we look at the loss components shown in Fig. 4.10(a). Unlike the situation seen in Fig. 4.6(b), the leakage loss through the BSF and FSF dominates over the loss through bulk recombination loss. In another word, the p+ GaInP BSF is not as effective as the AlGaInP BSF used in the 31.1% cell, and it is the primary reason for the decrease in V_{OC}. When the backside mirror reflectivity changes, the mirror benefits the bottom GaAs solar cell, thus the V_{OC} increases. However, having a higher IRE or completely eliminating the SRH recombination does not significantly increase the minimal V_{OC}, since the dominant loss—the leakage through p+ GaInP BSF remains.

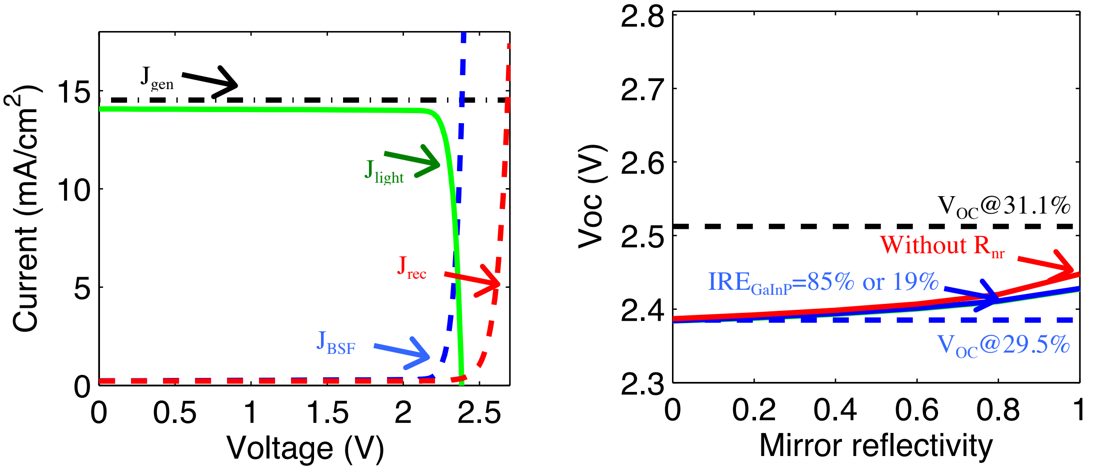

Fig. 4.10. (a) The generation current (J_{gen}), the terminal current under light (J_{light}), the recombination current (J_{rec}), and the leakage current through the BSF of top GaInP cell (J_{BSF}) versus applied voltage. (b) The effect of mirror reflectivity on V_{OC} with GaInP IRE = 19% or IRE = 85% (green line, since both lines are very close), and without (red line) non-radiative recombination (R_{nr}). The V_{OC} values for the NREL 31.1% cell (black dash line) and the NREL 29.5% cell (blue dash line) are provided as reference.

With Fig. 4.11(a), (b), and (c), a quantitative comparison between the 29.5% cell and 31.1% cell illustrates the importance of optimizing the BSF and IRE of the top GaInP cell. Without an effective BSF, 86.7% of the recombination loss is through the BSF leakage current at $V_{OC.}$ This leakage can be prevented by using a heterojunction, conduction band barrier such as AlGaInP, which would allow the V_{OC} to increase significantly. After that, the limiting loss becomes the non-radiative recombination occurring inside the GaInP top cell. As seen in Fig. 4.11(c), even with 85% of GaInP IRE, the non-radiative recombination is still significantly higher than radiative recombination. Therefore, increasing the GaInP IRE to a level matching that of GaAs becomes the critical task for improving the cell efficiency toward the Shockley-Queisser limit. As shown in Table 1, improving the backside mirror reflection to 100% increases efficiency to 31.4%. Also using a high quality material with IRE of 85% leads to efficiency of 32.3%.

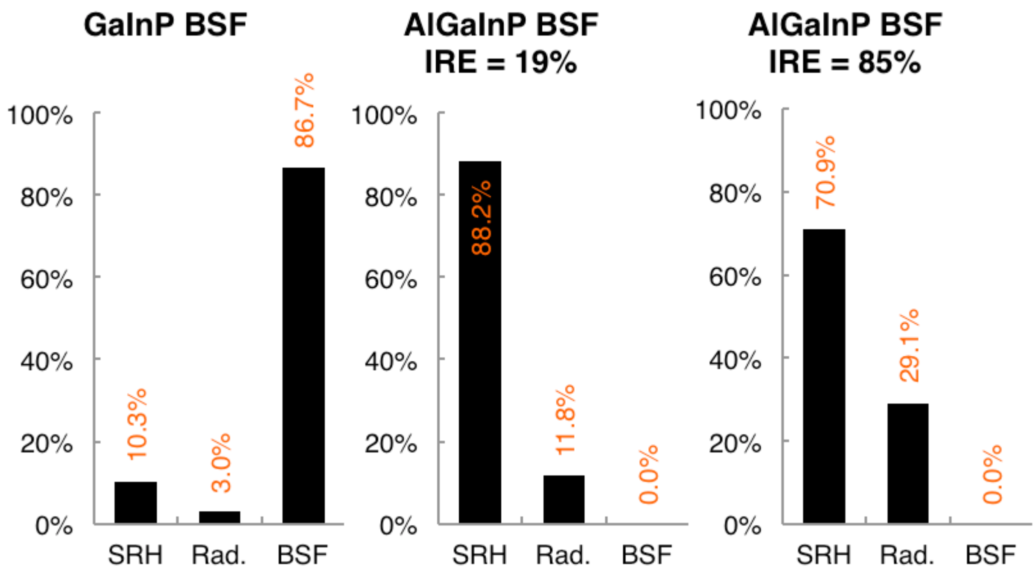

Fig. 4.11. Percentage of each loss mechanism at V_{OC}: (a) with a less efficient GaInP BSF, (b) with AlGaInP BSF and GaInP IRE = 19%, and (c) with AlGaInP BSF and GaInP IRE = 85%.

Table 4.1. Summary of cell performance for various structures investigated by this study. The shaded rows are benchmarked to have similar structure to the experiments.

	Mirror Refl.	GaInP IRE	η	V_{OC} (V)	J_{SC} (mA/cm^2)	Ref.
GaInP BSF	0%	19%	29.6%	2.38	14.06	[117]
	60%	19%	29.9%	2.40	14.06	
AlGaInP BSF	0%	19%	30.8%	2.49	14.09	
	60%	19%	31.1%	2.52	14.09	[105]
	100%	19%	31.4%	2.54	14.08	
	100%	85%	32.3%	2.61	14.09	

4.6 Summary

In this work, a state-of-the-art GaInP/GaAs tandem cell is analyzed using an electro-optically coupled simulator. Even at its efficiency of 31.1%, it is shown to have a wide room for further efficiency increase. In particular, the top GaInP cell is found to be the limiting component for recombination losses. The BSF for the top GaInP cell needs a high bandgap heterojunction in order to effectively block the minority carrier leakages, and the IRE of the GaInP material needs to be further improved to match that of the GaAs. This work predicts that improved mirror and IRE of 85% would increase the efficiency up to 32.3%.

5 CHARACTERIZATION OF SOLAR CELLS WITH THE RECIPROCITY THEOREM

5.1 Preface

The contents of this chapter have been extracted from the following publications with permission: X. Wang and M. S. Lundstrom, "On the Use of Rau's Reciprocity to Deduce External Radiative Efficiency in Solar Cells," *IEEE Journal of Photovoltaics,* pp. 1-6, 2013.

5.2 Introduction

The radiative emission of a solar cell can be a good indicator of its intrinsic quality [49, 108, 120, 121]. The external radiative efficiency (ERE) of a solar cell at its open-circuit voltage (V_{OC}) can be defined, as suggested by Green [109], as

$$ERE \equiv \frac{q\phi_{emit}}{J_{dark}(V_{oc})} \tag{5.1}$$

where ϕ_{emit} is the total photon flux emitted from the cell and $J_{dark}(V_{oc})$ is the dark current at the V_{oc}. The emitted photon flux can be measured [122-125], but it is not a standard part of solar cell characterization. Given the importance of ERE as a measure of solar cell performance, it would be highly desirable to deduce it from standard solar cell characterization measurements.

To address this need, Rau has proposed a surprisingly simple formula that links a solar cell's ERE with its V_{oc}, short circuit current (J_{sc}), and external quantum efficiency (EQE) as [126]

$$ERE = \frac{\exp(qV_{oc}/kT)\int_0^\infty \phi_B(E)EQE(E)dE}{J_{sc}} \tag{5.2}$$

$$\phi_B(E) = \frac{2\pi q}{h^3 c^2} \frac{E^2}{\exp(E/kT) - 1} \tag{5.3}$$

where ϕ_B is the Planck's formula, q is the elementary charge, c is the speed of light, h is Planck's constant, k is Boltzmann's constant, T is the temperature of the cell, and E is the photon energy. In several subsequent works, Rau and others expanded the connection to both photoluminescence (PL) and electroluminescence (EL) [82], and applied (5.2) to different types of solar cells including CIGS [127]. Recently, Green has applied [109] to a comprehensive set of solar cells ranging from standard c-Si solar cells to organic solar cells. The ERE values deduced from (5.2) showed reasonable agreement with independently measured ERE values or with expectations in cases for which no measured data was available.

The Rau reciprocity relation (RRR), (5.2), is based on several assumptions including the validity of the Donolato theorem [128] and superposition [126]. Derived from the principle of detailed balance, the Donolato theorem is a reciprocity relation that states the current collected by the junction surface, S_j in the presence of a unit point source of carriers at location r is the same as the excess minority-carrier density at r due to a unit carrier density injected on S_j. The superposition principle states that the illuminated IV characteristics of a solar cell $J_{light}(V)$ is composed of the voltage dependent dark injection current $J_{dark}(V)$ and the short circuit current under illumination J_{sc}

$$J_{light}(V) = J_{dark}(V) - J_{sc} \tag{5.4}$$

The work so far has been analytical, starting from these assumptions. In order to test the validity of (5.2) and understand the conditions under which it may break down, a comprehensive numerical study is needed. In this work, we perform such a study for some common types of thin film solar cells using an established optical/electrical numerical simulator, ADEPT 2.0 [57]. The results provide insights into the validity of (5.2).

The chapter is organized as follows. Our thermodynamically self-consistent electrical-optical model has been described previously [81]; it is briefly reviewed in Sec. 5.3. In Sec. 5.3, we also define three model structures: i) a thin-film GaAs cell for which we expect the RRR to hold, ii) a CIGS cell for which superposition fails due to the presence of charged traps, and iii) a CdTe cell for which superposition fails due to the presence of a Schottky barrier at the back contact. In Sec. 5.4, we use numerical simulations to extract the ERE of each of these cells and then compare the results to the ERE deduced from (5.2). Section5.5 is a discussion of the results and the conditions under which (5.2) can fail. We conclude in Sec. 5.6 with some general guidelines for using (5.2) in solar cell analysis.

5.3 Approach

5.3.1 Self-consistent Optical Module with the Semiconductor Equations

Since the ERE and the RRR involve both optical (generation, emission, etc.) and electrical aspects (recombination, drift and diffusion transport, etc.), the numerical framework used to study this problem must be overall self-consistent. In this study, we use an enhanced version of ADEPT 2.0, which solves the semiconductor device equations. ADEPT 2.0 is a 1D self-consistent solar cell simulator capable of simulating layered structures. The simulator is well calibrated and is numerically sound. The enhanced version includes photon recycling based on an approach similar to that of Durbin [56]. The details of this implementation are described in. For this work, ADEPT 2.0 has been further upgraded to track the angle and spatially resolved radiative photon emission at the front and back of the solar cell.

5.3.2 Model Structures

In this study, we focus on three types of thin film solar cells: GaAs, CIGS, and CdTe. GaAs thin film solar cells currently have the highest reported efficiency (28.8%) for single junction solar cells under 1-sun conditions [12]. The extraordinary intrinsic quality of GaAs double heterostructures gives these cells a very high Shockley-Read-Hall (SRH) lifetime and low surface recombination, and as a result, radiative emission from such cell can be very high [49]. Thus, it can serve as a benchmarking structure where intrinsic radiative emission dominates.

CIGS solar cells can also reach high efficiencies (above 20%) [12]. Unlike the GaAs cells, they display a nonsuperposition behavior—their illuminated and dark IVs cross-over slightly beyond V_{oc} . In addition, the SRH lifetime is low - on the order of nanoseconds due to grain boundaries and bulk defects [129]. As a result, the external radiative efficiency is low in CIGS devices [127]. Compared to GaAs solar cells, which operate as near-ideal P-N junction diodes, CIGS solar cells provide us with an opportunity to examine a cell for which superposition fails and nonradiative recombination dominates.

The third solar cell to be examined is a CdTe cell, which also achieve high efficiency but can display a nonsuperposition behavior due to a hole-blocking Schottky barrier at the back contact [95, 130]. The methods used to investigate the three types of solar cells we chose in this study can be extended to other types of solar cells.

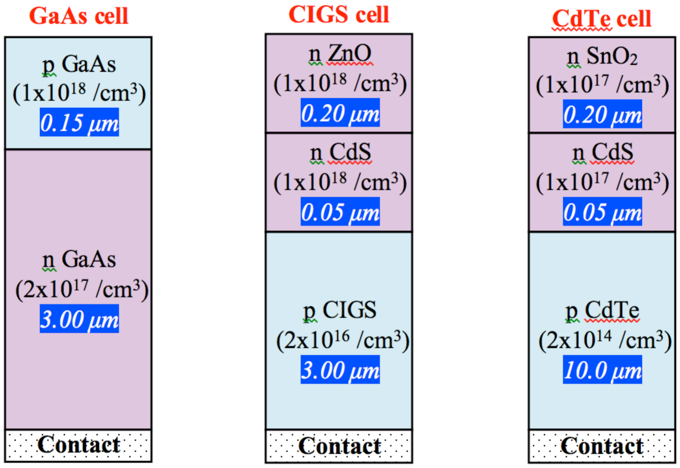

Fig. 5.1. (a) Baseline single junction GaAs thin film solar cell with reflective back contact. (b) Baseline CIGS solar cell modeled after Gloeckler [131]. (c) Baseline CdTe solar cell modeled after Demtsu [95].

Fig. 5.1 illustrates the device structures for the GaAs, CIGS, and CdTe solar cells. The model GaAs cell is a simplified version of the structure studied in [93]. Since we do not explicitly simulate the AlGaAs layers passivating the GaAs, an effective surface recombination velocity of 100 cm/s for both top and bottom surfaces are used. Except for the doping density, parameters are identical for both p-type emitter and n-type base. Bandgap reduction due to heavy doping is not included in this study. As discussed in [52], the Roosbroeck-Shockley equation is used to relate the radiative recombination coefficient, *B*, to the GaAs absorption coefficient. The GaAs absorption coefficients are from experimental data by Lush [48]. A high mirror reflectivity (95%) is used as suggested in [7] as a critical requirement toward high photon recycling and thus high solar cell efficiency.

The baseline CIGS cell structure and material parameters are modeled after Gloeckler [131]. Instead of specifying lifetime, the defect density model is used for SRH recombination with the trap density, energy distribution and capture cross sections specified. We use a Gaussian distribution of defects centered at mid-gap. The conduction band offset at the heterojunction interface between the CdS and CIGS layers is set to 0.3 eV. Radiative emission from the ZnO and CdS layers is minimal because these layers are very thin and have high bandgaps compared to CIGS. Thus, we set the indices of refraction for all layers to be the same as GaAs (3.3) to make later comparisons easier to comprehend. In this study, the specific values of refractive index for each semiconductor layer have minor impact on the results. The refractive index is only used to calculate the escape cone at front surface. Since the ERE values from both RRR and direct computation are calculated through the same optical module, the choice of refractive indices equally affect both calculations. The absorption coefficients for the three layers are taken from [131, 132].

The CdTe solar cell is modeled after [95]. It is very similar to the CIGS cell except for a lighter base doping (2×10^{14} /cm^3) and a hole-blocking Schottky barrier at the back contact. In this study, we vary the Schottky barrier height to investigate different degree of nonsuperposition. For both CIGS and CdTe solar cells, the back contacts are made from molybdenum with 80% reflectivity [131].

Important material parameters for the baseline GaAs, CIGS, and CdTe cells are summarized in

Table 5.1.

Table 5.1. Important device parameters for (a) the baseline solar cells, (b) the baseline CIGS solar cell, and (c) the baseline CdTe solar cell. Parameters: donor-like (acceptor-like) defect density N_{DG} (N_{AG}); donor-like (acceptor-like) defect peak energy E_D (E_A); trap Gaussian distribution width W_G; and capture cross-section σ.

GaAs emitter/base			**(a)**
Bandgap	1.414 eV	Index n	3.3
Mobility (e)	250 cm^2/V-s	Mobility (h)	500 cm^2/V-s
SRH lifetime	1 μs	Auger coeff.	7×10^{-30} cm^6/s
Surface rec. velocity	100 cm/s (front, rear)	Backside mirror refl.	95%

CdS n+ emitter			**(b)**
Bandgap	2.4 eV	Index n	3.3
N_{AG}	10^{18} /cm^3	E_D	mid-gap
W_G	0.1 eV	σ_e σ_h	10^{-17} cm^2 10^{-12} cm^2
CIGS p-type base			
Bandgap	1.15 eV	Index n	3.3
Mobility (e)	100 cm^2/V-s	Mobility (h)	25 cm^2/V-s
N_{DG}	10^{14} /cm^3	E_D	mid-gap
W_G	0.1 eV	σ_e σ_h	5×10^{-13} cm^2 10^{-15} cm^2
Surface rec. velocity	10^7 cm/s (front, rear)	Backside mirror refl.	80%

CdTe p-type base			**(c)**
Bandgap	1.5 eV	Index n	3.3
Mobility (e)	320 cm^2/V-s	Mobility (h)	40 cm^2/V-s
SRH lifetime	1 ns	Backside mirror refl.	80%

5.4 Results

5.4.1 GaAs Solar Cell

As discussed in [126], the validity of the RRR is a sufficient condition for the superposition principle and vice versa. It is therefore helpful to start with a well-behaved p-n junction that obeys superposition. We start with a simple GaAs solar cell.

Fig. 5.2 displays the band diagram and IV characteristics of the GaAs solar cell. The illuminated and dark IV displays no cross-over point so the RRR should hold. As shown in Fig. 5.3, the ERE values derived from the direct calculation and the RRR agree very well for cases of different mirror reflectivities and carrier lifetimes. Furthermore, not shown here are the results for various base thickness and mobilities, which produce results similar to those in Fig. 5.3.

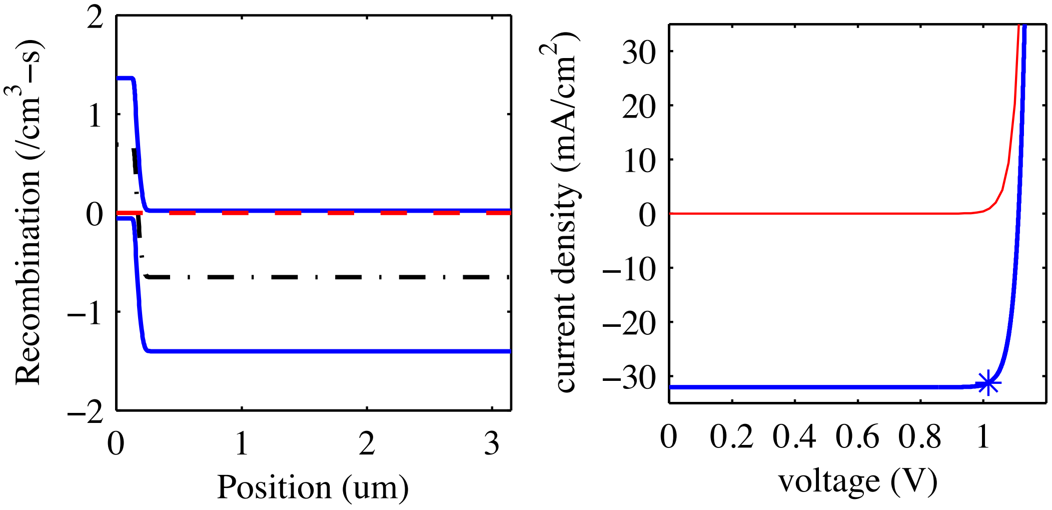

Fig. 5.2. (a) Equilibrium band diagram for the baseline GaAs solar cell. (b) Illuminated (AM1.5G) and dark IV displaying superposition behavior. The asterisk symbol marks the maximum power point (MPP).

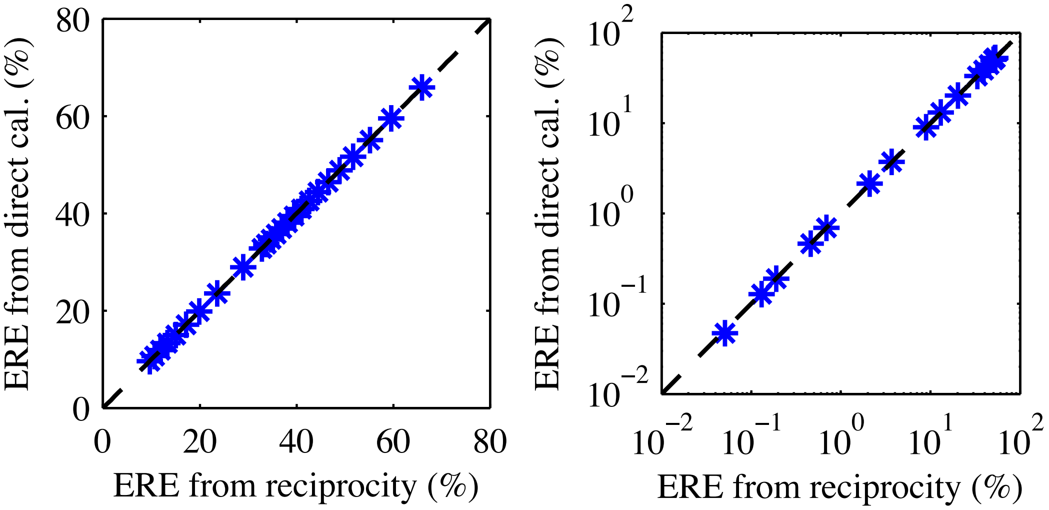

Fig. 5.3. (a) ERE values derived from the RRR and direct calculation for different mirror reflectivities (0% - 100%). (b) ERE values derived from the RRR and direct calculation for different base minority carrier lifetime (10 ps – 100 μs).

5.4.2 CIGS Solar Cell with Trap-induced Nonsuperposition

It is well known that in CIGS solar cells, nonsuperposition behavior can cause the illuminated and dark IVs to cross-over each other. The equilibrium band diagram is shown in Fig. 5.4(a). Compared to the baseline GaAs cell, the CIGS cell has a lighter doping in the base and a larger depletion region (~ 200 nm). In addition, the cell has a heterojunction at the front due to CdS/CIGS interface.

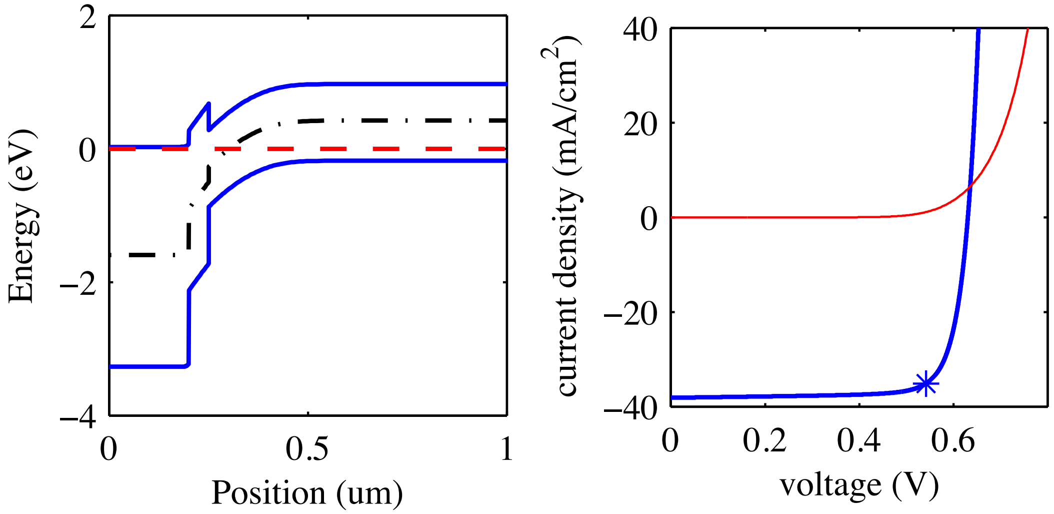

Fig. 5.4. (a) Equilibrium band diagram for the baseline CIGS solar cell. (b) Illuminated (AM1.5G) and dark IV displaying nonsuperposition behavior. The asterisk symbol marks the maximum power point (MPP).

As pointed out in [131], the conduction band barrier height ΔE_C is a critical factor controlling the cell's nonsuperposition behavior. The CdS layer contains acceptor-like traps that, under illumination when excess amount of electrons and holes are generated within the n-type CdS emitter, the acceptor-like traps will capture the excess holes and become neutral [133, 134]. When the illumination is terminated, the decrease in hole population causes the neutral acceptor-like traps to give up the captured holes and become negatively charge. This as a result causes the bands of CdS shift upward in energy as if a negative bias has been applied to it. In other words, the barrier essentially acts as an illumination-dependent series resistance impeding the flow of electron current in dark. The illuminated and dark IVs showing cross-over are displayed in Fig. 5.4(b).

The RRR is not expected to hold for solar cells that do not display superposition. Fig. 5.5(a) shows the comparison for various values of ΔE_C. Clearly, the RRR no longer holds in this case. Moreover, the disagreement between the ERE determined directly and by the RRR increases as the band discontinuity increases and the cross-over becomes more severe as shown in Fig. 5.5(b). More interesting is the fact that the discrepancy between the two approaches has different trends. Increasing conduction band offset decreases the actual ERE but has virtually no effect on the value deduced from the RRR.

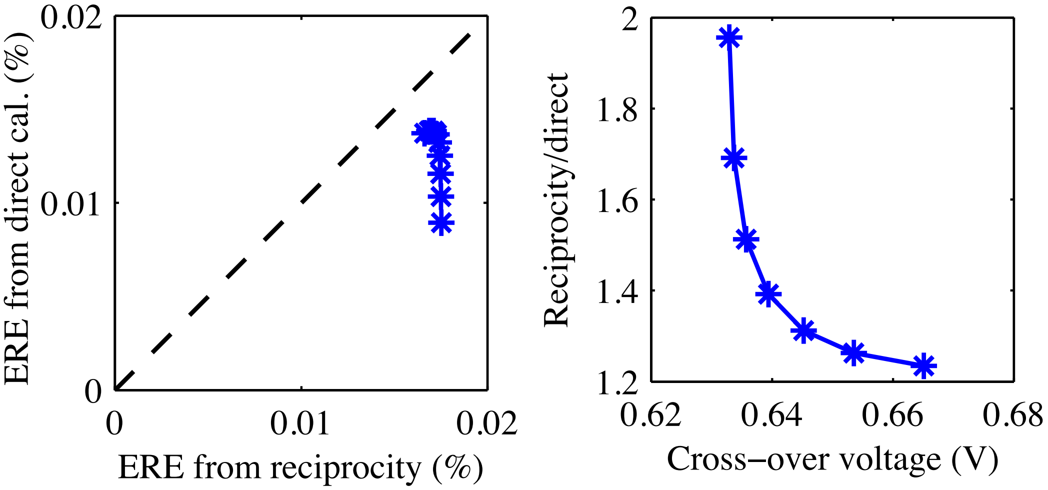

Fig. 5.5. (a) ERE values derived from the RRR and direct calculation for different ΔE_C (0.1 eV – 0.5 eV, with 0.05 eV increments). (b) Ratio between ERE values from direct computation and the RRR vs. J-V cross-over voltages in Fig. 5.5(a).

The observation can be understood as follows. In dark, the CdS layer acts as a series resistance delaying the turn-on of the diode. The higher the CdS barrier, the lower the current, and the more recombination occur within the depletion region where non-radiative recombination is more effective than radiative. As a result, the ERE is inversely related to the height of the CdS barrier.

Under illumination, the CdS barrier lowers, and the series resistance it introduced also drops significantly to a point that the cell performance is minimally affected. As a result, the height of the barrier has virtually no effect on the EREs derived from the RRR.

Fig. 5.6 examines two more cases. As shown in Fig. 5.6(a), increasing the CIGS lifetime increases both the actual ERE and the value deduced from the RRR. Some error occurs when using the RRR, but the trend is the same. Fig. 5.6(b) shows a more interesting behavior as the trap density in the CdS is varied. Increasing trap density decreases the actual ERE but has almost no effect on the value deduced from the RRR. This behavior is similar to what was observed for the varying conduction band discontinuity in Fig. 5.5. Under dark conditions, with increasing acceptor-like trap concentration in the CdS layer, the CdS barrier height increases and more strongly impedes the electron current. As a result, the actual ERE decreases with increasing trap density. Under illumination, the traps become neutral and have minimal effect in impeding the electron current flow. Thus, the ERE derived from the RRR is unaffected by a change of the trap density.

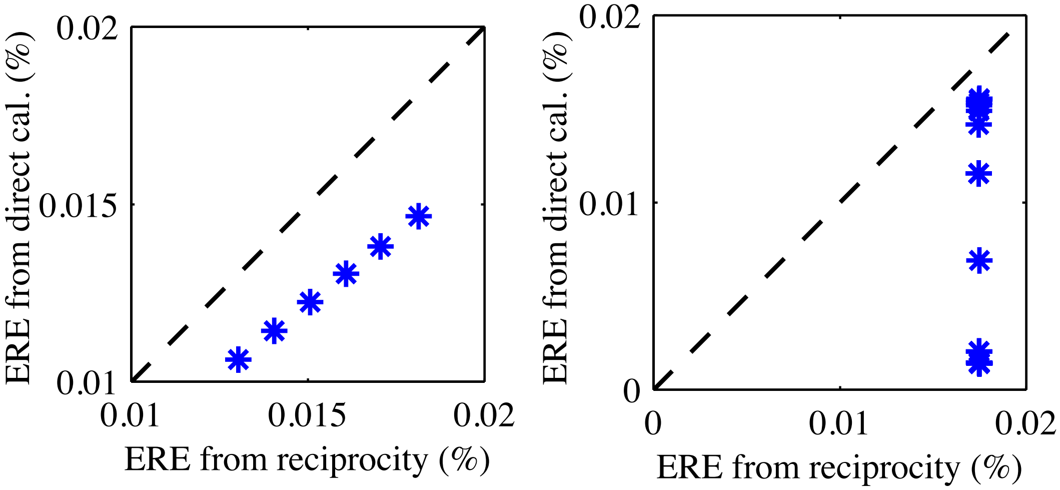

Fig. 5.6. (a) ERE values derived from the RRR and direct calculation for different mirror reflectivities (0% - 100%, with 20% increments). (b) ERE values derived from the RRR and direct calculation for different trap density (8.5×10^{17}, 9×10^{17}, 1×10^{18}, 1.5×10^{18}, 2×10^{18}, 2.5×10^{18}, and 3×10^{18} /cm^3) in CdS layer. Conduction band offset is set at 0.3 eV and is unaffected by the trap density.

5.4.3 CdTe Solar Cell with Backside Schottky Barrier-induced Nonsuperposition

CdTe solar cells with a backside Schottky barrier can display nonsuperposition behavior very much like the CIGS solar cells as displayed in Fig. 5.7. The situation in a real CdTe solar cell is complicated with the presence of both a Schottky back contact and a valence band offset at the CdS/CdTe interface. As shown in Fig. 5.8(a), the RRR seriously under-estimates the true ERE. This is opposite to what we observed in case of the CIGS cells, indicating that, although both types of cells display nonsuperposition, the mechanisms behind the deviation of the RRR from the true ERE values are different.

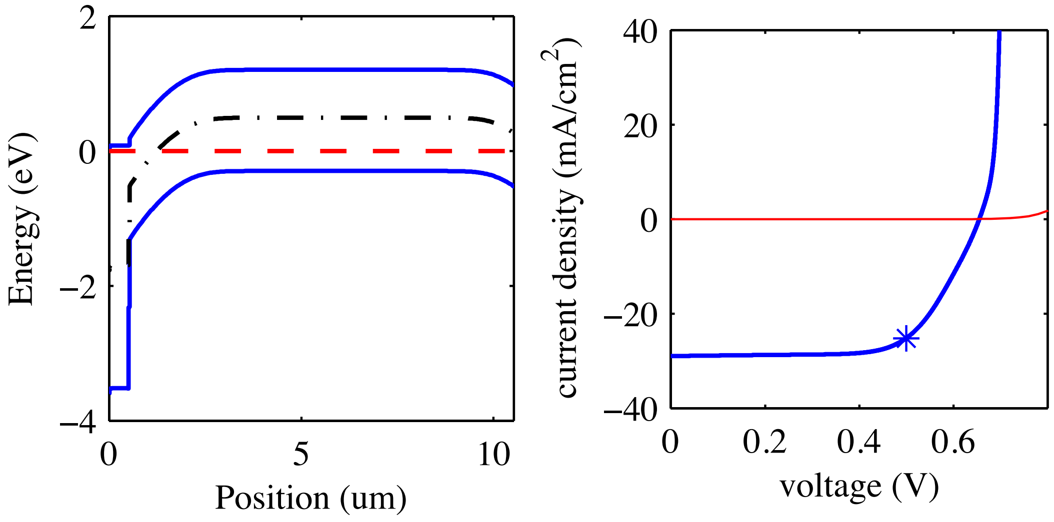

Fig. 5.7. (a) Equilibrium band diagram for the baseline CdTe solar cell. (b) Illuminated (AM1.5G) and dark IV displaying nonsuperposition behavior. The asterisk symbol marks the maximum power point (MPP).

The reason for the failure of the RRR in case of CdTe cell rests in the conservation of charge. Let us begin with the equilibrium band diagram in Fig. 5.7(a). If the cell is suddenly illuminated, excess electrons and holes are generated. The excess holes have only two routes to exit the structure: 1) by recombination with electrons, and 2) by escaping through the rear Schottky barrier.

Under short-circuit conditions, the bulk recombination is minimal, so most excess holes escape by the Schottky barrier. To permit this increase in hole current, the bands in the CdTe quasi-neutral region shift downward in energy forward biasing the Schottky barrier. At the same time, the voltage drop across the front p-n junction is also reduced. This means less applied voltage is needed to reach the open circuit condition, and thus the V_{OC} is reduced.

The Schottky barrier, however, has little to no impact on J_{SC}. This means that if we compare a CdTe solar cell with a Schottky back contact to one without, we expect to see a reduced V_{OC}, but similar EQE and J_{SC}. As a result, the RRR under-estimates the ERE, and this is exactly what we observe in Fig. 5.8(a). Notice the difference between the two approaches increases exponentially as the Schottky barrier height increases. This occurs because the change in V_{OC} is proportional to the change in barrier height, but the V_{OC} enters the RRR as $\exp(qV_{OC}/kT)$.

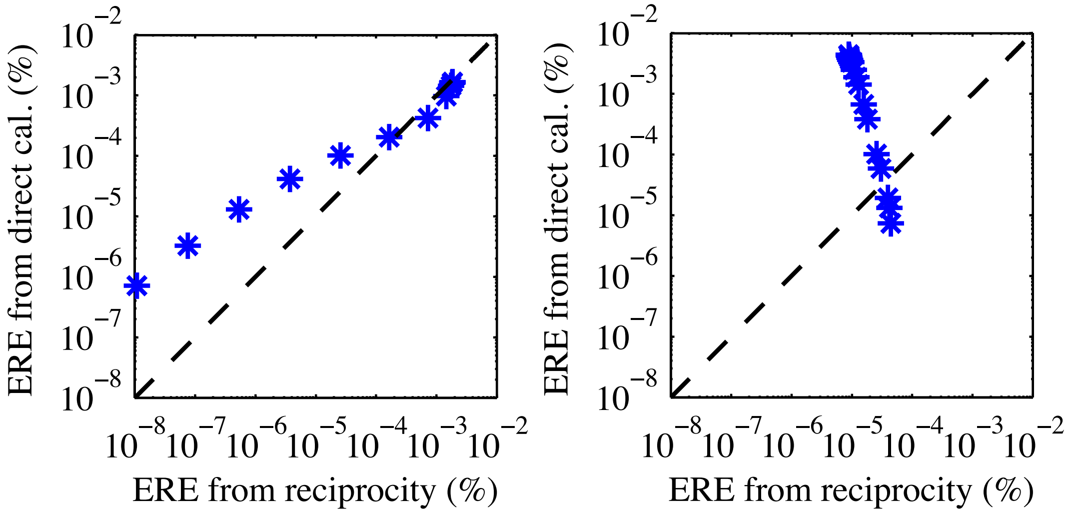

Fig. 5.8. (a) ERE values derived from the RRR and direct calculation for different Schottky barrier height (0 eV – 0.5 eV, with 0.05 eV increments). (b) ERE values derived from the RRR and direct calculation for different base minority carrier lifetime (10 ps – 100 μs) with a Schottky barrier height of 0.4 eV.

When the CdTe lifetime is varied, the resulting comparison between ERE values from the RRR and direct calculation is intriguing. The increasing ERE from the direct calculation with increasing lifetime is expected since higher non-radiative lifetime permits more radiative emission. The decreasing ERE from the RRR with increasing lifetime is however counter-intuitive and can be explained as follows.

With low carrier lifetime, the majority of the recombination occurs within the bulk. The bulk recombination increases as the cell is biased toward V_{OC}. However, not all of this applied bias drops across the front p-n junction. The increased bulk recombination requires an increased supply of holes, which is accomplished by reverse biasing the Schottky barrier. Thus, part of the applied bias in fact goes to reverse biasing the rear Schottky barrier. As a result, the cell with a lower carrier lifetime requires more voltage to be applied to reach open-circuit condition and thus has a higher V_{OC}. This however does not mean a lower lifetime will yield a more efficient solar cell. The increasing reverse bias on the Schottky barrier as the cell is biased toward V_{OC} acts as an increasing series resistance that severely degrades the fill-factor. As a result of this fill-factor degradation, the cell efficiency decreases with decreasing lifetime, despite the slight increase in V_{OC}. Similar counterintuitive behaviors are also reported in [135] where the rate of photoluminescence decay increases with mobility with the presence of strong surface recombination.

5.5 Discussion

From the previous section, we have seen that the most significant factor deviating the ERE calculated using the RRR from its true value is the violation of the superposition principle. In addition, we observe that as the nonsuperposition behavior becomes increasingly severe, the deviation becomes larger.

As Moore *et al.* pointed out in [94], nonsuperposition in fact can be observed in all types of solar cells due to bias dependent light generation current. As the solar cell is biased toward the built-in voltage, V_{bi}, the built-in electric field reduces, and eventually the light generated carriers will have equal chance to reach both contacts. At this point, the light generated current becomes zero, and the dark and illuminated IVs cross-over. This universal nonsuperposition behavior however is not the cause for the error of the RRR. In fact, in the typical solar cells we investigated in this work, the V_{OC} is far below V_{bi}. At V_{OC}, there is still a significant built-in electric field remain, and the light induced current is not much different from J_{SC}.

The nonsuperposition behavior we observed in the CIGS and CdTe cells is at voltages significantly below V_{bi}. The cause is the dynamic change in their band diagrams under illuminated and dark conditions, instead of the bias dependent light induced current. In the CIGS cell, the CdS layer acts as an illumination-dependent series resistance; and in the CdTe cell, the charge conservation introduces an illumination-dependent bias across the Schottky barrier. This causes the RRR, which assumes identical band diagram under illuminated and dark conditions, to fail.

As a rule of thumb, one should expect the RRR to fail when the cross-over voltage is near V_{bi}. For some situations, the RRR produces errors in the magnitude of the ERE, but displays the correct overall trends (e.g. Fig. 5.6(a) and Fig. 5.8(a)). For other situations, however, the RRR produces trends that are different – even opposite to the correct ERE (e.g. Fig. 5.6(b) and Fig. 5.8(b)).

5.6 Summary

The external radiative efficiency of a solar cell can be directly measured or indirectly estimated through the Rau reciprocity relation. In this study, we explored the relation between these two techniques using numerical simulation studies of GaAs, CIGS, and CdTe solar cells. We find that the Rau reciprocity relation holds very well for cells obeying the superposition principle and fails when the cross-over voltage is near V_{OC}. The cross-over voltage is therefore a helpful indicator for the validity of applying the RRR. When the RRR fails, it produces errors in the estimated ERE. It is surprising, however, that the RRR can produce trends in the estimated ERE as material parameters are varied that are distinctly different and even opposite to those of the actual ERE. When these limitations are understood, the Rau reciprocity relation can be a very useful technique in the characterization of solar cells.

6 CHARACTERIZATION OF INP THIN FILMS WITH TRPL/PLE/SIMULATION COUPLED APPROACH

6.1 Preface

The contents of this chapter have been extracted from the following publications with permission: X. Wang, J. Bhosale, J. Moore, R. Kapadia, P. Bermel, A. Javey*, et al.*, "Photovoltaic Material Characterization with Steady-State and Transient Photoluminescence," *IEEE Journal of Photovoltaics*, submitted, 2014.

6.2 Introduction

Various characterization techniques based on photoluminescence of semiconductors offer powerful insights into the properties of photovoltaic materials that affect solar cell performance. In particular, the transient form of PL, namely the time-resolved photoluminescence (TRPL) method has been widely used in material lifetime characterization [135-141]. In a TRPL setup, the sample is excited with a short laser pulse. The generated carriers move within the sample and eventually recombine [142]. The resulting radiative emission vs. time plot serves as an indirect probe of the characteristic sample lifetimes. Compared to transient PL, steady-state PL techniques such as photoluminescence excitation spectroscopy (PLE) are far less widely used [125, 143]. In the PLE technique, a constant monochromatic light source is used to excite the sample, and the radiative emission flux from the sample is recorded. The flux ratio between the emission and source yields the external fluorescence efficiency [21]:

$$PLE(\lambda_{in}) = \frac{\phi_{emit}}{\phi_{in}(\lambda_{in})} \tag{5.5}$$

where ϕ_{in} is the incident photon flux at wavelength λ_{in}, and ϕ_{emit} is the radiative emission from the sample.

By varying the incident light wavelength, the external fluorescence efficiency is measured as a function of excitation wavelength. Although PLE does not yield lifetime directly as TRPL does, the external fluorescence efficiency measures the gap between a solar cell and its ultimate radiative efficiency limit. It has therefore been suggested as an effective contact-less method for inline quality control of solar cells [50, 109, 144].

PL-based characterization is important and widely used, but also challenging to interpret when applied to materials with novel compositions or growth methods. In such cases, the PL data usually does not always follow simple analytical models [145-148]. For example, it has been shown that the presence of a junction or surface band-bending can lead to a false observation of significantly larger lifetime in a TRPL measurement [135, 149]. Moreover, traditional TRPL is limited by the strong absorption near the sample surface, according to Beer's law. Novel and complex techniques such as the two-photon excitation method must be applied to remedy this shortcoming [150, 151]. Thus, an analytical parameter fit is often insufficient to capture the many uncertainties and subtleties in material properties (e.g., lifetime parameters). Therefore, a general and robust method is needed beyond the simple analytical interpretation of the PL data to characterize the various novel photovoltaic materials being developed today.

In this work, using a combination of TRPL and PLE coupled with rigorous numerical simulation, we show that the surface and bulk recombination lifetime can be quantitatively extracted for an arbitrary photovoltaic material. Our experimental and numerical methods are discussed in Sec. 6.3. In Sec. 6.4, we investigate the differing sensitivities of TRPL and PLE to surface and bulk recombination, which explains our reasons to the couple the TRPL and PLE approaches. We then apply our proposed method to evaluate an InP substrate sample and a VLS-grown InP sample in Sec. 6.5. Our conclusions are summarized in Sec. 6.6.

6.3 Method

6.3.1 Experimental Setup

The PLE measurements of thin film samples involve measuring an extremely weak PL signal often accompanied by a large scattered radiation background, due to the rough surface topography of many thin films. In order to address these issues the PLE measurements are performed with a LED based setup as shown in Fig. 6.1 and Fig. 6.2(a). In this setup, a tunable LED source [124] provides a bright light output, which is then collimated and focused onto the entrance grating in order to tune the bandwidth of the source (~15 nm) near the peak intensity wavelengths. This light is then split into two components with a periscope structure, where one part is used to monitor the incident photon flux and the other part is focused on the sample. PL excited by the incident light is then collimated and focused onto the exit grating, which is positioned to select the band-edge PL radiation while rejecting the incident light scattered from the sample. The PL signal is then passed through a long pass filter to further ensure the incident light rejection. Finally, the PL is focused on a high gain Si detector connected to a lock-in amplifier. The modulation in the LED light intensity required for the lock-in detection is achieved by driving the LED with an AC signal controlled by the lock-in amplifier. Details regarding the instrumentation setup and calibration will be published elsewhere.

Although we measured InP samples in this work, this PLE setup is can be applied to other materials. In Fig. 6.2(b), the PLE setup has been used to measure an unpassivated GaAs wafer, where strong suppression of the PLE signal at short wavelength region is observed. This is likely due to the unpassivated GaAs wafer having a very high surface recombination. In addition, a higher quality GaAs thin film double-hetero structure has also been investigated using this PLE setup [125].

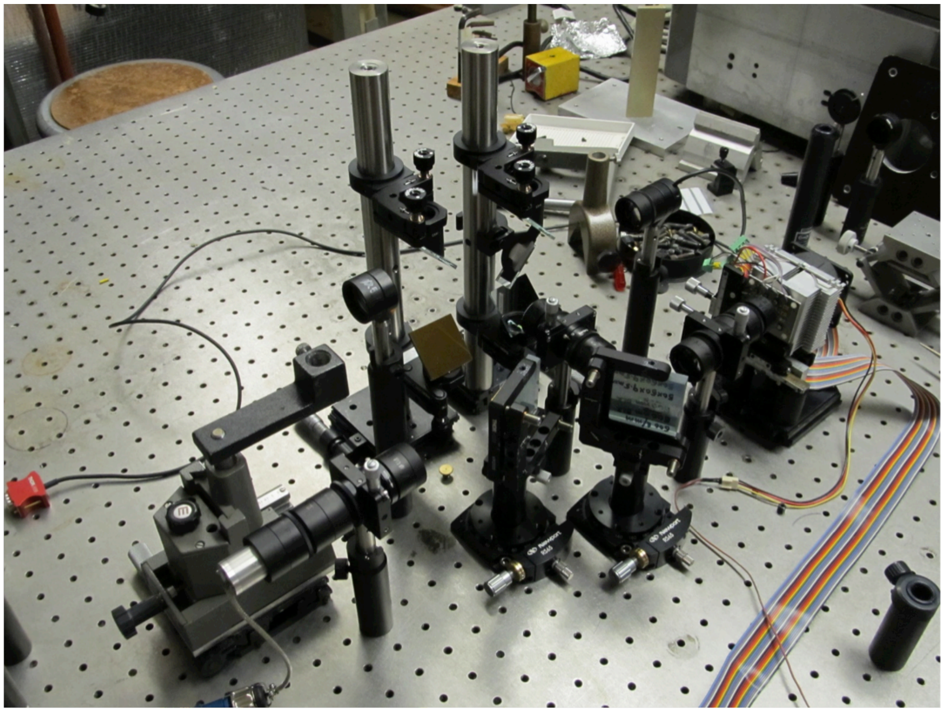

Fig. 6.1. Picture of the PLE setup used in this study. Several electrical components including the LED driver unit, lock-in amplifier, and controlling PC are not captured in this picture.

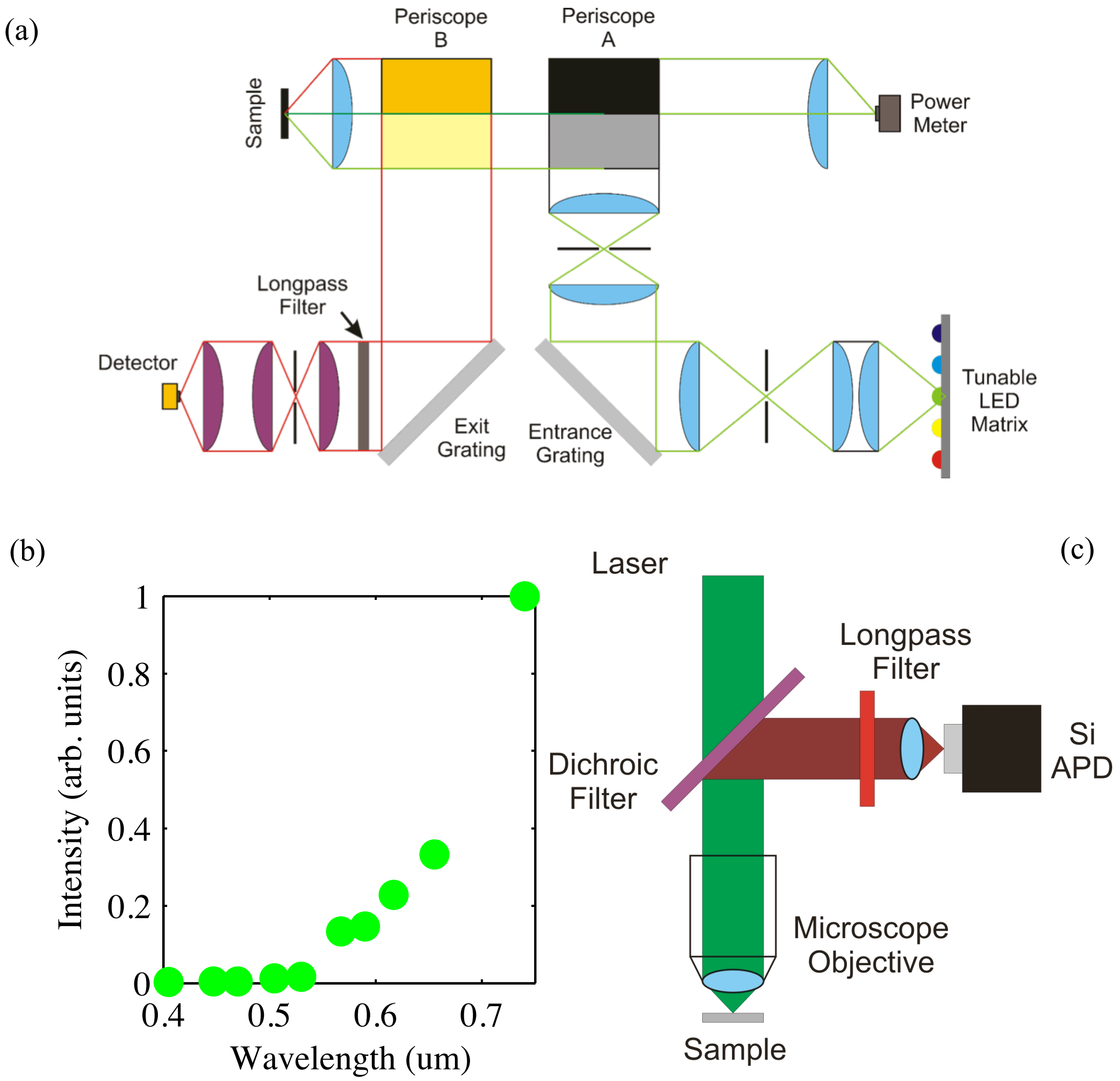

Fig. 6.2. (a) Layout for the PLE experimental setup used in this study. The measurement event starts at the tunable LED matrix at the lower right corner. The sample under testing is at the upper left corner, and the PLE emission signal is detected at the lower left corner. (b) PLE for an unpassivated GaAs wafer. (c) The TCSPC TRPL experimental setup used in this study.

The TRPL measurements were conducted using a standard confocal microscope based Time-Correlated Single Photon Counting (TCSPC) setup [152] shown in Fig. 6.2(c). In this setup a 550 nm pulsed laser is focused on the sample with a microscope objective. The PL collected by the objective is then passed through a dichroic filter to reject the laser light from the PL radiation. A long pass filter further ensures reliable PL signal for detection. The PL photons are detected with a Si Avalanche Photo Diode (Si-APD) in order to perform the time correlated photon counting.

6.3.2 Simulation Setup

Since the techniques used here are both based on PL, a correct model of PL emission is critical for proper analysis of the results. A simple integration of radiative recombination as emission, as commonly seen in literature, can be inaccurate and inadequate due to the structural dependence of emission caused by photon recycling. Instead, we opt to: 1) calculate a structure-independent intrinsic radiative recombination rate, and 2) use ray-tracing to calculate the amount of radiative emission that is reabsorbed (recycled) or that escapes as the PL signal. The approach is similar to the one used by Durbin *et al.* [56, 67].

Radiative recombination is an intrinsic property of any material at a finite temperature, and it is related to the absorption coefficient by the Roosbroeck-Shockley equation. Away from equilibrium the quasi-Fermi levels split, so that:

$$R_{emit}(V) = R_{emit}(V = 0)e^{qV/kT} \tag{5.6}$$

Based on this idea, we upgraded an existing electro-optically coupled simulation framework based on Sentaurus™ to simulate PL based characterization [93]. As a result, the photon recycling is taken into account and the various radiative loss components are resolved. For more details on this electro-optically coupled simulation framework, readers are referred to Refs. [93] and [113], where this framework has been successfully used to investigate single-junction GaAs solar cells and nanowire solar cells.

6.4 TRPL & PLE Sensitivity

Although both TRPL and PLE measurements are influenced by surface and bulk recombination, their sensitivities to each mechanism vary. To illustrate this idea, we simulate and compare the TRPL and PLE for a 3-μm thick InP thin film. Fig. 6.3(a) shows the TRPL with 28 ns bulk SRH lifetime (τ_{SRH}) for various front surface recombination velocities (S_{front}). The surface only affects the PL decay rate during the first few nanoseconds. Using $S_{\mathrm{front}} = 5\mathrm{x}10^4$ cm/s and $\tau_{\mathrm{SRH}} = 12$ ns for example, the time-dependent recombination rates are shown in Fig. 6.4(a). During the initial few nanoseconds, the newly generated electron-hole pairs have not yet diffused far away from the front surface, so front surface recombination dominates the PL decay. As the carriers diffuse toward the back, most of the recombination occurs in the bulk, and the decay rate becomes dominated by the bulk SRH lifetime. Ideally, S_{front} can be extracted through a double-exponential fit to the TRPL data, but it is often not feasible in practice due to factors such as injection-level and carrier mobility, or experimental factors such as instrument response time. As a result, TRPL-based estimates of surface recombination velocity have significant uncertainty.

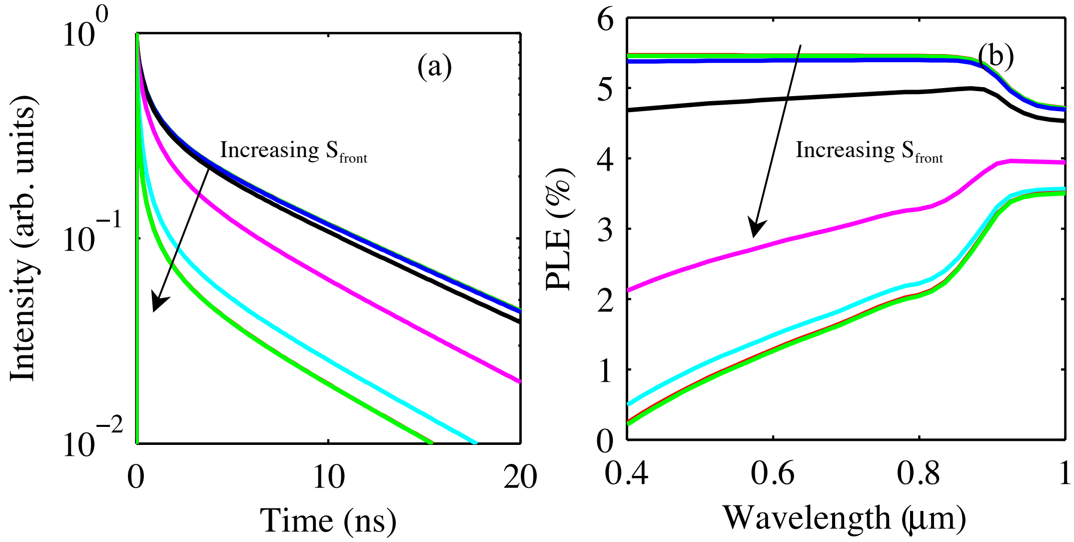

Fig. 6.3. Numerical simulations demonstrate that: (a) TRPL and (b) PLE show greatly differing responses to variations in surface recombination velocity over the range $S_{\mathrm{front}} =$ 1, 10, 10^2, 10^3, 10^4, 10^5, 10^6, and 10^7 cm/s at $\tau_{\mathrm{SRH}} = 28$ ns. PLE-based estimates of S_{front} generally have much smaller errors.

In contrast to TRPL, PLE displays a clear, predictable dependency on S_{front} in Fig. 6.3(b). Due to the change of absorption coefficient, the generation profile of carriers varies across different wavelengths. Fig. 6.4(b) displays the recombination components versus wavelength for $S_{front} = 10^4$ cm/s. As the centroid of generation moves away from the front surface, the impact of front surface recombination decreases, and the external fluorescence efficiency increases as a result.

Because of these effects, PLE can be interpreted as an "open-circuit" version of the external quantum efficiency (EQE) measurement [109]. Both PLE and EQE are steady-state measurements using incident light sources as a function of wavelengths. Instead of detecting the short-circuit current as in EQE, PLE measures the radiative emission under open-circuit condition. The presence of surface recombination decreases the current collected in EQE, and in the case of PLE, it decreases the amount of free carriers recombining radiatively. In fact, it has been shown that, in a high quality sample, the EQE and PLE are closely related [125].

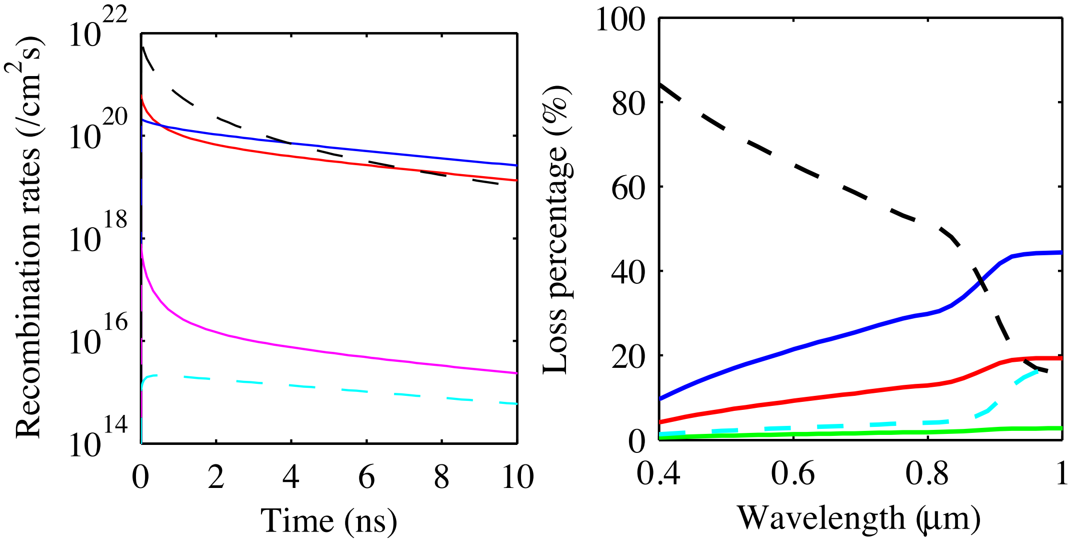

Fig. 6.4. Internal loss components predicted for (a) TRPL vs. time and (b) PLE vs. wavelength at $S_{front} = 5\text{x}10^4$ cm/s and $\tau_{SRH} = 12$ ns. These specific parameters are chosen since they provide the best overall fit to the InP sample tested, as shown in Fig. 6.7.

Consider next the sensitivity of these techniques to bulk lifetime. For a fixed S_{front} = 10^4 cm/s, both TRPL and PLE display sensitivity to a change in the bulk SRH lifetime, as shown in Fig. 6.5(a) and (b) respectively. In practice, however, the variation in PLE observed in Fig. 6.5(b) may be difficult to observe, since the absolute measurement of PLE can be difficult, and the less than 1% difference in values can easily be washed out by noise.

To summarize, TRPL is more sensitive to bulk properties, particularly when the surface is well passivated, while the extraction of surface information is much more robust in PLE. The two techniques nicely compliment each other, and both involve complicated internal physics that require electro-optically coupled simulation to self-consistently resolve.

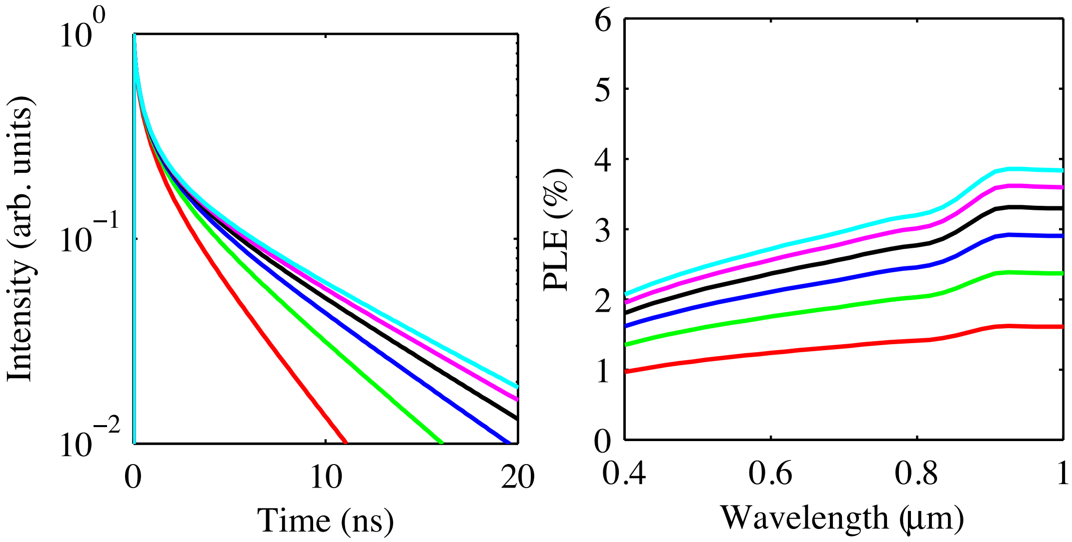

Fig. 6.5. (a) TRPL and (b) PLE for τ_{SRH} = 5, 9, 13, 17, 21, and 25 ns at S_{front} = 10^4 cm/s.

6.5 Results and Analysis

6.5.1 VLS-grown InP Thin Film

Recently, InP thin films have been grown via a novel VLS growth method [153]. The large grain size and good uniformity make it a promising technique for low-cost InP thin film photovoltaics. In this section, the proposed TRPL and PLE coupled approach is applied to these InP thin films in order to derive quantitative information regarding surface and bulk recombination.

TRPL and PLE for various S_{front} and SRH lifetimes are simulated using the electro-optically coupled simulator, and compared to the measured curves. The maps of least-square fitting errors for TRPL and PLE as a function of Shockley-Read-Hall (SRH) bulk lifetime and surface recombination velocity S_{front} are displayed in Fig. 6.6(a) and (b), respectively. The heightened sensitivity of TRPL to bulk properties, and PLE to surface properties, can be clearly seen as stronger gradients in those directions. By minimizing the overall error between both of our measurements and simulations, we find S_{front} = 5×10^4 cm/s and τ_{SRH} = 12 ns represents our best estimate of the overall material properties. While the precision of this estimate of each property is fairly good, to within several percent, estimating the absolute accuracy would require an independent measurement.

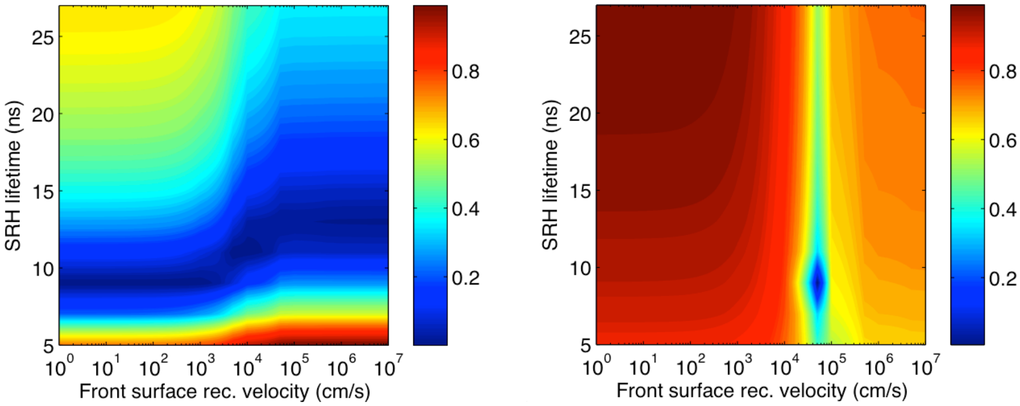

Fig. 6.6. VLS-grown InP thin film: least-square error map as a function of SRH lifetime and front surface recombination velocity when fitting to simulations of (a) TRPL and (b) PLE. The least-square error units are arbitrary, with cold blue regions indicating smaller error and best fit, with hot red regions being the opposite.

Fig. 6.7(a) and (b) respectively show the simulated TRPL and PLE curve for the estimated material parameters compared to the measured data. Both display a good overall match. The only deviation is in TRPL within the first 2 ns, when the surface recombination dominates. In practice, TRPL curves often do not display such sharp features due to lagged instrument response artificially prolonging the delay and adding noise. A convolution of simulated TRPL with the instrument response function (IRF) should further improve agreement over the first few nanoseconds.

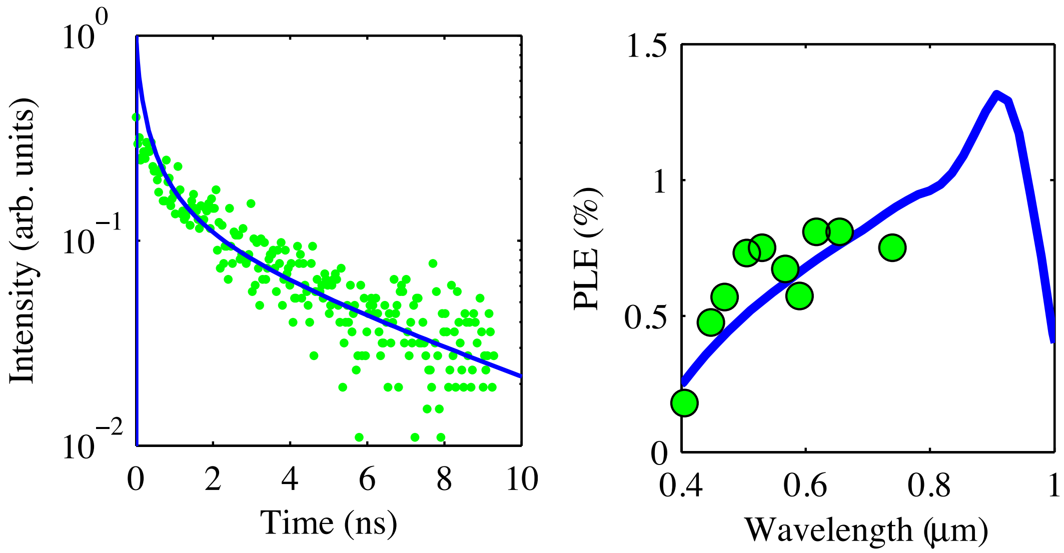

Fig. 6.7. Best overall fit for (a) TRPL and (b) PLE. Simulations are solid blue curves, and measurements are green dots.

6.5.2 InP Substrate

For comparison, an n-type ($5x10^{17}$ /cm^3) InP wafer of 250 mm thickness is also analyzed. The maps of least-square fitting errors for TRPL and PLE as a function of Shockley-Read-Hall (SRH) bulk lifetime and surface recombination velocity S_{front} are displayed in Fig. 6.8(a) and (b), respectively. Overall, $S_{\mathrm{front}} = 2x10^4$ cm/s and $\tau_{\mathrm{SRH}} = 0.2$ ns give the best fitting for the InP wafer. Compared to the VLS-grown InP thin film sample, the wafer has significantly lower bulk SRH lifetime, which is expected in this sample. The surface for the wafer is unpassivated and the same as the VLS-grown InP thin film, thus the derived surface recombination velocities are similar in both cases.

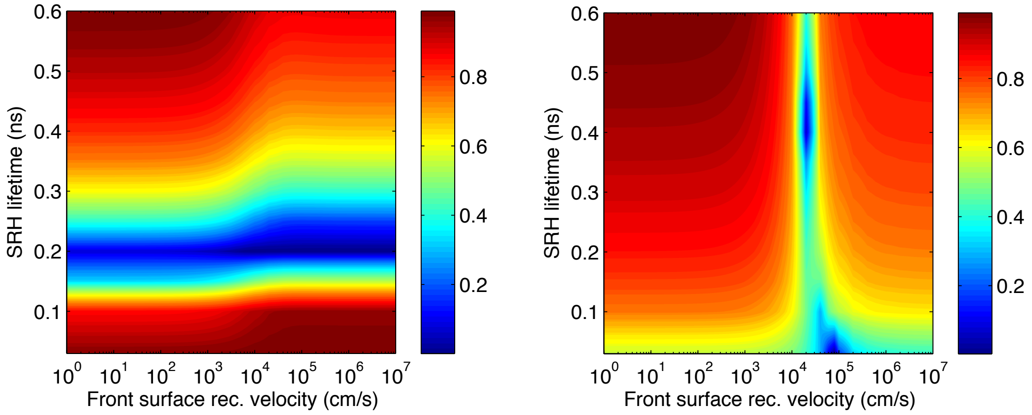

Fig. 6.8. InP wafer: Least-square error map as a function of SRH lifetime and front surface recombination velocity when fitting to simulations of (a) TRPL and (b) PLE. The least-square error units are arbitrary, with cold blue regions indicating smaller error and best fit, with hot red regions being the opposite.

6.6 Summary

In this study, we demonstrated that combining TRPL and steady-state PLE experiments with multi-physics simulation techniques yields a precise, contactless inline characterization method for photovoltaic materials. Differences in sensitivity to various loss mechanisms make TRPL and PLE more suitable for measuring bulk and surface recombination, respectively, particularly for well-passivated front surfaces. With a rigorous electro-optically coupled simulator properly modeling PL emission, we show quantitative bulk lifetime and surface recombination velocity can be extracted self-consistently. The method is applied to a novel VLS-grown InP thin film, and we find S_{front} = 5x10^4 cm/s and τ_{SRH} = 12 ns gives the best match between our simulation and experiments. The precision of the combined approach appears to be good, but the accuracy should be assessed using an independent measurement technique. We believe the method in this work is general enough to be applied to other materials and to be used as an inline method for quantitative process monitoring.

7 CONCLUSIONS AND FUTURE WORK

7.1 Conclusions

As solar cells continue in reaching higher efficiencies, it may be only a matter of time before many of them eventually overcome practical obstacles and approach their Shockley-Queisser limits. Near the Shockley-Queisser limit, the radiative recombination is the dominant loss mechanism, which turns the entire design and optimization of solar cells into a nontrivial, electro-optically coupled problem. The traditional approach of treating the radiative recombination using an effective B coefficient that is independent of dielectric structure or position is not suitable near the Shockley-Queisser limit. The radiative recombination must be modeled optically to accurately calculate the intrinsic emission and photon recycling.

The thesis first develops an electro-optically coupled simulation framework for the purpose of correctly resolving radiative recombination in a thermodynamically sound way. It is applied to the design and characterization of various solar cells near the Shockley-Queisser limit. This thesis was dedicated to the study of this problem. In terms of solar cell design, three different high-efficiency designs are investigated: 1) a world-record thin-film GaAs solar cell, 2) a single nanowire solar cell, and 3) a world-record GaInP/GaAs tandem solar cell.

The thin-film GaAs solar has a rather simple, layered structure that can be treated using ray-optics. Chapter 2 demonstrates that, with detailed electro-optically coupled simulation and careful calibration of material parameters, the numerical simulation can precisely reproduce experiments, suggesting areas where new designs can focus to improve efficiency. The single nanowire solar cell represents a breed of novel solar cell designs, including the likes of plasmonic solar cells and quantum dot solar cells, which integrate the electrical and optical structures together at the nanoscale. The electro-optically coupled approach automatically takes care of the integrated structure, and takes into account the nanoscale features of the nanowires, where the radiative recombination is treated using wave optics. For the GaInP/GaAs tandem solar cell, the electro-optically coupled simulator is able to consider both the top and bottom cells in one self-consistent simulation. Therefore, important physical phenomena such as luminescence couplings and current matching are taken into account. Overall, this work has demonstrated that the electro-optically coupled approach proposed in this thesis is versatile and comprehensive enough to tackle a wide range of solar cell design problems.

In terms of characterization, studies are conducted on two topics: 1) the reciprocity theorem of solar cells, and 2) the quantitative material parameter extraction from TRPL/PLE. In the first work, the electro-optically coupled simulator is used to verify the validity of the reciprocity theorem, which links the EQE with the ERE of the solar cells. The simulator faithfully solves the semiconductor equations without the assumptions embedded in the reciprocity theorem as an independent test. It is found that the superposition principle must be obeyed for the reciprocity theorem to hold. In the second topic, it is shown that the same simulator can also be coupled with TRPL/PLE experiments to extract lifetime parameters from photovoltaic materials in a self-consistent manner. Due to the nature of being transient and steady-state, respectively, TRPL and PLE are much more sensitive to bulk and surface recombination, respectively. Coupling these two techniques with the electro-optically coupled simulator allows one to fit and extract quantitative lifetime parameters.

7.2 Future work

7.2.1 Nanowire array design and optimization

In Chapter 3, a single nanowire solar cell is studied. To use nanowire as a variable way of collecting sunlight, however, an array of nanowires must be used. In this case, many design parameters including the diameter of the nanowires, the packing geometry, the spacing between neighboring nanowires, and the height must be considered. Using the electro-optically coupled approach with wave optics, it would be interesting to see how the overall efficiency of the nanowire array compare to that of a single nanowire. Furthermore, it would be important to redesign it for improved performance.

Using the present electro-optically coupled simulator in Sentaurus™ can solve this problem, but it would be time consuming. The majority of the calculation time is spent in the FDTD simulation of intrinsic emission and photon recycling. This time-consuming step prevents one from investigating the many combinations of critical design parameters mentioned above.

One way around this problem is to replace the FDTD module with a frequency domain simulator such as S4 [154]. S4 at present is unable to include an arbitrary dipole source. However future development on the code would enable a faster wave-optics module for the electro-optically coupled simulator. Otherwise, an independently deployed S-matrix code would provide appropriate functionality.

7.2.2 Tandem solar cell optimization and characterization

In Chapter 4, the GaInP/GaAs tandem solar cell is investigated without optimizing its geometry. The first opportunity for future work is to optimize its structure while taking into account luminescent coupling and current matching. This includes optimizing the subcell thickness, junction positions, and material bandgaps. The scope shall also be expanded to other III-V material systems and to triple-junction devices.

A second opportunity is the characterization of tandem solar cells. One key difficulty in characterizing tandem solar cells is to separate the effects of the individual junctions. Moreover, since the subcells are connected in series, techniques depending on current, such as EQE, become nontrivial. For example, to obtain the overall EQE for the tandem cell, all junctions except the junction under test must be over-illuminated using a bias light.

Luminescence based techniques such as PLE can potentially bypass the current matching problems in EQE. However, luminescence couplings can become non-trivial. Thus, the combination of PLE with electro-optically coupled approach is a promising method of characterizing the tandem solar cell.

7.2.3 Novel junction designs and optimization

High quality materials relax many constraints on the solar cell design, allowing unconventional structures to be used for efficient current extraction. The interdigitized back contact (IBC) cell is a successful example of such design. Taking advantage of the long lifetime of crystalline silicon, one can readily move the junction and both contacts to the back of the solar cell to eliminate shadowing losses. The electro-optically coupled simulator gives one the opportunity to explore novel junction designs to facilitate better light trapping and photon recycling.

LIST OF REFERENCES

LIST OF REFERENCES

[1] K. H. Solangi, M. R. Islam, R. Saidur, N. A. Rahim, and H. Fayaz, "A review on global solar energy policy," *Renewable and Sustainable Energy Reviews,* vol. 15, pp. 2149-2163, 2011.

[2] S. Mekhilef, R. Saidur, and A. Safari, "A review on solar energy use in industries," *Renewable and Sustainable Energy Reviews,* vol. 15, pp. 1777-1790, 2011.

[3] T. M. Razykov, C. S. Ferekides, D. Morel, E. Stefanakos, H. S. Ullal, and H. M. Upadhyaya, "Solar photovoltaic electricity: Current status and future prospects," *Solar Energy,* vol. 85, pp. 1580-1608, 2011.

[4] F. Dinçer, "The analysis on photovoltaic electricity generation status, potential and policies of the leading countries in solar energy," *Renewable and Sustainable Energy Reviews,* vol. 15, pp. 713-720, 2011.

[5] G. R. Timilsina, L. Kurdgelashvili, and P. A. Narbel, "Solar energy: Markets, economics and policies," *Renewable and Sustainable Energy Reviews,* vol. 16, pp. 449-465, 2012.

[6] J. Nelson, *The Physics of Solar Cells* vol. 50: Imperial College Press, 2003.

[7] B. M. Kayes, H. Nie, R. Twist, S. G. Spruytte, F. Reinhardt, I. C. Kizilyalli*, et al.*, "27.6% Conversion efficiency, a new record for single-junction solar cells under 1 sun illumination," in *IEEE Phovoltaic Specialist Conference*, 2011, pp. 000004-000008.

[8] G. L. Pearson, "Conversion of Solar to Electrical Energy," *American Journal of Physics,* vol. 25, pp. 591-591, 1957.

[9] W. Shockley and H. J. Queisser, "Detailed Balance Limit of Efficiency of p-n Junction Solar Cells," *Journal of Applied Physics,* vol. 32, pp. 510-510, 1961.

[10] E. T. Yu and J. van de Lagemaat, "Photon management for photovoltaics," *MRS Bulletin,* vol. 36, pp. 424-428, 2011.

[11] D. M. Callahan, J. N. Munday, and H. A. Atwater, "Solar Cell light trapping beyond the ray optic limit," *Nano letters,* vol. 12, pp. 214-8, 2012.

[12] M. A. Green, K. Emery, Y. Hishikawa, W. Warta, and E. D. Dunlop, "Solar cell efficiency tables (version 44)," *Progress in Photovoltaics: Research and Applications,* vol. 22, pp. 701-710, 2014.

[13] A. de Vos, "Detailed balance limit of the efficiency of tandem solar cells," *Journal of Physics D: Applied Physics,* vol. 13, pp. 839-846, 1980.

[14] P. T. Landsberg and P. Baruch, "The thermodynamics of the conversion of radiation energy for photovoltaics," *Journal of Physics A: Mathematical and General,* vol. 22, pp. 1911-1926, 1989.

[15] M. R. Khan, P. Bermel, and M. A. Alam, "Thermodynamic Limits of Solar Cells with Non-ideal Optical Response," *2013 39th IEEE Photovoltaic Specialists Conference,* vol. 2, 2013.

[16] O. E. Semonin, J. M. Luther, S. Choi, H.-Y. Chen, J. Gao, A. J. Nozik*, et al.*, "Peak external photocurrent quantum efficiency exceeding 100% via MEG in a quantum dot solar cell," *Science (New York, N.Y.),* vol. 334, pp. 1530-3, 2011.

[17] D. König, K. Casalenuovo, Y. Takeda, G. Conibeer, J. F. Guillemoles, R. Patterson*, et al.*, "Hot carrier solar cells: Principles, materials and design," *Physica E: Low-dimensional Systems and Nanostructures,* vol. 42, pp. 2862-2866, 2010.

[18] A. Luque and A. Martí, "Increasing the efficiency of ideal solar cells by photon induced transitions at intermediate levels," *Physical Review Letters,* 1997.

[19] C. Honsberg and S. Bowden, "Anti-Reflection Coatings," ed.

[20] A. Wright, "Nature Photonics milestones," *Nature Photonics,* vol. 176, pp. 5-20, 2010.

[21] O. D. Miller, E. Yablonovitch, and S. R. Kurtz, "Strong Internal and External Luminescence as Solar Cells Approach the Shockley–Queisser Limit," *IEEE Journal of Photovoltaics,* vol. 2, pp. 303-311, 2012.

[22] D. M. Powell, M. T. Winkler, H. J. Choi, C. B. Simmons, D. B. Needleman, and T. Buonassisi, "Crystalline silicon photovoltaics: a cost analysis framework for determining technology pathways to reach baseload electricity costs," *Energy & Environmental Science,* vol. 5, pp. 5874-5874, 2012.

[23] J. Müller, B. Rech, J. Springer, and M. Vanecek, "TCO and light trapping in silicon thin film solar cells," *Solar Energy,* vol. 77, pp. 917-930, 2004.

[24] U. W. Paetzold, W. Zhang, M. Prömpers, J. Kirchhoff, T. Merdzhanova, S. Michard*, et al.*, "Thin-film silicon solar cell development on imprint-textured glass substrates," *Materials Science and Engineering: B,* vol. 178, pp. 617-622, 2013.

[25] "Shockley-Queisser limit and material bandgaps," ed.

[26] L. Rayleigh, "On the intensity of light reflected from certain surfaces at nearly perpendicular incidence," *Proceedings of the Royal Society of London,* vol. 41, pp. 275-294, 1886.

[27] W. L. Bailey, M. G. Coleman, C. B. Harris, and I. A. Lesk, "Texture etching of silicon: method," *US Patent 4,137,123,* 1979.

[28] E. Yablonovitch and G. D. Cody, "Intensity enhancement in textured optical sheets for solar cells," *IEEE Trans. Electron Devices,* vol. ED-29, pp. 300-305, 1982.

[29] C. J. R. Sheppard, "Approximate calculation of the reflection coefficient from a stratified medium," *Pure and Applied Optics: Journal of the European Optical Society Part A,* vol. 4, pp. 665-669, 1995.

[30] Y. Fink, J. N. Winn, S. Fan, C. Chen, J. Michel, J. D. Joannopoulos*, et al.*, "A Dielectric Omnidirectional Reflector," *Science,* vol. 282, pp. 1679-1682, 1998.

[31] P. Bermel, C. Luo, L. Zeng, L. C. Kimerling, and J. D. Joannopoulos, "Improving thin-film crystalline silicon solar cell efficiencies with photonic crystals," *Optics Express,* vol. 15, pp. 16986-17000, 2007.

[32] X. Wang and M. A. Alam, "Estimating pyramid density of a random-textured surface by capacitance-voltage measurement of c-Si solar cells," in *IEEE Photovoltaic Specialists Conference*, Tampa, FL, 2013, pp. 1-5.

[33] M. R. Khan, X. Wang, P. Bermel, and M. A. Alam, "Enhanced light trapping in solar cells with a meta-mirror following generalized Snell's law," *Opt Express,* vol. 22 Suppl 3, pp. A973-85, May 5 2014.

[34] A. Barnett, C. Honsberg, D. Kirkpatrick, S. Kurtz, D. Moore, D. Salzman*, et al.*, "50% Efficient Solar Cell Architectures and Designs," pp. 2560-2564.

[35] H. A. Atwater, M. D. Escarra, C. N. Eisler, E. D. Kosten, E. C. Warmann, S. Darbe*, et al.*, "Full Spectrum Ultrahigh Efficiency Photovoltaics," *2013 39th IEEE Photovoltaic Specialists Conference,* vol. 1, 2013.

[36] M. D. Escarra, S. Darbe, E. C. Warmann, and H. A. Atwater, "Spectrum-Splitting Photovoltaics : Holographic Spectrum Splitting in Eight-Junction, Ultra-high Efficiency Module," *2013 39th IEEE Photovoltaic Specialists Conference,* vol. 1, 2013.

[37] C. N. Eisler, E. D. Kosten, E. C. Warmann, H. A. Atwater, and J. Lloyd, "Spectrum Splitting Photovoltaics : Polyhedral Specular Reflector Design for Ultra-High Efficiency Modules," *2013 39th IEEE Photovoltaic Specialists Conference,* vol. 1, 2013.

[38] E. D. Kosten, J. Lloyd, E. Warmann, and H. A. Atwater, "Spectrum Splitting Photovoltaics : Light Trapping Filtered Concentrator for Ultrahigh Photovoltaic Efficiency," *2013 39th IEEE Photovoltaic Specialists Conference,* vol. 1, 2013.

[39] X. Ni, N. K. Emani, A. V. Kildishev, A. Boltasseva, and V. M. Shalaev, "Broadband light bending with plasmonic nanoantennas," *Science (New York, N.Y.),* vol. 335, pp. 427-427, 2012.

[40] N. Yu, P. Genevet, M. a. Kats, F. Aieta, J.-P. Tetienne, F. Capasso*, et al.*, "Light propagation with phase discontinuities: generalized laws of reflection and refraction," *Science (New York, N.Y.),* vol. 334, pp. 333-7, 2011.

[41] T.-H. Her, R. J. Finlay, C. Wu, S. Deliwala, and E. Mazur, "Microstructuring of silicon with femtosecond laser pulses," *Applied Physics Letters,* vol. 73, pp. 1673-1673, 1998.

[42] J. Zhu, Z. Yu, G. F. Burkhard, C. M. Hsu, S. T. Connor, Y. Xu*, et al.*, "Optical absorption enhancement in amorphous silicon nanowire and nanocone arrays," *Nano Lett,* vol. 9, pp. 279-82, Jan 2009.

[43] P. Krogstrup, H. I. Jørgensen, M. Heiss, O. Demichel, J. V. Holm, M. Aagesen*, et al.*, "Single-nanowire solar cells beyond the Shockley–Queisser limit," *Nature Photonics,* vol. 7, pp. 306-310, 2013.

[44] B. Tian, T. J. Kempa, and C. M. Lieber, "Single nanowire photovoltaics," *Chemical Society Reviews,* vol. 38, pp. 16-24, 2009.

[45] H. C. Casey and E. Buehler, "Evidence for low surface recombination velocity on n-type InP," *Applied Physics Letters,* vol. 30, pp. 247-247, 1977.

[46] J. Wallentin, N. Anttu, D. Asoli, M. Huffman, I. Aberg, M. H. Magnusson*, et al.*, "InP nanowire array solar cells achieving 13.8% efficiency by exceeding the ray optics limit," *Science (New York, N.Y.),* vol. 339, pp. 1057-60, 2013.

[47] J. M. Woodall, "Photoluminescent properties of GaAs–GaAlAs, GaAs–oxide, and GaAs–ZnS heterojunctions," *Journal of Vacuum Science and Technology,* vol. 16, pp. 1389-1389, 1979.

[48] G. Lush and M. Lundstrom, "Thin film approaches for high-efficiency III-V cells," *Solar cells,* vol. 30, pp. 337-344, 1991.

[49] I. Schnitzer, E. Yablonovitch, C. Caneau, and T. J. Gmitter, "Ultrahigh spontaneous emission quantum efficiency, 99.7% internally and 72% externally, from AlGaAs/GaAs/AlGaAs double heterostructures," *Applied Physics Letters,* vol. 62, pp. 131-131, 1993.

[50] E. Yablonovitch, O. D. Miller, and S. R. Kurtz, "A Great Solar Cell also Needs to be a Great LED: External Fluorescence Leads to New Efficiency Record," *Nobel Symposium 153: Nanoscale Energy Converters,* vol. 1519, pp. 9-11, 2013.

[51] H. A. Atwater, "Paths to high efficiency low-cost photovoltaics," *2011 37th IEEE Photovoltaic Specialists Conference,* pp. 000001-000003, 2011.

[52] W. van Roosbroeck and W. Shockley, "Photon-Radiative Recombination of Electrons and Holes in Germanium," *Physical Review,* vol. 94, pp. 1558-1560, 1954.

[53] A. Martí, J. L. Balenzategui, and R. F. Reyna, "Photon recycling and Shockley's diode equation," *Journal of Applied Physics,* vol. 82, pp. 4067-4067, 1997.

[54] F. Urbach, "The Long-Wavelength edge of photographic sensitivity and of the electronic absorption of solids," *Physical Review,* pp. 61-61, 1953.

[55] E. Yablonovitch, "Statistical ray optics," *Journal of the Optical Society of America,* vol. 72, p. 899, 1982.

[56] S. M. Durbin, J. L. Gray, R. K. Ahrenkiel, and D. H. Levi, "Numerical modeling of the influence of photon recycling on lifetime measurements," in *IEEE Phovoltaic Specialists Conference*, 1993, pp. 628-632.

[57] J. L. Gray, X. Wang, X. Sun, and J. R. Wilcox, "ADEPT 2.0," ed, 2013.

[58] M. A. Green and K. Emery, "Solar cell efficiency tables (version 42)," *Progress in Photovoltaics: Research and Applications,* vol. 21, pp. 827-837, 2013.

[59] G. J. Bauhuis, P. Mulder, E. J. Haverkamp, J. C. C. M. Huijben, and J. J. Schermer, "26.1% thin-film GaAs solar cell using epitaxial lift-off," *Solar Energy Materials and Solar Cells,* vol. 93, pp. 1488-1491, 2009.

[60] J. E. Parrott, "Radiative recombination and photon recycling in photovoltaic solar cells," *Solar Energy Materials and Solar Cells,* vol. 30, pp. 221-231, 1993.

[61] F. Stern and J. M. Woodall, "Photon recycling in semiconductor lasers," *Journal of Applied Physics,* vol. 45, pp. 3904-3904, 1974.

[62] J. Gray, "the physics of solar cells," in *handbook of photovoltaic science and engineering*, ed: John Wiley & Sons, 2011.

[63] P. Asbeck, "Self-absorption effects on the radiative lifetime in GaAs-GaAlAs double heterostructures," *Journal of Applied Physics,* vol. 48, p. 820, 1977.

[64] G. B. Lush, "B-coefficient in n-type GaAs," *Solar Energy Materials and Solar Cells,* vol. 93, pp. 1225-1229, 2009.

[65] Y. P. Varshni, "Band-to-Band Radiative Recombination in Groups IV, VI, and III-V Semiconductors (I)," *physica status solidi (b),* vol. 19, pp. 459-514, 1967.

[66] H. C. Casey, "Concentration-dependent absorption and spontaneous emission of heavily doped GaAs," *Journal of Applied Physics,* vol. 47, p. 631, 1976.

[67] S. M. Durbin and J. L. Gray, "Numerical modeling of photon recycling in solar cells," *IEEE Transactions on Electron Devices,* vol. 41, pp. 239-245, 1994.

[68] T. Yagi, Y. Uraoka, and T. Fuyuki, "Ray-trace simulation of light trapping in silicon solar cell with texture structures," *Solar Energy Materials and Solar Cells,* vol. 90, pp. 2647-2656, 2006.

[69] P. D. DeMoulin, S. P. Tobin, M. S. Lundstrom, M. S. Carpenter, and M. R. Melloch, "Influence of perimeter recombination on high-efficiency GaAs p/n heteroface solar cells," *IEEE Electron Device Letters,* vol. 9, pp. 368-370, 1988.

[70] R. T. Ross, "Some Thermodynamics of Photochemical Systems," *The Journal of Chemical Physics,* vol. 46, p. 4590, 1967.

[71] L. Wen, L. Yueqiang, C. Jianjun, C. Yanling, W. Xiaodong, and Y. Fuhua, "Optimization of grid design for solar cells," *Journal of Semiconductors,* vol. 31, p. 014006, 2010.

[72] L. S. Mattos, S. R. Scully, M. Syfu, E. Olson, L. Yang, C. Ling*, et al.*, "New module efficiency record: 23.5% under 1-sun illumination using thin-film single-junction GaAs solar cells," pp. 003187-003190, 2012.

[73] M. A. Green, "Third generation photovoltaics: Ultra-high conversion efficiency at low cost," *Progress in Photovoltaics: Research and Applications,* vol. 9, pp. 123-135, 2001.

[74] L. Cao, P. Fan, A. P. Vasudev, J. S. White, Z. Yu, W. Cai*, et al.*, "Semiconductor nanowire optical antenna solar absorbers," *Nano letters,* vol. 10, pp. 439-45, 2010.

[75] M. D. Kelzenberg, D. B. Turner-Evans, B. M. Kayes, M. A. Filler, M. C. Putnam, N. S. Lewis*, et al.*, "Single-nanowire Si solar cells," in *IEEE Photovoltaic Specialist Conference*, 2008, pp. 1-6.

[76] E. C. Garnett and P. Yang, "Silicon nanowire radial p-n junction solar cells," *Journal of the American Chemical Society,* vol. 130, pp. 9224-5, 2008.

[77] E. C. Garnett, M. L. Brongersma, Y. Cui, and M. D. McGehee, "Nanowire Solar Cells," *Annual Review of Materials Research,* vol. 41, pp. 269-295, 2011.

[78] B. M. Kayes, H. A. Atwater, and N. S. Lewis, "Comparison of the device physics principles of planar and radial p-n junction nanorod solar cells," *Journal of Applied Physics,* vol. 97, pp. 114302-114302, 2005.

[79] E. C. Garnett, C. Peters, M. Brongersma, Y. Cui, and M. McGehee, "Silicon nanowire hybrid photovoltaics," in *2010 35th IEEE Photovoltaic Specialists Conference*, 2010, pp. 000934-000938.

[80] M. M. Adachi, M. P. Anantram, and K. S. Karim, "Core-shell silicon nanowire solar cells," *Scientific reports,* vol. 3, pp. 1546-1546, 2013.

[81] X. Wang, M. R. Khan, M. A. Alam, and M. Lundstrom, "Approaching the Shockley-Queisser limit in GaAs solar cells," in *IEEE Photovoltaic Specialists Conference*, 2012, pp. 002117-002121.

[82] U. Rau, "Superposition and Reciprocity in the Electroluminescence and Photoluminescence of Solar Cells," *Ieee Journal of Photovoltaics,* vol. 2, pp. 169-172, Apr 2012.

[83] X. Wang and M. S. Lundstrom, "On the Use of Rau's Reciprocity to Deduce External Radiative Efficiency in Solar Cells," *IEEE Journal of Photovoltaics,* pp. 1-6, 2013.

[84] A. David, "High efficiency GaN-based LEDs: light extraction by photonic crystals," *Annales de Physique,* vol. 31, pp. 1-235, 2007.

[85] E. Yablonovitch, "Inhibited Spontaneous Emission in Solid-State Physics and Electronics," *Physical Review Letters,* vol. 58, pp. 2059-2062, 1987.

[86] S. C. H. Allen Taflove, *Computational Electrodynamics*: Artech House, 2005.

[87] A. F. Oskooi, D. Roundy, M. Ibanescu, P. Bermel, J. D. D. Joannopoulos, and S. G. Johnson, "Meep: A flexible free-software package for electromagnetic simulations by the FDTD method," *Computer Physics Communications,* vol. 181, pp. 687-702, 2010.

[88] M. Bass, C. DeCusatis, J. Enoch, V. Lakshminarayanan, G. Li, C. MacDonald*, et al.*, *Handbook of Optics, Third Edition Volume IV: Optical Properties of Materials, Nonlinear Optics, Quantum Optics (set)*: Mcgraw-hill, 2009.

[89] Synopsys Sentaurus Semiconductor TCAD Software

[90] R. Pierret, *Semiconductor device fundamentals*: Addison-Wesley Publishing Company, 1996.

[91] J. Zhao and M. A. Green, "Optimized antireflection coatings for high-efficiency silicon solar cells," *IEEE Transactions on Electron Devices,* vol. 38, pp. 1925-1934, 1991.

[92] D. N. Wright, E. S. Marstein, and A. Holt, "Double layer anti-reflective coatings for silicon solar cells," in *IEEE Photovoltaic Specialists Conference*, 2005, pp. 1237-1240.

[93] X. Wang, M. R. Khan, J. L. Gray, M. A. Alam, and M. S. Lundstrom, "Design of GaAs Solar Cells Operating Close to the Shockley–Queisser Limit," *IEEE Journal of Photovoltaics,* vol. 3, pp. 737-744, 2013.

[94] J. Moore, C. J. Hages, N. Carter, R. Agrawal, M. Lundstrom, and W. Lafayette, "The Physics of V bi -Related IV Crossover in Thin Film Solar Cells : Applications to Ink Deposited CZTSSe," in *IEEE Photovoltaic Specialists Conference*, 2013.

[95] S. H. Demtsu and J. R. Sites, "Effect of back-contact barrier on thin-film CdTe solar cells," *Thin Solid Films,* vol. 510, pp. 320-324, 2006.

[96] "NREL Reports 31.1% Efficiency for III-V Solar Cell-Conversion-efficiency mark is a world record for a two-junction solar cell measured under one-sun illumination," ed. NREL News, 2013.

[97] Bandgap Optimizer for Spectral Splitting PV Systems nanoHUB, 2014, https://nanohub.org/resources/19193

[98] K. C. Charles, J. R. Wilcox, and J. L. Gray, "Optimization Tool for Multijunction Photovoltaic Systems," in *40th IEEE Photovoltaic Specialists Conference*, Denver, CO, 2014.

[99] S. Kurtz, D. Myers, W. E. McMahon, J. Geisz, and M. Steiner, "A comparison of theoretical efficiencies of multi-junction concentrator solar cells," *Progress in Photovoltaics: Research and Applications,* vol. 16, pp. 537-546, 2008.

[100] M. A. Green, "Thin-film solar cells: review of materials, technologies and commercial status," *Journal of Materials Science: Materials in Electronics,* vol. 18, pp. 15-19, 2007.

[101] S. Kurtz and J. Geisz, "Multijunction solar cells for conversion of concentrated sunlight to electricity," *Optics Express,* vol. 18, pp. A73-A78, 2010/04/26 2010.

[102] J. F. Wheeldon, C. E. Valdivia, A. W. Walker, G. Kolhatkar, A. Jaouad, A. Turala*, et al.*, "Performance comparison of AlGaAs, GaAs and InGaP tunnel junctions for concentrated multijunction solar cells," *Progress in Photovoltaics: Research and Applications,* vol. 19, pp. 442-452, 2011.

[103] M. Yamaguchi, T. Takamoto, K. Araki, and N. Ekins-Daukes, "Multi-junction III–V solar cells: current status and future potential," *Solar Energy,* vol. 79, pp. 78-85, 2005.

[104] M. Meusel, R. Adelhelm, F. Dimroth, A. W. Bett, and W. Warta, "Spectral mismatch correction and spectrometric characterization of monolithic III-V multi-junction solar cells," *Progress in Photovoltaics: Research and Applications,* vol. 10, pp. 243-255, 2002.

[105] M. A. Steiner, J. F. Geisz, I. García, D. J. Friedman, A. Duda, W. J. Olavarria*, et al.*, "Effects of internal luminescence and internal optics on the V oc and J sc of III-V solar cells," *IEEE Photovolt. Spec. Conf.,* 2013.

[106] M. A. Steiner, J. F. Geisz, T. E. Moriarty, R. M. France, W. E. McMahon, J. M. Olson*, et al.*, "Measuring IV Curves and Subcell Photocurrents in the Presence of Luminescent Coupling," *Ieee Journal of Photovoltaics,* vol. 3, pp. 879-887, Apr 2013.

[107] J. F. Geisz, M. A. Steiner, I. García, S. R. Kurtz, and D. J. Friedman, "Enhanced external radiative efficiency for 20.8% efficient single-junction GaInP solar cells," *Applied Physics Letters,* vol. 103, p. 041118, 2013.

[108] E. Yablonovitch, T. Gmitter, and R. Bhat, "Inhibited and Enhanced Spontaneous Emission from Optically Thin AlGaAs/GaAs Double Heterostructures," *Physical Review Letters,* vol. 61, pp. 2546-2549, 1988.

[109] M. A. Green, "Radiative efficiency of state-of-the-art photovoltaic cells," *Progress in Photovoltaics: Research and Applications,* vol. 20, pp. 472-476, 2012.

[110] M. A. Steiner and J. F. Geisz, "Non-linear luminescent coupling in series-connected multijunction solar cells," *Applied Physics Letters,* vol. 100, p. 251106, Jun 18 2012.

[111] V. Ganapati, C.-S. Ho, and E. Yablonovitch, "Intermediate Mirrors to Reach Theoretical Efficiency Limits of Multi-Bandgap Solar Cells," *arXiv,* vol. 1406.3126 2014.

[112] A. Barnett, D. Kirkpatrick, C. Honsberg, D. Moore, M. Wanlass, K. Emery*, et al.*, "Very high efficiency solar cell modules," *Progress in Photovoltaics: Research and Applications,* vol. 17, pp. 75-83, 2009.

[113] X. Wang, M. R. Khan, M. Lundstrom, and P. Bermel, "Performance-limiting factors for GaAs-based single nanowire photovoltaics," *Optics Express,* vol. 22, p. A344, 2014.

[114] M. Hermle, G. Létay, S. P. Philipps, and A. W. Bett, "Numerical simulation of tunnel diodes for multi ‐ junction solar cells," *Progress in Photovoltaics: Research and Applications,* vol. 16, pp. 409-418, 2008.

[115] A. Kanevce, J. M. Olson, and W. K. Metzger, "Numerical simulations of triple-junction GaInP/GaAs/Ge solar cells to provide insight into fill-factor losses at high concentration," pp. 002066-002069, 2010.

[116] I. MeiKei, P. M. Solomon, S. E. Laux, H. S. P. Wong, and D. Chidambarrao, "Comparison of raised and Schottky source/drain MOSFETs using a novel tunneling contact model," in *Electron Devices Meeting, 1998. IEDM '98. Technical Digest., International*, 1998, pp. 733-736.

[117] K. A. Bertness, S. R. Kurtz, D. J. Friedman, A. E. Kibbler, C. Kramer, and J. M. Olson, "29.5%-efficient GaInP/GaAs tandem solar cells," *Applied Physics Letters,* vol. 65, p. 989, 1994.

[118] S. R. Kurtz, J. M. Olson, D. J. Friedman, J. F. Geisz, K. A. Bertness, and A. E. Kibbler, "Passivation of Interfaces in High-Efficiency Photovoltaic Devices," *MRS Proceedings,* vol. 573, 2011.

[119] S. H. Lim, J.-J. Li, E. H. Steenbergen, and Y.-H. Zhang, "Luminescence coupling effects on multijunction solar cell external quantum efficiency measurement," *Progress in Photovoltaics: Research and Applications,* vol. 21, pp. 344-350, 2013.

[120] T. Trupke, J. Zhao, A. Wang, R. Corkish, and M. a. Green, "Very efficient light emission from bulk crystalline silicon," *Applied Physics Letters,* vol. 82, pp. 2996-2996, 2003.

[121] T. Tiedje, E. Yablonovitch, G. D. Cody, and B. G. Brooks, "Limiting efficiency of silicon solar cells," *IEEE Transactions on Electron Devices,* vol. 31, pp. 711-716, 1984.

[122] M. D. Abbott, J. E. Cotter, F. W. Chen, T. Trupke, R. A. Bardos, and K. C. Fisher, "Application of photoluminescence characterization to the development and manufacturing of high-efficiency silicon solar cells," *Journal of Applied Physics,* vol. 100, p. 114514, 2006.

[123] A. Roos, "Use of an integrating sphere in solar energy research," *Solar Energy Materials and Solar Cells,* vol. 30, pp. 77-94, 1993.

[124] J. S. Bhosale, "High signal-to-noise Fourier transform spectroscopy with light emitting diode sources," *The Review of scientific instruments,* vol. 82, pp. 093103-093103, 2011.

[125] D. Berdebes, J. Bhosale, K. H. Montgomery, X. Wang, A. K. Ramdas, J. M. Woodall*, et al.*, "Photoluminescence Excitation Spectroscopy for In-Line Optical Characterization of Crystalline Solar Cells," *IEEE Journal of Photovoltaics,* vol. 3, pp. 1342-1347, 2013.

[126] U. Rau, "Reciprocity relation between photovoltaic quantum efficiency and electroluminescent emission of solar cells," *Phys. Rev. B,* vol. 76, pp. 85303-85303, 2007.

[127] T. Kirchartz, U. Rau, M. Kurth, J. Mattheis, and J. H. Werner, "Comparative study of electroluminescence from Cu(In,Ga)Se2 and Si solar cells," *Thin Solid Films,* vol. 515, pp. 6238-6242, 2007.

[128] C. Donolato, "A reciprocity theorem for charge collection," *Applied Physics Letters,* vol. 46, pp. 270-270, 1985.

[129] Q. Cao, O. Gunawan, M. Copel, K. B. Reuter, S. J. Chey, V. R. Deline*, et al.*, "Defects in Cu(In,Ga)Se2 Chalcopyrite Semiconductors: A Comparative Study of Material Properties, Defect States, and Photovoltaic Performance," *Advanced Energy Materials,* vol. 1, pp. 845-853, 2011.

[130] A. Niemegeers and M. Burgelman, "Effects of the Au/CdTe back contact on IV and CV characteristics of Au/CdTe/CdS/TCO solar cells," *Journal of Applied Physics,* vol. 81, pp. 2881-2881, 1997.

[131] M. Gloeckler, J. R. Sites, and W. K. Metzger, "Grain-boundary recombination in Cu(In,Ga)Se[sub 2] solar cells," *Journal of Applied Physics,* vol. 98, p. 113704, 2005.

[132] P. D. Paulson, R. W. Birkmire, and W. N. Shafarman, "Optical characterization of CuIn[sub 1−x]Ga[sub x]Se[sub 2] alloy thin films by spectroscopic ellipsometry," *Journal of Applied Physics,* vol. 94, p. 879, 2003.

[133] M. Burgelman, F. Engelhardt, J. F. Guillemoles, R. Herberholz, M. Igalson, R. Klenk*, et al.*, "Defects in Cu(In, Ga) Se2 semiconductors and their role in the device performance of thin-film solar cells," *Progress in Photovoltaics: Research and Applications,* vol. 5, pp. 121-130, 1997.

[134] A. Kylner, "Effect of impurities in the CdS buffer layer on the performance of the Cu(In,Ga)Se[sub 2] thin film solar cell," *Journal of Applied Physics,* vol. 85, p. 6858, 1999.

[135] R. K. Ahrenkiel, "Influence of junctions on photoluminescence decay in thin-film devices," *Journal of Applied Physics,* vol. 62, pp. 2937-2937, 1987.

[136] R. K. Ahrenkiel, "Measurement of Minority-Carrier Lifetime by Time-Resolved Photoluminescence," *Solid-State Electronics,* vol. 35, pp. 239-250, Mar 1992.

[137] D. K. Schroder, *Semiconductor Material and Device Characterization*, 3 ed.: Wiley, 2006.

[138] W. K. Metzger, D. Albin, D. Levi, P. Sheldon, X. Li, B. M. Keyes*, et al.*, "Time-resolved photoluminescence studies of CdTe solar cells," *Journal of Applied Physics,* vol. 94, p. 3549, 2003.

[139] W. K. Metzger, R. K. Ahrenkiel, and P. Dippo, "Time-resolved photoluminescence and photovoltaics," *Department of Energy Solar Energy Technologies Program Review Meeting,* vol. 1, pp. 1-2, 2004.

[140] T. Trupke, B. Mitchell, J. W. Weber, W. McMillan, R. A. Bardos, and R. Kroeze, "Photoluminescence Imaging for Photovoltaic Applications," *Energy Procedia,* vol. 15, pp. 135-146, 2012.

[141] T. Trupke and R. A. Bardos, "Photoluminescence: A surprisingly sensitive lifetime technique," *Conference Record of the Thirty-First IEEE Photovoltaic Specialists Conference - 2005,* pp. 903-906, 2005.

[142] A. Kanevce, D. H. Levi, and D. Kuciauskas, "The role of drift, diffusion, and recombination in time-resolved photoluminescence of CdTe solar cells determined through numerical simulation," *Progress in Photovoltaics: Research and Applications,* 2013.

[143] D. N. Hebert, J. A. N. T. Soares, and A. a. Rockett, "Photoluminescence and Photoluminescence Excitation Spectroscopy of Cu(In,Ga)Se2 Thin Films," *MRS Proceedings,* vol. 1165, pp. 1165-M03-05, 2011.

[144] S. Sandhu, Z. Yu, and S. Fan, "Detailed balance analysis and enhancement of open-circuit voltage in single-nanowire solar cells," *Nano Lett,* vol. 14, pp. 1011-5, Feb 12 2014.

[145] D. Kuciauskas, A. Kanevce, J. N. Duenow, P. Dippo, M. Young, J. V. Li*, et al.*, "Spectrally and time resolved photoluminescence analysis of the CdS/CdTe interface in thin-film photovoltaic solar cells," *Applied Physics Letters,* vol. 102, p. 173902, 2013.

[146] D. Shvydka, V. G. Karpov, and A. D. Compaan, "Bias-dependent photoluminescence in CdTe photovoltaics," *Applied Physics Letters,* vol. 80, p. 3114, 2002.

[147] H. W. Hillhouse and M. C. Beard, "Solar cells from colloidal nanocrystals: Fundamentals, materials, devices, and economics," *Current Opinion in Colloid & Interface Science,* vol. 14, pp. 245-259, 2009.

[148] A. P. Kirk, M. J. DiNezza, S. Liu, X.-H. Zhao, and Y.-H. Zhang, "CdTe vs. GaAs solar cells: A modeling case study with preliminary experimental results," in *IEEE Photovoltaic Specialists Conference*, Tempa, FL, 2013, pp. 2515-2517.

[149] D. A. R. Barkhouse, O. Gunawan, T. Gokmen, T. K. Todorov, and D. B. Mitzi, "Device characteristics of a 10.1% hydrazine-processed Cu2ZnSn(Se,S)4 solar cell," *Progress in Photovoltaics: Research and Applications,* vol. 20, pp. 6-11, 2012.

[150] A. Kanevce, D. Kuciauskas, T. A. Gessert, D. H. Levi, and D. S. Albin, "Impact of interface recombination on time resolved photoluminescence (TRPL) decays in CdTe solar cells," in *IEEE Photovoltaic Specialists Conference*, 2011, pp. 000848-000853.

[151] D. Kuciauskas, A. Kanevce, J. M. Burst, J. N. Duenow, R. Dhere, D. S. Albin, *et al.*, "Minority Carrier Lifetime Analysis in the Bulk of Thin-Film Absorbers Using Subbandgap (Two-Photon) Excitation," *IEEE Journal of Photovoltaics,* vol. 3, pp. 1319-1324, 2013.

[152] L. A. Eldada, V. Buschmann, S. Fore, F. Koberling, A. Knigge, P. Kapusta, *et al.*, "Characterization and quality control of semiconductor wafers using time-correlated single photon counting," *Proc. of SPIE,* vol. 8470, p. 84700F, 2012.

[153] R. Kapadia, Z. Yu, H.-H. H. Wang, M. Zheng, C. Battaglia, M. Hettick, *et al.*, "A direct thin-film path towards low-cost large-area III-V photovoltaics," *Scientific reports,* vol. 3, pp. 2275-2275, 2013.

[154] V. Liu and S. Fan, "S4 : A free electromagnetic solver for layered periodic structures," *Computer Physics Communications,* vol. 183, pp. 2233-2244, 2012.

VITA

VITA

Xufeng Wang received his BSc. and MSc. in Electrical Engineering from Purdue University, West Lafayette, IN, in 2008 and 2010 respectively. From 2010-2014 he has been pursuing his Ph.D. degree at Purdue University in the area of Microelectronics and Nanotechnology. He is a member of the Network for Photovoltaic Technology (NPT) group at Purdue. His research interests include the theory, modeling and simulation of photovoltaic devices.